TR 3906-S

Stellingen

Behorend bij het proefschrift

Electromagnetic Interaction Modeling on Radio Proximity Fuzes for Incoming Targets

door Erdal Korkmaz

- Voor een eenduidige oplossing van de verstrooiing door een ondoordringbaar object met behulp van integraalvergelijkingen over de rand van het object zijn consistentie-eisen in het inwendige ervan essentieel.
- Voor een voldoende foutcriterium kunnen nietnoodzakelijke eisen in de formulering van een verstrooiingsprobleem met voordeel in rekening worden gebracht.
- Het verdient aanbeveling om de zwakke vorm van de Greense functie te verkrijgen door middel van een bolgemiddelde over de inverse van de afstand.

Dit proefschrift, Hoofdstuk 4.

- 4. Bij het gebruik van een nabijheidsbuis is kennis over de verstrooiingseigenschappen van een vijandelijk doel noodzakelijk voor het onderkennen van de geometrie van het doel en het punt van interceptie.
- 5. Een dun SiC laagje met lage mechanische spanning gedeponeerd met een techniek van de "Plasma Enhanced Chemical Vapor Deposition" is gunstig voor "IC-compatible" micro-sensoren.

E. Korkmaz, 'Low-stress PECVD SiC thin films for IC-compatible microstructures', MSc thesis, Delft University of Technology, The Netherlands, November 1997.

- 6. Een onderzoek dat uitsluitend resultaatgericht is, beperkt de persoonlijke ontplooiing.
- 7. Tolerantie en dialoog zijn de pijlers van een multiculturele samenleving.
- 8. Het woord 'geloven' wordt meestal verkeerd opgevat en veelal gebruikt wanneer er concrete bewijzen zijn over hetgeen waarin men gelooft.
- 9. Het oude gezegde "Wie de jeugd heeft, heeft de toekomst" verdient nieuwe aandacht.
- 10. Een goede spits in een voetbalteam onderscheidt zich door de keuze van de positie waar hij zich aanbiedt.



390. 730229

Electromagnetic Interaction Modeling on Radio Proximity Fuzes for Incoming Targets

TR 3906



Electromagnetic Interaction Modeling on Radio Proximity Fuzes for Incoming Targets

Proefschrift



ter verkrijging van de graad van doctor
aan de Technische Universiteit Delft,
op gezag van de Rector Magnificus prof. dr. ir. J.T. Fokkema,
voorzitter van het College voor Promoties,
in het openbaar te verdedigen op donderdag 19 september 2002 om 13:30 uur
door

Erdal Korkmaz

elektrotechnisch ingenieur geboren te Göle, Turkije. Dit proefschrift is goedgekeurd door de promotor:

Prof. dr. ir. P.M. van den Berg

Samenstelling promotiecommissie:

Rector Magnificus,

Prof. dr. ir. P.M. van den Berg, Prof. dr. ir. J.T. Fokkema,

Prof. dr. ir. A. Gisolf,

Prof. ir. P. Hoogeboom,

Prof. dr. ir. A.P.M. Zwamborn, Dr. A.J. Schoolderman,

Dr. ir. A. Abubakar,

voorzitter

Technische Universiteit Delft, promotor

Technische Universiteit Delft

Technische Universiteit Delft

Technische Universiteit Delft

Technische Universiteit Eindhoven

TNO-FEL

Technische Universiteit Delft

$Published\ and\ distributed\ by:$

Drukkerij Deniz

Brielselaan 135

3081 AB Rotterdam The Netherlands

Telephone:

+31 10 4858488

fax:

 $+31\ 10\ 2152803$

E-mail: info@drukkerijdeniz.nl

ISBN 90-9016148-1

Keywords: scattering, integral equations, moving targets

Copyright © 2002 by E. Korkmaz

All rights reserved. No part of the material protected by this copyright notice may be reproduced or utilized in any form or by any means, electronic or mechanical, including photocopying, recording or by any information storage and retrieval system, without permission from the publisher: Delft University Press.

Printed in The Netherlands

Contents

1				
2				
	2.1. Description of experimental setup		7	
	2.2. Electromagnetic field from a dipole antenna		9	
	2.3. Calibration		11	
3	Formulation of the Scattering Problem			
	3.1. The scattering configuration		19	
	3.2. Lorentz's reciprocity theorem		20	
	3.3. Electromagnetic Green's states		21	
	3.4. General integral representations		23	
	3.5. Integral representations for scattered field		26	
	3.5.1. Integral representations		28	
	3.5.2. Integral equations		29	
	3.5.3. Interior representations		30	
4	Numerical Approach		31	
	4.1. Discretization of the geometry		31	
	4.2. Discretization of integral representations		33	

viii CONTENTS

	4.3.	tization of integral equations	34			
	4.4.	Conjug	gate gradient method	36		
		4.4.1.	An additional error criterion	39		
		4.4.2.	Numerical example of a sphere	40		
	4.5.	Constr	cained conjugate gradient method	44		
		4.5.1.	Numerical example of a sphere	47		
		4.5.2.	Numerical results of a finite cylinder	55		
		4.5.3.	Numerical results of a plate	56		
		4.5.4.	Numerical results of a capped box	59		
5	Comparison of Experimental and Numerical Results					
	5.1.	Exper	iments with a sphere	63		
	5.2.	. Experiments with a finite cylinder				
	5.3.	Experiments with a finite flat plate				
	5.4.	Exper	iments with a capped box	84		
6	Con	ns	97			
\mathbf{A}	ppen	dix		101		
	A.	Discr	etization of the geometry	101		
	В.	Weak	form of Green's function	104		
Samenvatting						
About the author						

Chapter 1

Introduction

Since World War II proximity fuzes are used against aerial targets. The principle of these fuzes is based on the observation of moving aerial targets in the near field of the antenna present in a proximity fuze. It radiates a continuous RF signal. When the target passes the proximity fuze, part of the signal is received back due to the reflection. The received signal has a small difference in frequency when the target is moving. This small difference frequency (the so-called LF Doppler signal) is proportional with the relative velocity between the proximity fuze and the moving target. The LF Doppler signal forms the input of a piece of electronic signal processing equipment and an algorithm that has to decide whether or not, and at which moment, an explosion has to take place so that the target is destroyed.

The knowledge about the scattering properties of targets is not only useful for the evaluation of the performance of proximity fuzes, it can also be used to design proximity fuzes that recognize their target and the geometry of interception. This would lead to an optimization of the burst point, and an increase of the effectivity of the fuze.

In order to develop new types of proximity fuze a trajectory simulator and scaled models are used at TNO-FEL. However, this simulator has some restrictions and therefore a software simulator is required. Our aim is to develop a method of calculating the electromagnetic interaction between the fuze and the target when the passing-by distance between the target and the fuze is less than or equal to the size of the target. The method can then be used as a basic tool in a computer model that generates the target signals.

Our present research objective is to develop a method to calculate the scattered electromagnetic fields by a moving object. In 1991 Vogel [1] calculated the near-by reflection of aerial targets in the radar frequency (cm-waves). In his calculations the moving object is large with respect to the wavelength. For this reason he has used the 'Physical-Optics' approximations to compute the surface field at the target. Furthermore, his experiments were restricted to rotationally symmetrical scatterers. In the present study we aim to compute the surface field on an object of general shape, by solving an integral equation over the surface of the target.

In Chapter 2, we describe the experimental setup where we have performed measurements in order to compare the accuracy of numerically computed results. In the experimental setup, the received signals are processed by a microwave mixer, such that the output voltage is proportional to the real part of the complex value of the measured electric field component [1]. To facilitate a comparison between modeled and experimental results, we replace the actual transmitter/receiver antenna by an effective dipole. Subsequently we determine the actual magnitude of the dipole moment of our effective dipole antenna by means of determining a multiplicative constant between the measured signal and the simulated field responses. For this calibration we take a very large plate as a scatterer so that the reflected fields are known analytically and can be computed directly. After presenting the measured and calibrated computed results we observe a phase shift between the two results. This may be due to the actual positioning of the scatterer, where a small location error is made. Hence we further develop a calibration procedure to find an improved estimate for the location of the origin of the effective dipole.

In Chapter 3, we formulate the stationary scattering problem as a problem of scattering an electromagnetic wave field by an electrically perfectly conducting object. In view of our application we aim to solve this scattering problem for objects having dimensions in the order of a wavelength. This means that the physical-optics approximation is not valid and we have to develop a rigorous computational method. From Lorentz' reciprocity theorem [2], we briefly discuss the derivation of the integral representations for the scattered fields in terms of the tangential component of the total magnetic field on the boundary surface of the scattering object. This unknown surface field follows from a solution of an integral equation over the boundary of the object. There are two types of integral equations, one of the electric type and one of the magnetic type, see e.g. [3, 4]. Since the magnetic-field

equation is an integral equation of the second kind and easy to discretize we take this boundary integral equation as point of departure.

A disadvantage of the use of boundary type integral equations is related to the non-uniqueness of their solution. In absence of an exciting field, the boundary integral equations can also represent the electromagnetic field solution of a cavity enclosed by the boundary of the object. Thus, at certain eigenfrequencies associated with the cavity problem, the homogeneous type of integral equation yields source-free solutions. Hence, the solution of the integral equation for the exterior problem will not be unique when a nontrivial solution exists to the interior problem. Although the theoretical problem of the non-uniqueness has been well understood [5, 6], the problem is often not anticipated in advance. Development involving the numerical solution of integral equations typically concentrates on the treatment of electrically small or moderately-sized scatterers, at least for the initial testing and validation of the formulations. Then, the solution is obtained by a direct matrix inversion of the discretized equations and the electric-field and magnetic-field integral equations produce perfect solutions as long as the frequency of operation does not coincide with an eigenfrequency of an interior resonance [7]. For electrically large objects, the number of unknowns becomes so large that direct matrix inversion is not feasible, and we adopt the conjugate gradient method [8, 9] as an iterative solver of the discretized integral equation. But, within some frequency band around the eigenfrequency of an internal resonance, the convergence rate of this iterative scheme decreases dramatically and the numerical results are not reliable.

Mitzner [10] recommended the use of a linear combination of the electric-field integral equation and the magnetic-field integral equation as a remedy to overcome non-uniqueness problems at eigenfrequencies of interior resonances. The resulting formulation is known as the combined-field integral equation [11, 12]. But the drawback is the increase of computation time for the calculation of the matrix elements of the two sets of discretized equations. Yaghjian [13] augmented the magnetic-field integral equation with the normal projection of the integral equation, while recently an iterative solution of this augmented system is discussed by Makarov and Vedantham [15]; the latter authors remark that their approach is not expected to completely eliminate the numerical problems due to the spurious resonances. Another approach is the use of dual surfaces [16, 17] to create a well-conditioned problem. The dual surface is located at approximately one quarter wavelength inside the actual scatterer surface. The disadvantage is the extra computa-

tion of the matrix elements with respect to this interior dual surface. Our present objective is to minimize these extra computations by taking a smaller interior surface, without losing uniqueness. This is achieved by using the integral equations in combination with interior integral representations (often called null-field equations) obtained by applying Oseen's extinction theorem [18]. In contrast to the dual surface equation used in [16] and [17], where the tangential components of the electric-field integral equations are used, we propose to include the null-field equations for the three components of the magnetic field. This guarantees uniqueness, irrespectively of the choice of the closed interior surface. This idea is inspired by the work of Schenck [19] in acoustics, and the work of Mittra and Klein [20] in electromagnetics, using an over-specification with these null-field equations throughout the interior region. Although we are dealing with a unique solution when all interior points are taken into account, for computational reasons the number of interior points (and hence extra equations) should be limited. The pre-selection of the interior points must then be based on some a priori information about the occurrence and nature of the interior resonances. In this thesis, this problem is avoided by assuming that these interior points span a surface that encloses a non-vanishing subdomain. Observing that on this closed interior surface convergent expansions of the incident field and the Green function in spherical regular vector eigenfunctions [21] exist, we may conclude that the interior field representations hold everywhere in the interior of the object and hence uniqueness is guaranteed. We therefore replace the pre-selection of interior points by a null-field integral equation over a closed interior surface. We first use the null-field integral equation, to be imposed on a closed interior surface, as a criterion to monitor the error in the solution. Subsequently we use it as a sufficient constraint to the boundary integral equation to guarantee a unique solution. Combining this first kind null-field integral equation together with the second kind boundary equation of the magnetic type and normalizing both equations properly [14], the illposedness of the first kind integral equation over the interior surface is not important and we may choose the interior surface as small as possible, as long as the field variation over this surface remains computable within the degree of accuracy.

In Chapter 4, we discuss the discretization of the boundary of the scattering object in a number of planar triangles. We further discuss a weak form of the Green function, that is finite and defined everywhere, and that replaces the exact one. Then in the integration over a patch, it is allowed

to interpolate the integrands linearly in terms of their values at the vertices. We formulate a conjugate gradient iterative scheme [22] that minimizes an integrated squared error over the boundary surface of the object and uses the integrated squared error norm over an internal surface as an additional check for the numerical results. For a sphere we compare the results with the analytical solution in terms of the Mie series [23]. We observe that the additional error criterion is also a computational error criterion to quantify the error made in the discretization of the boundary integral equation. This inspires us to use this error norm as a constraint for the conjugate gradient scheme. Then a modified conjugate gradient scheme (based on the principles developed in [24]) is presented, such that both the normalized error norm in the satisfaction of the boundary integral equation and the normalized error norm in the satisfaction of the integral equation over the interior surface are minimized simultaneously. Some numerical tests are performed and with some very small additional computer time (less than 3%) we observe that the combined error criterion indeed reflects the actual discretization error of the problem at hand, and in addition it overcomes the problem of non-uniqueness due to interior resonances.

In Chapter 5, we compare our numerically computed results and the measured results for various perfectly conducting objects. We use a measurement setup in an anechoic chamber, where the antenna is moved to the object under consideration. In our computations we assume that the speed of movement is much smaller than the wave speed in vacuum, so that no relativistic corrections are needed. This means that for each location of the transmitter/receiver antenna the scattering problem can be handled as a stationary one. In other words, we are dealing with a monostatic scattering problem. In the experimental setup, the received signals are processed by a microwave mixer, such that the output voltage is proportional to the real part of the complex value of the measured electric field component [1]. Therefore we have multiplied our computed results with the calibration constant calculated as described in Chapter 2. In addition, we use the correction of the positioning of the antenna configuration determined in Chapter 2.

In our simulations, we first compute the surface field with the constrained conjugate gradient method as developed in Chapter 4. Since we compute the scattered fields at certain discrete points along the measurement range we determined a factor which is roughly proportional with the field change along the movement. We use this factor to improve the initial estimate when we change the antenna position. After computation of the surface field we

compute the scattered field. We also compare the measured results with simulated results when we take the physical-optics approximation for the surface field. After the comparisons of the measured results and simulated results for some simple canonical objects (sphere, cylinder and plate), we also made some numerical simulations with the physical-optics approximation and constrained conjugate gradient method for a capped box, in order to study the accuracy of physical optics approximation for a more complicated scatterer. We compare the results for three different orientations of the capped box.

Chapter 2

Experimental Setup

In order to compare the accuracy of numerical results for various objects we have performed some measurements. Since we model the antenna as an electric dipole source, we want to determine the effective dipole moment. The first thing is to calibrate the modeled field from this dipole source; in fact we want to determine the amplitude of the dipole moment and the origin (phase center) of the dipole source. We therefore discuss a measurement setup and calibration scheme, where the antenna is moved to a very large flat plate, so that the measured reflected field can be considered as generated by a mirrored antenna.

2.1. Description of experimental setup

The measurements are performed in an anechoic chamber to avoid unwanted reflections caused by other objects present (e.g. the walls, floor, ceiling). The measurement setup consists of two perpendicularly standing rails, one lower rail and one upper rail (see Fig. 2.1). The upper rail is fixed and has a sledge to move horizontally the suspending object. The scattering object is suspended from the sledge of the upper rail and fixed with cores on three points. The lower rail has also a sledge on which the antenna is located and this sledge can move horizontally, while the lower rail can move entirely vertically with the help of linear induction motors. The antenna has a function of transmitting electromagnetic field and receiving reflected fields by the object present. The rails are covered by a foam that absorbs electromagnetic

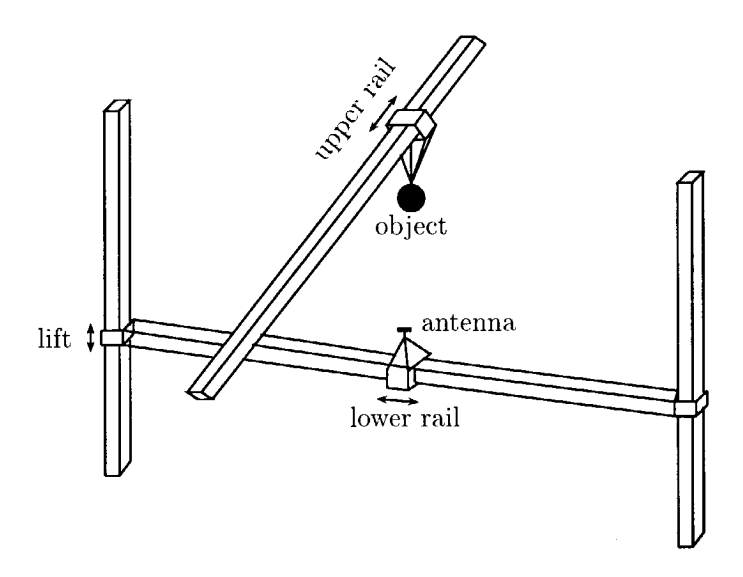


Figure 2.1: The experimental setup

energy and exhibits very low reflection. Its relative permittivity is typically 1.04.

The experiments are performed at 35.06 GHz. The various scattering objects chosen for the experiments are made of conducting materials like aluminum and copper. We assume that we are dealing with perfectly conducting objects.

The antenna (see Fig. 2.2), that transmits and receives the electromagnetic signals, has approximately a half-wave dipole radiation pattern. The pedestal for the antenna is also made of polystyrene foam. Since we model the antenna as an electric dipole source, we want to determine the effective dipole moment; this is achieved by matching the modeled incident field from this dipole source to the field from the actual antenna. In fact we want to determine the amplitude of the dipole moment and the origin (phase center) of the dipole source. Therefore, we first describe the modeled electromagnetic field from a dipole source.

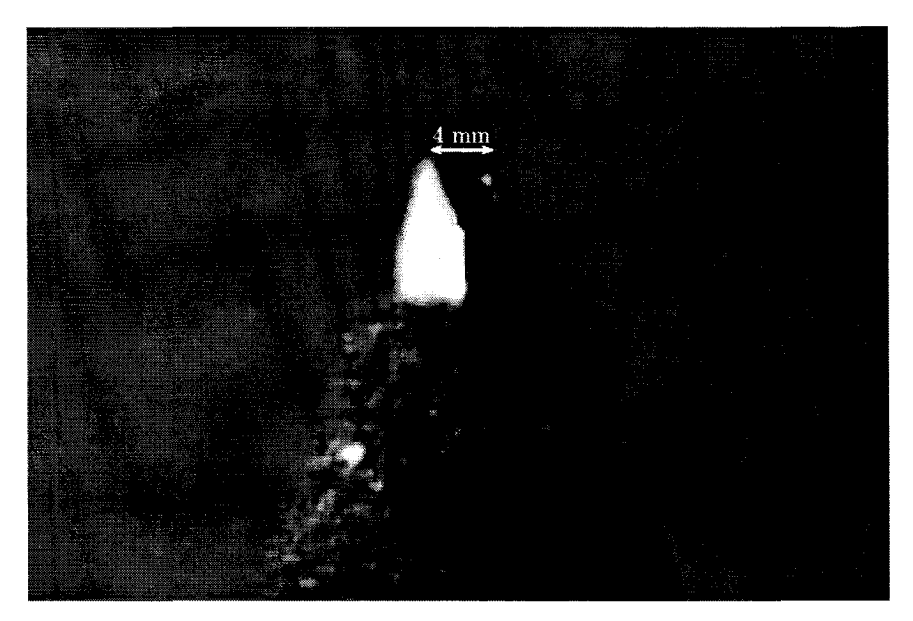


Figure 2.2: The transmitting and receiving antenna.

2.2. Electromagnetic field from a dipole antenna

In this section we compute the field strengths of the electromagnetic field emitted by a dipole antenna. We consider the dipole antenna as a short, straight segment of a thin, conducting, current-carrying wire. In the thin-wire approximation, we replace the actual volume distribution of electric current by a line current concentrated at the center line of the conductor, the line current having the direction of the local tangent to the line segment. We use the complex representation of field quantities with complex time factor $\exp(-i\omega t)$, where i is the imaginary unit and $\omega=2\pi f$ is the angular frequency and f is the frequency of operation in Hz. To locate a point in space we use a Cartesian coordinate system with position vector $\boldsymbol{x} = \{x,y,z\}$.

We now consider the electromagnetic field at a point x generated by a dipole antenna with center at x^T (see Fig. 2.3). For an arbitrary dipole source distribution, the expressions for the electromagnetic field quantities E and H in an unbounded, homogeneous domain \mathbb{R}^3 are [2]

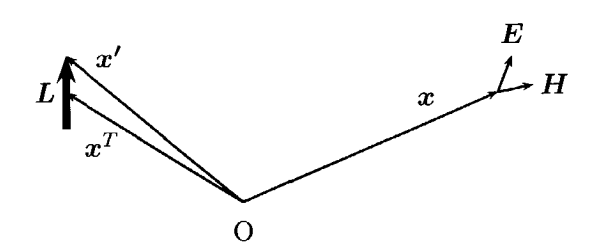


Figure 2.3: Configuration for a dipole antenna.

$$E(\boldsymbol{x}) = \frac{-1}{\mathrm{i}\omega\varepsilon_0} [k_0^2 + \boldsymbol{\nabla}\boldsymbol{\nabla}\cdot] \int_{\boldsymbol{x}'\in\mathbf{R}^3} G(\boldsymbol{x}-\boldsymbol{x}') \boldsymbol{J}(\boldsymbol{x}') \,\mathrm{d}V, \qquad (2.1)$$

$$H(x) = \nabla \times \int_{x' \in \mathbb{R}^3} G(x - x') J(x') dV,$$
 (2.2)

where $k_0 = \omega(\varepsilon_0 \mu_0)^{\frac{1}{2}}$ is the wave number, ε_0 is the free-space permittivity and μ_0 is the free-space permeability. Further, G is the free-space Green function given by

$$G(\boldsymbol{x} - \boldsymbol{x}') = \frac{\exp(ik_0|\boldsymbol{x} - \boldsymbol{x}'|)}{4\pi|\boldsymbol{x} - \boldsymbol{x}'|}$$
(2.3)

and J is the volume density of electric current. Assuming that the dipole antenna is located at $x' = x^T$ and that it can be approximated as a short, straight and thin wire, we then approximate the integral at the right-hand sides of Eqs. (2.1) and (2.2) as

$$\mathbf{A} = \int_{x' \in \mathbb{R}^3} G(\mathbf{x} - \mathbf{x}') \mathbf{J}(\mathbf{x}') \, dV,$$

$$\approx G(\mathbf{x} - \mathbf{x}^T) \int_{x' \in \text{antenna}} \mathbf{J}(\mathbf{x}') \, dV,$$

$$\approx G(\mathbf{x} - \mathbf{x}^T) I_{ant} \mathbf{L}, \qquad (2.4)$$

where I_{ant} denotes the electric current through the dipole antenna and L denotes the oriented length of the dipole.

Using the approximation of Eq. (2.4) in Eqs. (2.1) and (2.2) and after computing the spatial derivatives of $\nabla = \{\partial_x, \partial_y, \partial_z\}$, we note that the fields may be written as $E(x) = E(x - x^T)$ and $H(x) = H(x - x^T)$, where the

CALIBRATION 11

fields $\boldsymbol{E}(\boldsymbol{x}) = \boldsymbol{E}(\boldsymbol{x} - \boldsymbol{x}^T)$ and $\boldsymbol{H}(\boldsymbol{x}) = \boldsymbol{H}(\boldsymbol{x} - \boldsymbol{x}^T)$ are obtained as

$$E(x - x^{T}) = I_{ant} \left\{ \frac{1}{i\omega\varepsilon_{0}} \frac{(L - 3\Theta\Theta \cdot L)}{|x - x^{T}|^{2}} - \frac{k_{0}}{\omega\varepsilon_{0}} \frac{(L - 3\Theta\Theta \cdot L)}{|x - x^{T}|} + i\omega\mu_{0}(L - \Theta\Theta \cdot L) \right\} G(x - x^{T}),$$
(2.5)

$$H(x - x^T) = I_{ant} \left[ik_0 - \frac{1}{|x - x^T|} \right] \Theta \times LG(x - x^T),$$
 (2.6)

with unit vector

$$\Theta = \frac{\boldsymbol{x} - \boldsymbol{x}^T}{|\boldsymbol{x} - \boldsymbol{x}^T|}.$$
 (2.7)

This electromagnetic field is taken as the field that is generated by the antenna and it is considered as the field that incidents on the object under investigation. Therefore this field is denoted as $\{E^i, H^i\}$. It is linearly related to the magnitude of the dipole moment $I_{ant}L$. To determine this magnitude we carry out a particular calibration experiment.

2.3. Calibration

In the experimental setup, the received signals are processed by a microwave mixer, such that the output voltage is proportional to the real part of the complex value of the measured electric field component [1]. In order to be able to compare the experimental with the measured results we have to perform some calibration to determine the multiplicative constant between the measured signal and the simulated field responses. In view of the linearity of the problem at hand, it means that we want to determine the actual magnitude of the dipole moment of our effective dipole antenna, say

$$C = |I_{ant} \mathbf{L}|, \qquad (2.8)$$

such that the responses of the measured output and the simulated received field values coincide as well as possible. The phase is calibrated in a subsequent step.

The calibration is carried out with a scattering experiment, where the reflected field from the scattering object is known. As scattering object we

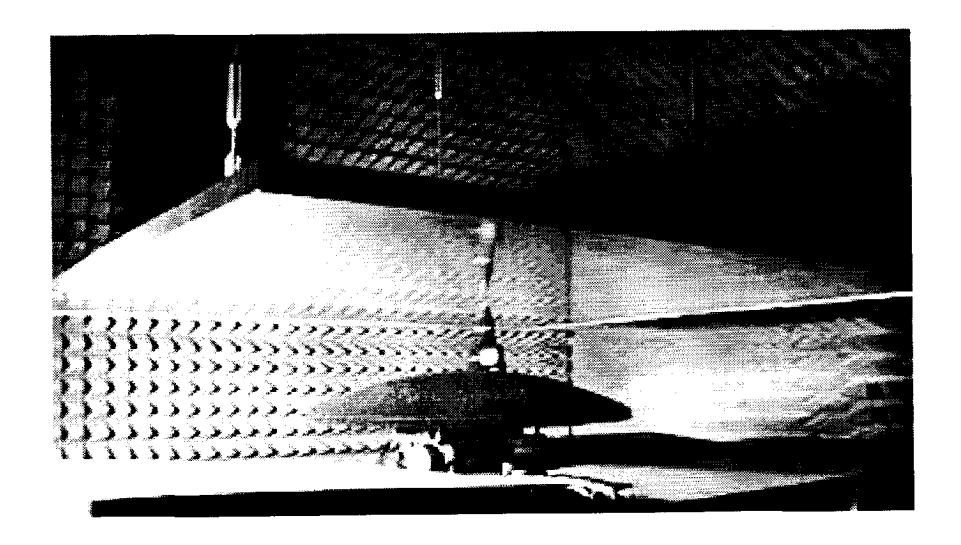


Figure 2.4: Antenna moving to a large plate.

simply have chosen a large aluminum square flat plate with side lengths of 1.20 m and moved the antenna towards the plate (Fig. 2.4). The idea is based on the fact that the size of the plate is much larger than the wavelength (0.856 cm) of the electromagnetic wave field. Hence, it can be considered as an infinitely large plate and therefore a total reflection will be obtained. The scattering pattern of that experiment can be mathematically modeled as a mirrored dipole source moving towards the plate (Fig. 2.5).

We consider a coordinate system such that the metal plate coincides with z=0. The dipole is moved along the z-axis. Let us denote the spatial position of the effective dipole source by $\mathbf{x}^T = \{0,0,d\}$ and let us assume that the dipole is oriented in the y-direction (see Fig. 2.5). Then, the measured reflected field at \mathbf{x}^T can be considered as the field from a dipole source located at its image point $\mathbf{x}^{T,image}$ with a negative current $-I_{ant}$. For this reason, in our model computations we simply take the dipole moment as $I_{ant}\mathbf{L} = \{0, -1, 0\}$ and the source point as $\mathbf{x}^T = \{0, 0, -d\}$, and compute the y-component of the field at $\mathbf{x} = \{0, 0, d\}$. The real part of this field component represents the reflected field received in the antenna and is denoted as E^T . This experiment is carried out for a moving antenna along

CALIBRATION 13

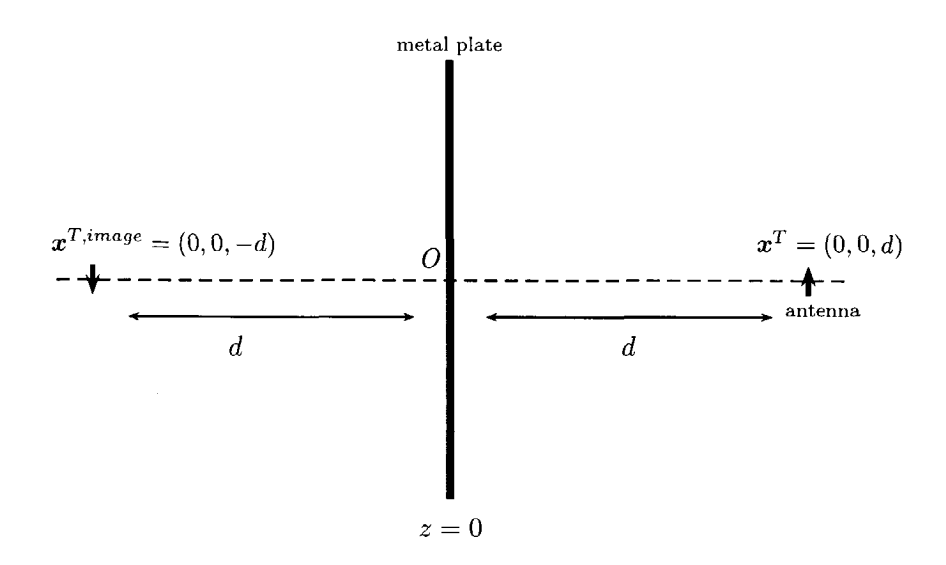


Figure 2.5: Configuration for the calibration: A dipole antenna is moving towards the infinite metal plate.

the z-direction. Since the speed of movement is very low, it means that the measurements of the field are carried out for some discrete values of d, viz.,

$$d_k = k\Delta z, \quad k = k_{start}, \cdots, k_{end}, \qquad (2.9)$$

in which Δz is the sampling interval in the z-direction. The measured field values are denoted as $e(d_k)$. The real part of the simulated field values are denoted as $E^r(d_k)$. For an observation range of 30 mm $< d_k <$ 260 mm, the results of the measurement and the computed model are depicted in Figs. (2.6) and (2.7). In the measurement results we observed roughly 0.24 V DC value of the measurement setup and we have subtracted it from all measurement results. In view of the different amplitudes, we determine a calibration constant C, see Eq. (2.8), from

$$C = \left(\frac{\sum_{k=k_{start}}^{k_{end}} |e(d_k)|^2}{\sum_{k=k_{start}}^{k_{end}} |E^r(d_k)|^2}\right)^{1/2}.$$
 (2.10)

After taking $|I_{ant}L| = C$ in our simulations we present the measured and calibrated computed results in Fig. 2.8. From this figure we observe that

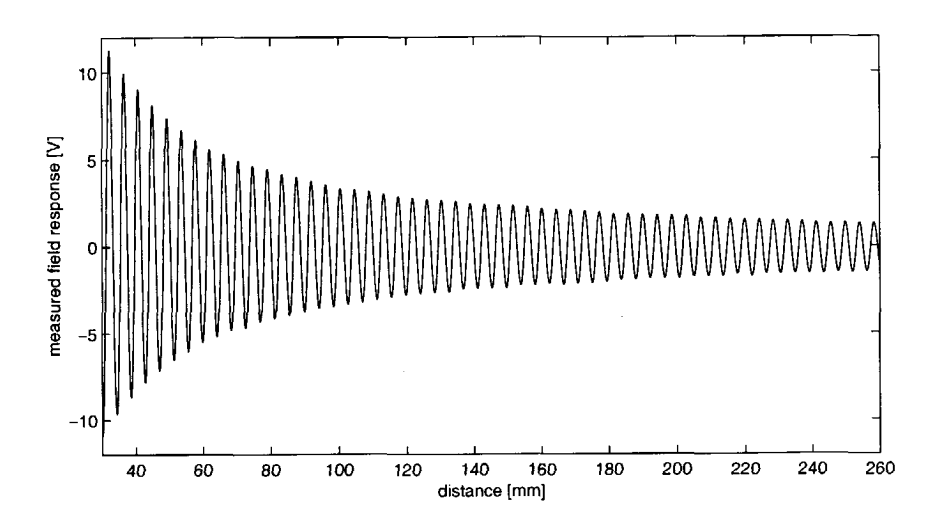


Figure 2.6: Measurement signal, $e(d_k)$, as a function of distance d_k .

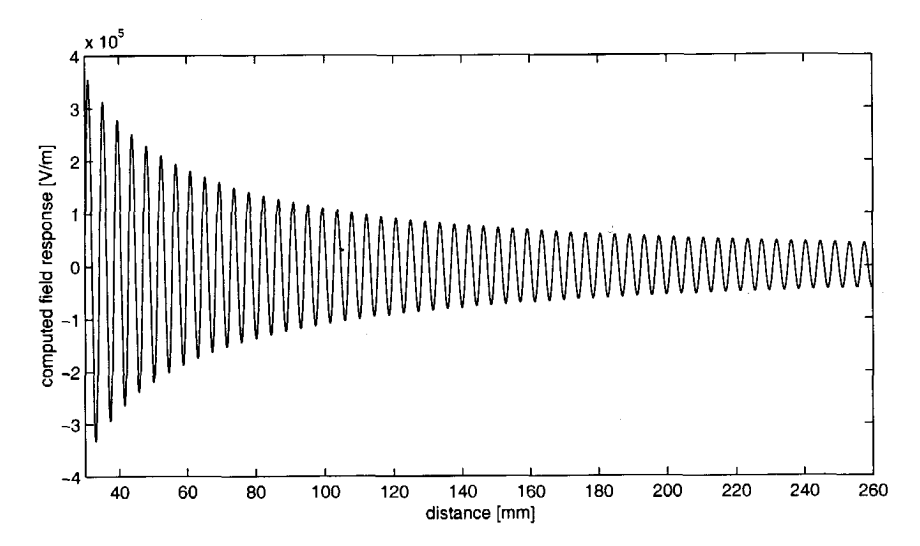


Figure 2.7: Computed field response, $E^r(d_k)$, as a function of distance d_k .

there is some shift between the two results in the z-direction. This may be due to the uncertainty in the determination of the phase center of the actual antenna. Therefore we carry out a second calibration to find an improved estimate for the location of the origin of the effective dipole. We now assume

CALIBRATION 15

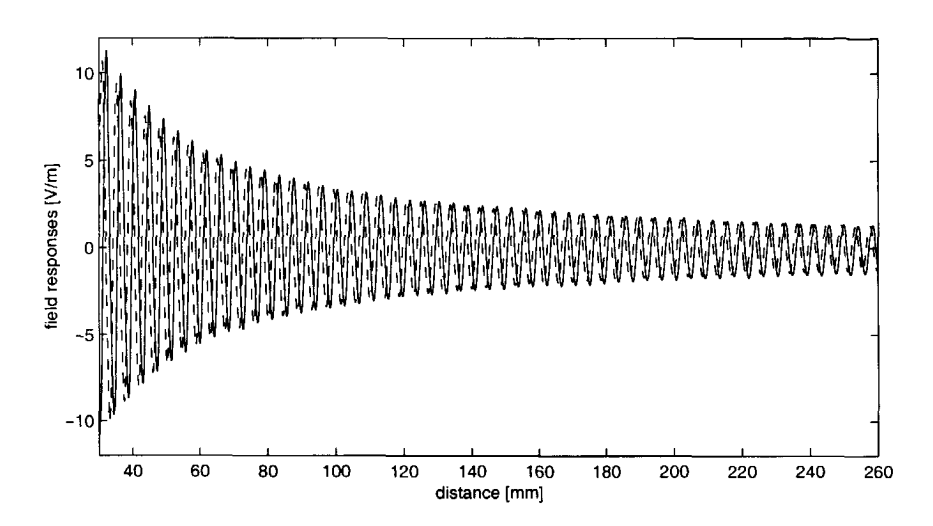


Figure 2.8: The measurement (solid line) and simulated (dashed line) responses after calibration as a function of distance d_k .

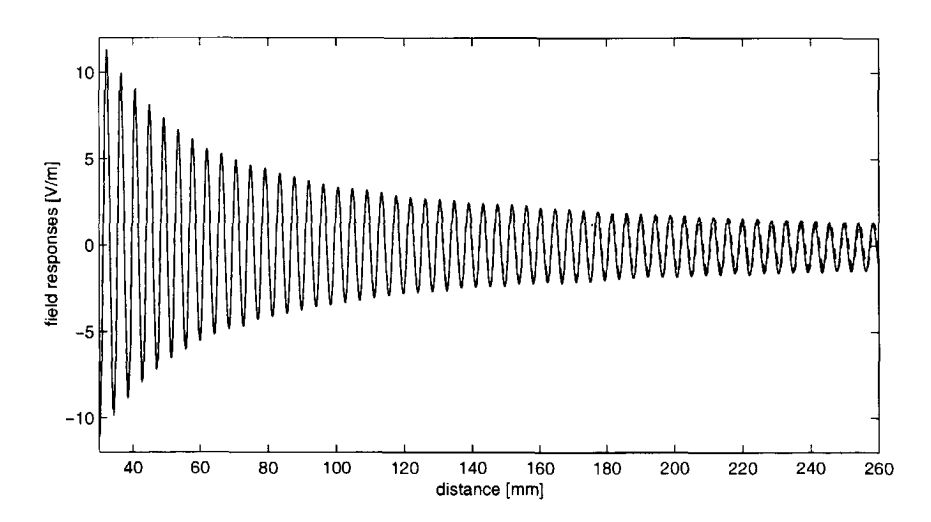


Figure 2.9: Same as Fig. 2.8, but now after phase center correction.

the dipole located to be at $\mathbf{x}^T = \{0, 0, d + \Delta d\}$. To find the shift Δd we consider the correlation, $P(\Delta d)$, involving the sequences $E^r(d_k + \Delta d)$ and $e(d_k)$. We consider this correlation as function of Δd , where we express Δd

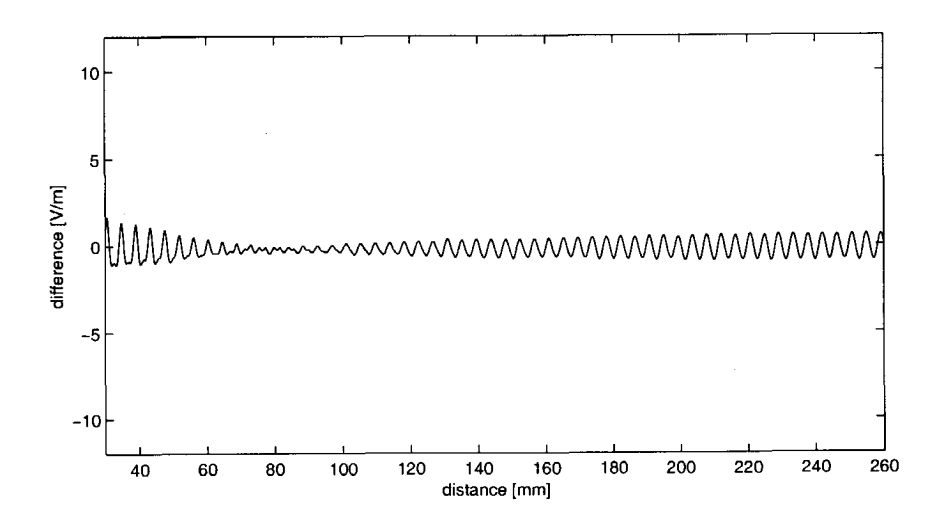


Figure 2.10: The differences between the measurement signal and computed signals, after the two calibration steps.

in terms of the discrete variable l as

$$\Delta d = l\Delta z$$
, $l = -\frac{1}{2}L, \cdots, \frac{1}{2}L$, (2.11)

where the interval $[-\frac{1}{2}L,\frac{1}{2}L]$ is chosen such that the oscillating curve of the simulated field response shifts at most one period. Hence, $L=\lambda$, where λ is the free-space wavelength of the electromagnetic wave field. Then our correlation function is defined as

$$P = \sum_{k=k_{start} + \frac{1}{2}L}^{k=k_{end} - \frac{1}{2}L} e(d_k) E^r(d_k + l\Delta z).$$
 (2.12)

We search for its maximum by varying l and determine the proper calibration value of l as the one where the correlation P has a maximum. From Eq. (2.11) the value of Δd , is obtained as $\Delta d = 0.58$ mm in this way, we have found the actual source point of our dipole model. After applying this phase center correction, the simulated results and the measured ones are depicted in Fig. 2.9. The differences between these two results are depicted in Fig. 2.10.

Finally we have to mention that unfortunately, even the most carefully designed anechoic chamber will produce some residual reflections. To have

CALIBRATION 17

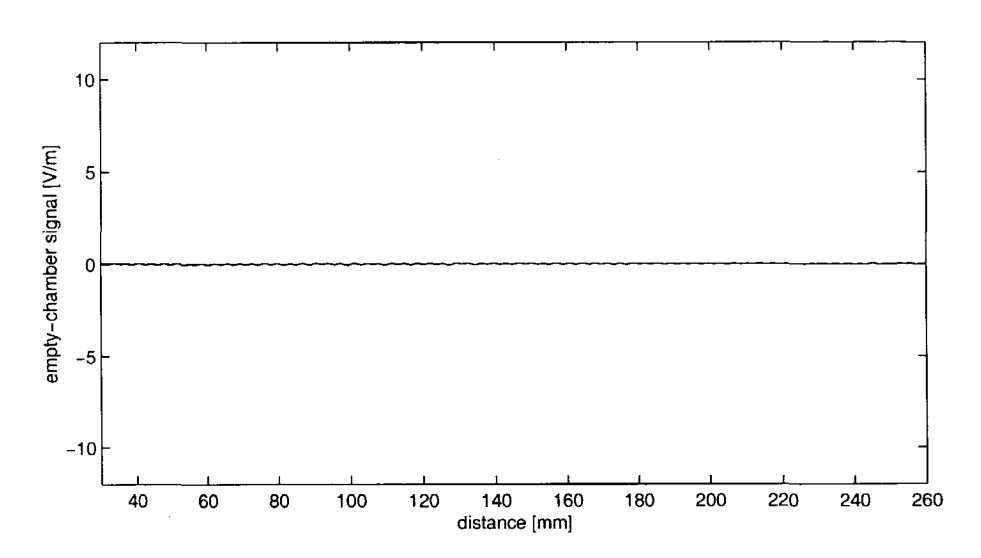


Figure 2.11: Reflections of the anechoic chamber without any object present.

an idea of the magnitude of these unwanted reflections we performed an experiment without a scattering object present. The results are shown in Fig. (2.11). The amplitude of this signal varies between -0.07 V/m and 0.07 V/m, which is considerable less than the discrepancies between the computer simulations and actual measurements of the field components.

Before discussing the results of measurements and computations, when a scattering object is present, we first develop in the next chapter the theoretical formulation and its resulting algorithm for computation of the scattered field from a finite object.



Chapter 3

Formulation of the Scattering Problem

In this chapter, we formulate the problem of scattering of an incident wave field by a finite object in free space. Using Lorentz's reciprocity theorem we derive integral representations for the electric and magnetic wave fields in terms of the tangential components of the electric and magnetic field on a closed surface. In particular, we derive integral representations for the incident and scattered electromagnetic fields. We simplify the representations for the scattered field by assuming that the scattering object under consideration is electrically perfectly conducting. Then, only the tangential components of the magnetic field are the fundamental unknown field quantities. Subsequently, we derive two types of boundary integral equations for this unknown surface field. In view of non-uniqueness problems, we also require consistency of the integral representations in the interior of the scattering object.

3.1. The scattering configuration

Consider the electromagnetic scattering by an arbitrary object occupying the domain D_{obj} with boundary surface ∂D_{obj} . The electromagnetic radiation originates from an antenna in a domain D_{ant} . The configuration is depicted in Fig. 3.1. The total electromagnetic field quantities E and H can be written as the sum of the incident and scattered fields, $E = E^{i} + E^{s}$,

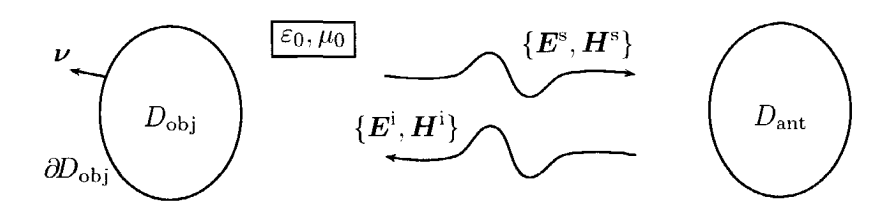


Figure 3.1: The scattering configuration.

 $H = H^{\rm i} + H^{\rm s}$, where the superscripts "i" and "s" denote the incident and scattered fields, respectively. These fields satisfy the Maxwell equations in the frequency domain in vacuum, viz.

$$\nabla \times \boldsymbol{H}(\boldsymbol{x}) + i\omega \varepsilon_0 \boldsymbol{E}(\boldsymbol{x}) = \boldsymbol{J}(\boldsymbol{x}), \qquad (3.1)$$

$$\nabla \times \boldsymbol{E}(\boldsymbol{x}) - i\omega \mu_0 \boldsymbol{H}(\boldsymbol{x}) = -\boldsymbol{K}(\boldsymbol{x}), \qquad (3.2)$$

where J is the volume density of the electric current and K is the volume density of the magnetic current.

3.2. Lorentz's reciprocity theorem

In order to derive the appropriate representations for the scattered fields we briefly state the essential steps to derive Lorentz's reciprocity theorem [2]. Consider the configuration as described in Fig. 3.2. The superscripts "a" and "b" denote fields somewhere in space due to the volume densities of the electric current $J^{a,b}$ and the magnetic current $K^{a,b}$ inside a closed domain D with boundary ∂D and the outward normal vector $\boldsymbol{\nu}$. These two field states are denoted as State A and State B, respectively. The fundamental interaction quantity between the two states is

$$\nabla \cdot (\mathbf{E}^{\mathbf{a}} \times \mathbf{H}^{\mathbf{b}} - \mathbf{E}^{\mathbf{b}} \times \mathbf{H}^{\mathbf{a}}) = \mathbf{H}^{\mathbf{b}} \cdot (\nabla \times \mathbf{E}^{\mathbf{a}}) - \mathbf{E}^{\mathbf{a}} \cdot (\nabla \times \mathbf{H}^{\mathbf{b}}) - \mathbf{H}^{\mathbf{a}} \cdot (\nabla \times \mathbf{E}^{\mathbf{b}}) + \mathbf{E}^{\mathbf{b}} \cdot (\nabla \times \mathbf{H}^{\mathbf{a}}). (3.3)$$

Subsequently after using Eq. (3.1) and Eq. (3.2) in Eq. (3.3) it becomes

$$\nabla \cdot (E^{a} \times H^{b} - E^{b} \times H^{a}) = E^{b} \cdot J^{a} - H^{b} \cdot K^{a} - E^{a} \cdot J^{b} + H^{a} \cdot K^{b}, (3.4)$$

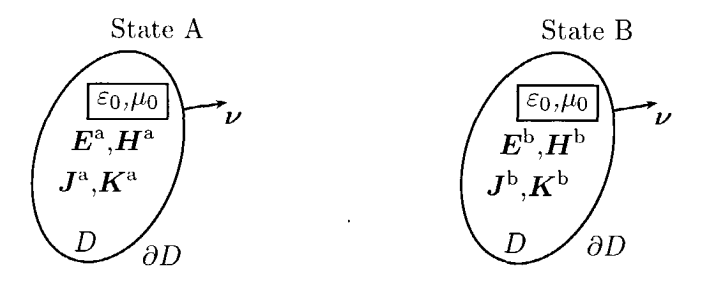


Figure 3.2: Configuration for the application of the reciprocity theorem.

which is Lorentz's reciprocity theorem in local form. Taking the integral over D and after applying Gauss' integral theorem to the left part of Eq. (3.4), it becomes now

$$\oint_{\partial D} (\mathbf{E}^{\mathbf{a}} \times \mathbf{H}^{\mathbf{b}} - \mathbf{E}^{\mathbf{b}} \times \mathbf{H}^{\mathbf{a}}) \cdot \boldsymbol{\nu} \, dA =$$

$$\int_{D} [\mathbf{E}^{\mathbf{b}} \cdot \mathbf{J}^{\mathbf{a}} - \mathbf{H}^{\mathbf{b}} \cdot \mathbf{K}^{\mathbf{a}} - \mathbf{E}^{\mathbf{a}} \cdot \mathbf{J}^{\mathbf{b}} + \mathbf{H}^{\mathbf{a}} \cdot \mathbf{K}^{\mathbf{b}}] \, dV, \quad (3.5)$$

being the global form of Lorentz's reciprocity theorem.

3.3. Electromagnetic Green's states

The desired representations are obtained when State A is chosen as the actual electromagnetic wave field in the configuration depicted in Fig. 3.2 and State B as the computational state, i.e. a state that is representative for the manner which the wave-field quantities in State A can be computed. To arrive at a Green's state we take a dipole source for State B.

For a dipole source at $x = x_p$, Maxwell's equations are written as

$$\nabla \times \boldsymbol{H}(\boldsymbol{x}) + i\omega \varepsilon_0 \boldsymbol{E}(\boldsymbol{x}) = \boldsymbol{j} \, \delta(\boldsymbol{x} - \boldsymbol{x}_p) \,,$$
 (3.6)

$$\nabla \times \boldsymbol{E}(\boldsymbol{x}) - i\omega \mu_0 \boldsymbol{H}(\boldsymbol{x}) = -\boldsymbol{k} \, \delta(\boldsymbol{x} - \boldsymbol{x}_p) \,. \tag{3.7}$$

in which j and k are arbitrary vectors, and $\delta(x_p)$ is the Dirac delta function. The electromagnetic field satisfying these equations are given by [2]

$$\boldsymbol{E}(\boldsymbol{x}) = \frac{-1}{i_{\nu} \varepsilon_0} [k_0^2 + \nabla \nabla \cdot] G(\boldsymbol{x} - \boldsymbol{x}_p) \, \boldsymbol{j} - \nabla \times G(\boldsymbol{x} - \boldsymbol{x}_p) \, \boldsymbol{k} \,, \tag{3.8}$$

$$\boldsymbol{H}(\boldsymbol{x}) = \frac{-1}{\mathrm{i}\omega\mu_0} [k_0^2 + \nabla\nabla] G(\boldsymbol{x} - \boldsymbol{x}_p) \, \boldsymbol{k} + \nabla \times G(\boldsymbol{x} - \boldsymbol{x}_p) \, \boldsymbol{j} \,. \tag{3.9}$$

where

$$G(\boldsymbol{x} - \boldsymbol{x}_p) = \frac{\exp(\mathrm{i}k_0|\boldsymbol{x} - \boldsymbol{x}_p|)}{4\pi|\boldsymbol{x} - \boldsymbol{x}_p|}.$$
 (3.10)

The electromagnetic Green's state $\{E^{Ge}, H^{Ge}\}$ is defined as the field that is generated by a dipole source of the electric type at $x = x_p$. Hence, $\{E^{Ge}, H^{Ge}\}$ satisfy

$$\nabla \times \boldsymbol{H}^{\text{Ge}}(\boldsymbol{x}) + i\omega \varepsilon_0 \boldsymbol{E}^{\text{Ge}}(\boldsymbol{x}) = \boldsymbol{j} \,\delta(\boldsymbol{x} - \boldsymbol{x}_p), \qquad (3.11)$$

$$\nabla \times \mathbf{E}^{\text{Ge}}(\mathbf{x}) - i\omega \mu_0 \mathbf{H}^{\text{Ge}}(\mathbf{x}) = \mathbf{0},$$
 (3.12)

The electromagnetic Green's state $\{E^{\rm Gm}, H^{\rm Gm}\}$ is defined as the field that is generated by a dipole source of the magnetic type at $x = x_p$. Hence, $\{E^{\rm Gm}, H^{\rm Gm}\}$ satisfy

$$\nabla \times \boldsymbol{H}^{Gm}(\boldsymbol{x}) + i\omega \varepsilon_0 \boldsymbol{E}^{Gm}(\boldsymbol{x}) = \boldsymbol{0},$$
 (3.13)

$$\nabla \times \mathbf{E}^{Gm}(\mathbf{x}) - i\omega \mu_0 \mathbf{H}^{Gm}(\mathbf{x}) = -\mathbf{k} \, \delta(\mathbf{x} - \mathbf{x}_p). \tag{3.14}$$

We can now write the solutions of Eq. (3.11) to Eq. (3.14) by means of Eq. (3.8) and Eq. (3.9) as

$$\boldsymbol{E}^{\text{Ge}} = \frac{-1}{\mathrm{i}\omega\varepsilon_0} [k_0^2 + \nabla_p \nabla_p \cdot] G(\boldsymbol{x} - \boldsymbol{x}_p) \boldsymbol{j}, \qquad (3.15)$$

$$\boldsymbol{H}^{\text{Ge}} = -\boldsymbol{\nabla}_{p} \times G(\boldsymbol{x} - \boldsymbol{x}_{p}) \boldsymbol{j}, \qquad (3.16)$$

$$\boldsymbol{E}^{\mathrm{Gm}} = \boldsymbol{\nabla}_{p} \times G(\boldsymbol{x} - \boldsymbol{x}_{p}) \boldsymbol{k}, \qquad (3.17)$$

$$\boldsymbol{H}^{\text{Gm}} = \frac{-1}{\mathrm{i}\omega\mu_0} [k_0^2 + \nabla_p \nabla_p \cdot] G(\boldsymbol{x} - \boldsymbol{x}_p) \boldsymbol{k}, \qquad (3.18)$$

in which the relation $\nabla = -\nabla_p$ has been used. Note that ∇_p denotes the spatial differentiation with respect to x_p .

3.4. General integral representations

In this section we derive general integral representation for the electromagnetic field quantities. Consider the configuration depicted in Fig. 3.3. It is assumed that no sources are present in the domain outside D. The sources that generate the electromagnetic field are assumed to be located inside D. While the domain D can be either $D_{\rm ant}$ or $D_{\rm obj}$, the domain ∂D is the boundary of D and the domain D' is defined as $D' = \Re^3 \setminus \{D \cup \partial D\}$. The boundary of D' consist of the surfaces $\partial D'_{\infty}$ (at infinity) and ∂D .

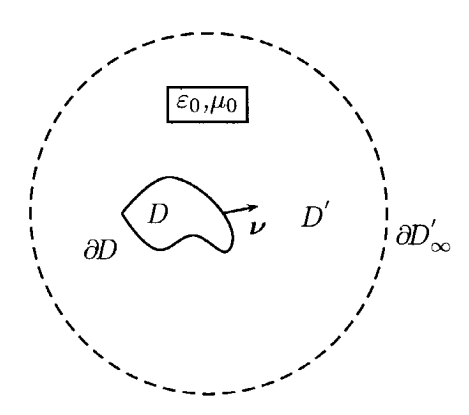


Figure 3.3: Configuration for application of reciprocity theorem.

Electric field

In order to derive a representation for the electric field we apply the reciprocity theorem. At the surface ∂D the normal ν is an inward normal to D', which results in an extra minus sign. Considering a field $\{E, H\}$ in State A and the electromagnetic Green's State $\{E^{\text{Ge}}, H^{\text{Ge}}\}$ in state B and applying the reciprocity theorem yields

$$-\oint_{\partial D} (\boldsymbol{E} \times \boldsymbol{H}^{\text{Ge}} - \boldsymbol{E}^{\text{Ge}} \times \boldsymbol{H}) \cdot \boldsymbol{\nu} \, dA = \int_{D'} -\boldsymbol{E} \cdot \boldsymbol{j} \delta(\boldsymbol{x} - \boldsymbol{x}_p) \, dV, \quad (3.19)$$

where x is the integration variable and the point, $x_p \in \{D', \partial D, D\}$, is an observation point. We have assumed that the integral over $\partial D'_{\infty}$ vanishes in view of the radiation conditions. The integral in the right-hand side of Eq. (3.19) is, after eliminating the minus sign, equal to $j \cdot E(x_p)$ when

 $x_p \in D'$, equal to $\frac{1}{2}j \cdot E(x_p)$ when $x_p \in \partial D$ and equal to 0 when $x_p \in D$. Hence,

$$\{1, \frac{1}{2}, 0\} \boldsymbol{j} \cdot \boldsymbol{E}(\boldsymbol{x}_p) = \oint_{\partial D} (\boldsymbol{E} \times \boldsymbol{H}^{Ge} - \boldsymbol{E}^{Ge} \times \boldsymbol{H}) \cdot \boldsymbol{\nu} \, dA.$$
 (3.20)

Substitution of the expressions for E^{Ge} and H^{Ge} of Eq. (3.15) and Eq. (3.16) into this equation yields

$$\{1, \frac{1}{2}, 0\} \boldsymbol{j} \cdot \boldsymbol{E}(\boldsymbol{x}_{p}) = \oint_{\partial D} \left\{ -\boldsymbol{E}(\boldsymbol{x}) \times [\boldsymbol{\nabla}_{p} \times G(\boldsymbol{x} - \boldsymbol{x}_{p}) \boldsymbol{j}] + \frac{1}{\mathrm{i}\omega\varepsilon_{0}} \left[k_{0}^{2} + \boldsymbol{\nabla}_{p} \boldsymbol{\nabla}_{p} \cdot] G(\boldsymbol{x} - \boldsymbol{x}_{p}) \boldsymbol{j} \times \boldsymbol{H}(\boldsymbol{x}) \right\} \cdot \boldsymbol{\nu} \, \mathrm{d}A, \quad (3.21)$$

We can rewrite the first expression of the integrand on the right-hand side of Eq. (3.21) as

$$\{-E(x) \times [\nabla_p \times G(x - x_p)j]\} \cdot \nu$$

$$= j \cdot \{\nabla_p \times [G(x - x_p)\nu \times E(x)]\}, (3.22)$$

and the second expression on the right-hand side of Eq. (3.21) as

$$\left\{ \frac{1}{\mathrm{i}\omega\varepsilon_0} [k_0^2 + \nabla_p \nabla_p \cdot] G(\boldsymbol{x} - \boldsymbol{x}_p) \boldsymbol{j} \times \boldsymbol{H}(\boldsymbol{x}) \right\} \cdot \boldsymbol{\nu} \\
= -\frac{1}{\mathrm{i}\omega\varepsilon_0} [k_0^2 + \nabla_p \nabla_p \cdot] G(\boldsymbol{x} - \boldsymbol{x}_p) [\boldsymbol{\nu} \times \boldsymbol{H}(\boldsymbol{x})] \cdot \boldsymbol{j} . \quad (3.23)$$

Using these relations in Eq. (3.21) and removing the arbitrary vector \boldsymbol{j} lead to the desired expression, viz.,

$$\{1, \frac{1}{2}, 0\} \boldsymbol{E}(\boldsymbol{x}_{p}) = \boldsymbol{\nabla}_{p} \times \oint_{\partial D} G(\boldsymbol{x} - \boldsymbol{x}_{p}) \boldsymbol{\nu} \times \boldsymbol{E}(\boldsymbol{x}) \, dA$$
$$- \frac{1}{\mathrm{i}\omega\varepsilon_{0}} [k_{0}^{2} + \boldsymbol{\nabla}_{p}\boldsymbol{\nabla}_{p} \cdot] \oint_{\partial D} G(\boldsymbol{x} - \boldsymbol{x}_{p}) \boldsymbol{\nu} \times \boldsymbol{H}(\boldsymbol{x}) \, dA, \quad (3.24)$$

when $x_p \in \{D', \partial D, D\}$.

Magnetic field

We derive now in the same way a representation for the magnetic field. Considering now a field $\{E, H\}$ as in state A and electromagnetic Green's

state $\{E^{\rm Gm}, H^{\rm Gm}\}$ in state B as described in Fig. 3.2, and applying the reciprocity theorem yields

$$-\oint_{\partial D} (\mathbf{E} \times \mathbf{H}^{Gm} - \mathbf{E}^{Gm} \times \mathbf{H}) \cdot \boldsymbol{\nu} \, dA = \int_{D'} \mathbf{H} \cdot \boldsymbol{k} \delta(\boldsymbol{x} - \boldsymbol{x}_p) \, dV, \quad (3.25)$$

where $x_p \in \{D', \partial D, D\}$. Similarly, Eq. (3.25) can now be rewritten as

$$\{1, \frac{1}{2}, 0\} \boldsymbol{k} \cdot \boldsymbol{H}(\boldsymbol{x}_p) = \oint_{\partial D} (\boldsymbol{E}^{Gm} \times \boldsymbol{H} - \boldsymbol{E} \times \boldsymbol{H}^{Gm}) \cdot \boldsymbol{\nu} \, dA, \qquad (3.26)$$

substitution of the expressions for $E^{\rm Gm}$ and $H^{\rm Gm}$ of Eq. (3.17) and Eq. (3.18) yields

$$\{1, \frac{1}{2}, 0\} \boldsymbol{k} \cdot \boldsymbol{H}(\boldsymbol{x}_p) = \oint_{\partial D} \left\{ [\boldsymbol{\nabla}_p \times G(\boldsymbol{x} - \boldsymbol{x}_p) \boldsymbol{k}] \times \boldsymbol{H}(\boldsymbol{x}) + \boldsymbol{E}(\boldsymbol{x}) \times \frac{1}{\mathrm{i}\omega\mu_0} [k_0^2 + \boldsymbol{\nabla}_p \boldsymbol{\nabla}_p \cdot] G(\boldsymbol{x} - \boldsymbol{x}_p) \boldsymbol{k} \right\} \cdot \boldsymbol{\nu} \, \mathrm{d}A. \quad (3.27)$$

We can rewrite the first expression of the integrand on the right-hand side of Eq. (3.27) as

$$\{ [\nabla_p \times G(\boldsymbol{x} - \boldsymbol{x}_p)\boldsymbol{k}] \times \boldsymbol{H}(\boldsymbol{x}) \} \cdot \boldsymbol{\nu}$$

$$= \boldsymbol{k} \cdot \{ \nabla_p \times [G(\boldsymbol{x} - \boldsymbol{x}_p)\boldsymbol{\nu} \times \boldsymbol{H}(\boldsymbol{x})] \} , (3.28)$$

and the second expression on the right hand side of Eq. (3.27) as

$$\left\{ \mathbf{E}(\mathbf{x}) \times \frac{1}{\mathrm{i}\omega\mu_0} [k_0^2 + \nabla_p \nabla_p \cdot] G(\mathbf{x} - \mathbf{x}_p) \mathbf{k} \right\} \cdot \mathbf{\nu}$$

$$= \frac{1}{\mathrm{i}\omega\mu_0} [k_0^2 + \nabla_p \nabla_p \cdot] G(\mathbf{x} - \mathbf{x}_p) [\mathbf{\nu} \times \mathbf{E}(\mathbf{x})] \cdot \mathbf{k} . \quad (3.29)$$

Using these relations in Eq. (3.27) and removing the arbitrary vector \mathbf{k} lead to the desired expression, viz.,

$$\{1, \frac{1}{2}, 0\} \boldsymbol{H}(\boldsymbol{x}_p) = \boldsymbol{\nabla}_p \times \oint_{\partial D} G(\boldsymbol{x} - \boldsymbol{x}_p) \boldsymbol{\nu} \times \boldsymbol{H}(\boldsymbol{x}) \, dA$$
$$+ \frac{1}{\mathrm{i}\omega u_0} [k_0^2 + \boldsymbol{\nabla}_p \boldsymbol{\nabla}_p \cdot] \oint_{\partial D} G(\boldsymbol{x} - \boldsymbol{x}_p) \boldsymbol{\nu} \times \boldsymbol{E}(\boldsymbol{x}) \, dA , \quad (3.30)$$

when $\boldsymbol{x}_p \in \{D', \partial D, D\}.$

3.5. Integral representations for scattered field

In the previous section we have obtained integral representations for the electromagnetic field quantities anywhere in space. We will now apply these results to our scattering problem. Instead of the domain D with boundary ∂D we now deal with a scattering object $D_{\rm obj}$ with boundary $\partial D_{\rm obj}$ (see Fig. 3.4), while the electromagnetic wavefield is denoted by $\{E^{\rm s}, H^{\rm s}\}$. Then, the general representations of Eqs. (3.24) and (3.30) for this special case are given by

$$\{1, \frac{1}{2}, 0\} \mathbf{E}^{s}(\mathbf{x}_{p}) = \nabla_{p} \times \oint_{\partial D_{\text{obj}}} G(\mathbf{x} - \mathbf{x}_{p}) \boldsymbol{\nu} \times \mathbf{E}^{s}(\mathbf{x}) \, dA$$
$$- \frac{1}{i\omega\varepsilon_{0}} [k_{0}^{2} + \nabla_{p} \nabla_{p} \cdot] \oint_{\partial D_{\text{obj}}} G(\mathbf{x} - \mathbf{x}_{p}) \boldsymbol{\nu} \times \mathbf{H}^{s}(\mathbf{x}) \, dA, \quad (3.31)$$

and

$$\{1, \frac{1}{2}, 0\} \boldsymbol{H}^{s}(\boldsymbol{x}_{p}) = \boldsymbol{\nabla}_{p} \times \oint_{\partial D_{\text{obj}}} G(\boldsymbol{x} - \boldsymbol{x}_{p}) \boldsymbol{\nu} \times \boldsymbol{H}^{s}(\boldsymbol{x}) \, dA$$
$$+ \frac{1}{\mathrm{i}\omega \mu_{0}} [k_{0}^{2} + \boldsymbol{\nabla}_{p} \boldsymbol{\nabla}_{p} \cdot] \oint_{\partial D_{\text{obj}}} G(\boldsymbol{x} - \boldsymbol{x}_{p}) \boldsymbol{\nu} \times \boldsymbol{E}^{s}(\boldsymbol{x}) \, dA, \quad (3.32)$$

where $\boldsymbol{x}_p \in \{D'_{\text{obj}}, \partial D_{\text{obj}}, D_{\text{obj}}\}.$

In order to obtain a representation for the scattered fields in terms of the total field, we apply the reciprocity theorem to the domain D_{obj} . The total field is the sum of the incident and scattered fields. We already have the integral representations for the scattered field. To obtain similar expressions for the incident field, we take the incident fields $\{E^i, H^i\}$ as state A. To obtain the expression for the electric field we choose the electromagnetic Green's state $\{E^{\text{Ge}}, H^{\text{Ge}}\}$ as in state B, with the result

$$\oint_{\partial D_{\text{obj}}} (\boldsymbol{E}^{\text{i}} \times \boldsymbol{H}^{\text{Ge}} - \boldsymbol{E}^{\text{Ge}} \times \boldsymbol{H}^{\text{i}}) \cdot \boldsymbol{\nu} \, dA = \int_{D_{\text{obj}}} -\boldsymbol{E}^{\text{i}} \cdot \boldsymbol{j} \delta(\boldsymbol{x} - \boldsymbol{x}_p \, dV, \quad (3.33)$$

which is, after substitution of $\{E^{\mathrm{Ge}}, H^{\mathrm{Ge}}\}$, equivalent with

$$-\{0, \frac{1}{2}, 1\} \boldsymbol{E}^{i}(\boldsymbol{x}_{p}) = \boldsymbol{\nabla}_{p} \times \oint_{\partial D_{\text{obj}}} G(\boldsymbol{x} - \boldsymbol{x}_{p}) \boldsymbol{\nu} \times \boldsymbol{E}^{i}(\boldsymbol{x}) \, dA$$
$$- \frac{1}{i\omega\varepsilon_{0}} [k_{0}^{2} + \boldsymbol{\nabla}_{p} \boldsymbol{\nabla}_{p}] \oint_{\partial D_{\text{obj}}} G(\boldsymbol{x} - \boldsymbol{x}_{p}) \boldsymbol{\nu} \times \boldsymbol{H}^{i}(\boldsymbol{x}) \, dA, \quad (3.34)$$

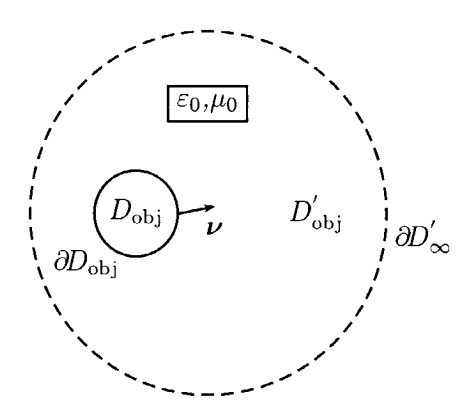


Figure 3.4: Configuration for application of reciprocity theorem, when the domain D encloses a scattering object.

where $x_p \in \{D'_{\text{obj}}, \partial D_{\text{obj}}, D_{\text{obj}}\}$. Addition of Eqs. (3.31) and (3.34) yields our desired representations

$$\begin{aligned} \{ \boldsymbol{E}^{\mathrm{s}}(\boldsymbol{x}_{p}), \, \frac{1}{2} [\boldsymbol{E}^{\mathrm{s}}(\boldsymbol{x}_{p}) - \boldsymbol{E}^{\mathrm{i}}(\boldsymbol{x}_{p})], \, -\boldsymbol{E}^{\mathrm{i}}(\boldsymbol{x}_{p}) \} \\ &= \nabla_{p} \times \oint_{\partial D_{\mathrm{obj}}} G(\boldsymbol{x} - \boldsymbol{x}_{p}) \boldsymbol{\nu} \times \boldsymbol{E}(\boldsymbol{x}) \, \mathrm{d}A \\ &- \frac{1}{\mathrm{i}\omega\varepsilon_{0}} [k_{0}^{2} + \nabla_{p}\nabla_{p} \cdot] \oint_{\partial D_{\mathrm{obj}}} G(\boldsymbol{x} - \boldsymbol{x}_{p}) \boldsymbol{\nu} \times \boldsymbol{H}(\boldsymbol{x}) \, \mathrm{d}A, \, (3.35) \end{aligned}$$

where $x_p \in \{D'_{\text{obj}}, \partial D_{\text{obj}}, D_{\text{obj}}\}.$

Similarly to find the representation for the magnetic field we choose the electromagnetic Green's state $\{E^{\rm Gm}, H^{\rm Gm}\}$ as in state B. We obtain then

$$\oint_{\partial D_{\text{obj}}} (\boldsymbol{E}^{\text{i}} \times \boldsymbol{H}^{\text{Gm}} - \boldsymbol{E}^{\text{Gm}} \times \boldsymbol{H}^{\text{i}}) \cdot \boldsymbol{\nu} \, dA = \int_{D_{\text{obj}}} \boldsymbol{H}^{\text{i}} \cdot \boldsymbol{k} \delta(\boldsymbol{x} - \boldsymbol{x}_p) \, dV, \quad (3.36)$$

which after substitution of $\{E^{\mathrm{Gm}}, H^{\mathrm{Gm}}\}$ is equivalent with

$$-\{0, \frac{1}{2}, 1\} \boldsymbol{H}^{i}(\boldsymbol{x}_{p}) = \nabla_{p} \times \oint_{\partial D_{\text{obj}}} G(\boldsymbol{x} - \boldsymbol{x}_{p}) \boldsymbol{\nu} \times \boldsymbol{H}^{i}(\boldsymbol{x}) \, dA$$

$$+ \frac{1}{i\omega\mu_{0}} [k_{0}^{2} + \nabla_{p}\nabla_{p} \cdot] \oint_{\partial D_{\text{obj}}} G(\boldsymbol{x} - \boldsymbol{x}_{p}) \boldsymbol{\nu} \times \boldsymbol{E}^{i}(\boldsymbol{x}) \, dA, \quad (3.37)$$

where $\dot{x}_p \in \{D'_{\text{obj}}, \partial D_{\text{obj}}, D_{\text{obj}}\}$. Addition of Eqs. (3.32) and (3.37) yields the desired representation

$$\begin{aligned} \{ \boldsymbol{H}^{\mathrm{s}}(\boldsymbol{x}_{p}), \ &\frac{1}{2} [\boldsymbol{H}^{\mathrm{s}}(\boldsymbol{x}_{p}) - \boldsymbol{H}^{\mathrm{i}}(\boldsymbol{x}_{p})], -\boldsymbol{H}^{\mathrm{i}}(\boldsymbol{x}_{p}) \} \\ &= \nabla_{p} \times \oint_{\partial D_{\mathrm{obj}}} G(\boldsymbol{x} - \boldsymbol{x}_{p}) \boldsymbol{\nu} \times \boldsymbol{H}(\boldsymbol{x}) \, \mathrm{d}A \\ &+ \frac{1}{\mathrm{i}\omega \mu_{0}} [k_{0}^{2} + \nabla_{p} \nabla_{p} \cdot] \oint_{\partial D_{\mathrm{obj}}} G(\boldsymbol{x} - \boldsymbol{x}_{p}) \boldsymbol{\nu} \times \boldsymbol{E}(\boldsymbol{x}) \, \mathrm{d}A, \quad (3.38) \end{aligned}$$

where $\boldsymbol{x}_p \in \{D'_{\text{obj}}, \partial D_{\text{obj}}, D_{\text{obj}}\}.$

3.5.1. Integral representations

At this point we are able to express the scattered fields outside the scattering object in terms of the total electric and magnetic fields on the surface of the scattering object by means of the following integral representations

$$\mathbf{E}^{\mathrm{s}}(\mathbf{x}_{p}) = \nabla_{p} \times \oint_{\partial D_{\mathrm{obj}}} G(\mathbf{x} - \mathbf{x}_{p}) \boldsymbol{\nu} \times \mathbf{E}(\mathbf{x}) \, \mathrm{d}A
- \frac{1}{\mathrm{i}\omega\varepsilon_{0}} [k_{0}^{2} + \nabla_{p}\nabla_{p}\cdot] \oint_{\partial D_{\mathrm{obj}}} G(\mathbf{x} - \mathbf{x}_{p}) \boldsymbol{\nu} \times \mathbf{H}(\mathbf{x}) \, \mathrm{d}A, \quad (3.39)$$

and

$$\boldsymbol{H}^{s}(\boldsymbol{x}_{p}) = \boldsymbol{\nabla}_{p} \times \oint_{\partial D_{\text{obj}}} G(\boldsymbol{x} - \boldsymbol{x}_{p}) \boldsymbol{\nu} \times \boldsymbol{H}(\boldsymbol{x}) \, dA$$
$$+ \frac{1}{\mathrm{i}\omega \mu_{0}} [k_{0}^{2} + \boldsymbol{\nabla}_{p} \boldsymbol{\nabla}_{p} \cdot] \oint_{\partial D_{\text{obj}}} G(\boldsymbol{x} - \boldsymbol{x}_{p}) \boldsymbol{\nu} \times \boldsymbol{E}(\boldsymbol{x}) \, dA, \quad (3.40)$$

where $x_p \in D'_{\text{obj}}$. These equations become simpler when we apply it for a perfectly conducting object. Applying the boundary condition $\nu \times E = 0$ gives

$$\boldsymbol{E}^{\mathrm{s}}(\boldsymbol{x}_{p}) = -\frac{1}{\mathrm{i}\omega\varepsilon_{0}}[k_{0}^{2} + \nabla_{p}\nabla_{p}\cdot] \oint_{\partial D_{\mathrm{obs}}} G(\boldsymbol{x} - \boldsymbol{x}_{p})\boldsymbol{\nu} \times \boldsymbol{H}(\boldsymbol{x}) \,\mathrm{d}A, \qquad (3.41)$$

and

$$\boldsymbol{H}^{\mathrm{s}}(\boldsymbol{x}_{p}) = \boldsymbol{\nabla}_{p} \times \oint_{\partial D_{\mathrm{obj}}} G(\boldsymbol{x} - \boldsymbol{x}_{p}) \boldsymbol{\nu} \times \boldsymbol{H}(\boldsymbol{x}) \, \mathrm{d}A, \qquad (3.42)$$

where $\boldsymbol{x}_p \in D'_{\text{obj}}$.

The integral representations for the scattered fields $E^{s}(x_{p})$ and $H^{s}(x_{p})$ now depend only on $\nu \times H$ at the boundary ∂D_{obj} .

3.5.2. Integral equations

The unknown $\nu \times H$ on ∂D_{obj} is a solution of an integral equation, obtained either from Eq. (3.35) or from Eq. (3.38), by letting the point of observation x_p on the surface ∂D of D and applying it for a perfectly conducting surface, viz.,

$$\frac{1}{2}\boldsymbol{E}(\boldsymbol{x}_{p}) = \boldsymbol{E}^{\mathsf{i}}(\boldsymbol{x}_{p})
- \frac{1}{\mathrm{i}\omega\varepsilon_{0}}[k_{0}^{2} + \boldsymbol{\nabla}_{p}\boldsymbol{\nabla}_{p}\cdot] \oint_{\partial D_{\mathrm{obj}}} G(\boldsymbol{x} - \boldsymbol{x}_{p})\boldsymbol{\nu} \times \boldsymbol{H}(\boldsymbol{x}) \,\mathrm{d}A, \quad (3.43)$$

and

$$\frac{1}{2}\boldsymbol{H}(\boldsymbol{x}_p) = \boldsymbol{H}^{i}(\boldsymbol{x}_p) + \boldsymbol{\nabla}_p \times \oint_{\partial D_{\text{obj}}} G(\boldsymbol{x} - \boldsymbol{x}_p) \boldsymbol{\nu} \times \boldsymbol{H}(\boldsymbol{x}) \, dA, \quad (3.44)$$

where in the left-hand sides the relations $E = E^{i} + E^{s}$ and $H = H^{i} + H^{s}$ are used. Subsequently, we take the cross product of these equations with the normal vector $\boldsymbol{\nu}_{p}$ and again applying the boundary condition $\boldsymbol{\nu}_{p} \times \boldsymbol{E}(\boldsymbol{x}_{p}) = \boldsymbol{0}$, we obtain the integral equations

$$\boldsymbol{\nu}_{p} \times \boldsymbol{E}^{i}(\boldsymbol{x}_{p}) = \boldsymbol{\nu}_{p} \times \frac{1}{i\omega\varepsilon_{0}} [k_{0}^{2} + \boldsymbol{\nabla}_{p}\boldsymbol{\nabla}_{p}\cdot] \oint_{\partial D_{\text{obj}}} G(\boldsymbol{x} - \boldsymbol{x}_{p})\boldsymbol{\nu} \times \boldsymbol{H}(\boldsymbol{x}) \, dA,$$
(3.45)

and

$$\nu_{p} \times \boldsymbol{H}^{i}(\boldsymbol{x}_{p}) = \frac{1}{2}\nu_{p} \times \boldsymbol{H}(\boldsymbol{x}_{p})$$

$$- \nu_{p} \times \left[\nabla_{p} \times \oint_{\partial D_{\text{obj}}} G(\boldsymbol{x} - \boldsymbol{x}_{p}) \boldsymbol{\nu} \times \boldsymbol{H}(\boldsymbol{x}) \, dA \right], \quad (3.46)$$

where $x_p \in \partial D_{\text{obj}}$.

These integral equations for $\nu \times H$ can be solved numerically and the results can be substituted in Eqs. (3.41) and (3.42) to arrive at the electromagnetic field anywhere outside the scattering object. Eq. (3.45) is an integral equation of the first kind and Eq. (3.46) is an integral equation of the second kind. In view of the advantageous properties of the integral equation of the second kind, we prefer this integral equation. Therefore, in this thesis we shall choose as point of departure the magnetic-field integral equation.

3.5.3. Interior representations

The solution of our integral equations is not-unique at certain frequencies of interior resonances [5, 6]. Nowadays, the standard technique to overcome this problem is a proper combination of the electric-field integral equation and the magnetic-field integral equation, see e.g. [10] and [11, 12]. The drawback is the extra computational burden of the electric-field integral equation. To overcome the non-uniqueness problem of the magnetic-field integral equation we require consistency inside the scattering object. For points inside the object, Eq. (3.38), together with the boundary condition that the tangential electric field vanishes, yields

$$H^{i}(\boldsymbol{x}_{p}) = -\nabla_{p} \times \oint_{S} G(\boldsymbol{x} - \boldsymbol{x}_{p}) \boldsymbol{\nu} \times H(\boldsymbol{x}) dA, \quad \boldsymbol{x}_{p} \in D_{\text{obj}}.$$
 (3.47)

However, it is not necessary to consider all the interior points. Let us consider a closed surface S_{int} that completely lies in the interior of D. When Eq. (3.47) is satisfied on this interior surface, both for the incident field and the Green function, we can use a convergent expansion in regular vector eigenfunctions inside and on this closed surface, and we may conclude that this equation holds inside $S_{\rm int}$ as well. Subsequently, in view of analytic continuation, Eq. (3.47) holds everywhere in the interior of the object. Hence, we may conclude that the satisfaction of the interior representation on a closed surface is a sufficient condition for uniqueness of the solution of the surface field $\nu \times H$ on the boundary of the object. Eq. (3.47) to be satisfied for all points on an interior surface S_{int} can be considered as a first kind of integral equation, and again we do not advocate to solve this ill-posed equation numerically. However, in the next chapter we show that this equation on an interior surface can be used advantageously as a sufficient error norm and hence as a constraint for the magnetic field integral equation, to overcome the non-uniqueness problems.

Chapter 4

Numerical Approach

In Chapter 3, we have derived, for a perfectly conducting object, the integral representations for the scattered fields E^s and H^s in terms of the tangential magnetic surface field. To compute this magnetic surface field, we also have derived a magnetic-field integral equation. Since the solution can only be found by numerical techniques we evaluate in this chapter both the integral representations and the integral equation numerically. In all expressions we have integrations over a surface of the boundary of the object, and for that reason we need the discretization of the geometry of the surface of the object.

4.1. Discretization of the geometry

For convenience, we denote the boundary surface of the object as $S = \partial D_{\text{obj}}$. Algebraic topology [25] tells us that the simplex triangle is the most fundamental shape to divide the surface S into a finite number of elementary surface elements. For this reason we discretize S into planar, triangular surface elements who span S. Let $\{S_n; n=1,2,\ldots,N\}$ be the collection of planar triangles, then

$$S \approx \bigcup_{n=1}^{N} S_n. \tag{4.1}$$

We take the orientation of the triangle such that the direction of circulation and the unit vector along the outward normal to S_n form a right-handed system. We use a local numbering of the vertices of S_n which carry the

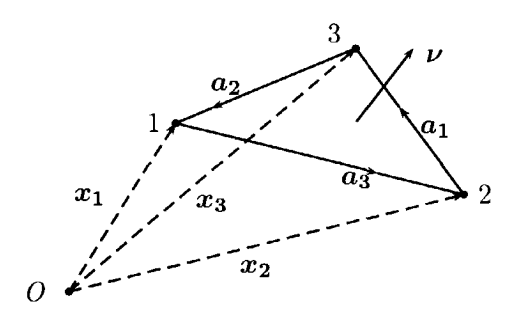


Figure 4.1: Spatial view of S_n with normal ν .

labels $\{1,2,3\}$. The computation is taken to the direction of the circulation. We further introduce the position vectors of its vertices with respect to the origin of the chosen background Cartesian reference frame. A spatial view of S_n is shown in Fig. 4.1. The vectorial edges $\{a_i; i=1,2,3\}$ of the triangle are defined with the aid of the position vectors as

$$a_i = x_k - x_j$$
, with $\{i, j, k\} = \text{cycl}\{1, 2, 3\},$ (4.2)

and the vectorial area of S_n can be expressed in terms of the vectorial edges through

$$\boldsymbol{A} = \frac{1}{2} [\boldsymbol{x_i} - \boldsymbol{x_k}] \times [\boldsymbol{x_j} - \boldsymbol{x_i}] = \frac{1}{2} \boldsymbol{a_j} \times \boldsymbol{a_k}, \quad \text{with } \{i, j, k\} = \text{cycl}\{1, 2, 3\},$$
(4.3)

and the unit vector $\boldsymbol{\nu}$ along the normal to S_n follows from

$$\nu = \frac{A}{A},\tag{4.4}$$

where A denotes the scalar area of S_n which is given by

$$A = [\mathbf{A} \cdot \mathbf{A}]^{\frac{1}{2}}. \tag{4.5}$$

In Appendix A, we derive a linear interpolation function to express any quantity in the interior and on the boundary of each planar triangle S_n , viz.,

$$\Phi_{n,i}(\boldsymbol{x}) = \frac{1}{3} - \frac{(\boldsymbol{x} - \boldsymbol{b_n}) \cdot \boldsymbol{L_{n,i}}}{2A_n},$$
(4.6)

in which b_n is the position vector of the barycenter of S_n and $L_{n,i}$ are the vectors normal to the respective edges in the plane of S_n , and A_n is the

scalar area of S_n . On S_n any vectorial function F(x) can be expanded as

$$F(x) = \sum_{i=1}^{3} F(x_i) \Phi_{n,i}(x)$$
. (4.7)

With the result,

$$\int_{S_n} \Phi_{n,i}(\mathbf{x}) dA = \frac{A_n}{3}, \quad i = 1, 2, 3,$$
(4.8)

the integral over a linear vector function F(x) is obtained as

$$\int_{S_n} \mathbf{F}(\mathbf{x}) dA = \frac{A_n}{3} \sum_{i=1}^3 \mathbf{F}(\mathbf{x}_i).$$
 (4.9)

This latter integration rule is used extensively in our discretization procedure. All integrals over the object surface S of a vector function F(x) are replaced by

$$\oint_{S} \mathbf{F}(\mathbf{x}) dA = \sum_{n=1}^{N} \sum_{i=1}^{3} \frac{A_{n}}{3} \mathbf{F}(\mathbf{x}_{n,i}), \qquad (4.10)$$

where $x_{n,i}$ denotes the nodal point with ordinal number i on the triangle with ordinal number n.

4.2. Discretization of integral representations

For a perfectly conducting object the integral representations for the scattered fields E^s and H^s are derived in Chapter 3 as

$$\mathbf{E}^{\mathrm{s}}(\mathbf{x}_{p}) = -\frac{1}{\mathrm{i}\omega\varepsilon_{0}}[k_{0}^{2} + \nabla_{p}\nabla_{p}\cdot] \oint_{S} G(\mathbf{x} - \mathbf{x}_{p})[\boldsymbol{\nu} \times \boldsymbol{H}](\mathbf{x}) \,\mathrm{d}A, \quad (4.11)$$

$$H^{s}(\boldsymbol{x}_{p}) = \nabla_{p} \times \oint_{S} G(\boldsymbol{x} - \boldsymbol{x}_{p})[\boldsymbol{\nu} \times \boldsymbol{H}](\boldsymbol{x}) dA,$$
 (4.12)

where $x_p \in D'_{\text{obj}}$ is the observation variable and $x \in S (= \partial D_{\text{obj}})$ is the integration variable. The integrations in these representations must be solved numerically. Since for points outside the scattering object the Green function is not singular, we can discretize the integrals straightforwardly. After

interchanging the order of differentiation and integration, we obtain

$$\mathbf{E}^{\mathrm{s}}(\mathbf{x}_{p}) = -\frac{1}{\mathrm{i}\omega\varepsilon_{0}} \sum_{n=1}^{N} \sum_{i=1}^{3} \frac{A_{n}}{3} [k_{0}^{2}G(\mathbf{x}_{n,i} - \mathbf{x}_{p}) + \nabla_{p}\nabla_{p}G(\mathbf{x}_{n,i} - \mathbf{x}_{p}) \cdot] [\boldsymbol{\nu} \times \boldsymbol{H}](\mathbf{x}_{n,i}), \qquad (4.13)$$

$$\boldsymbol{H}^{s}(\boldsymbol{x}_{p}) = \sum_{n=1}^{N} \sum_{i=1}^{3} \frac{A_{n}}{3} \nabla_{p} G(\boldsymbol{x}_{n,i} - \boldsymbol{x}_{p}) \times [\boldsymbol{\nu} \times \boldsymbol{H}](\boldsymbol{x}_{n,i}). \tag{4.14}$$

The summation with respect to n denotes the summation over the triangles, while the summation with respect to i denotes the summation over the particular nodes of the triangle with ordinal number n.

In these equations we have differentiations with respect to x_p which has to be carried out. The first derivative is obtained as [2]

$$\nabla_{p}G(\boldsymbol{x}-\boldsymbol{x}_{p}) = \frac{\exp(\mathrm{i}k_{0}|\boldsymbol{x}-\boldsymbol{x}_{p}|)}{4\pi|\boldsymbol{x}-\boldsymbol{x}_{p}|} \left[\mathrm{i}k_{0} - \frac{1}{|\boldsymbol{x}-\boldsymbol{x}_{p}|} \right] \boldsymbol{\Theta}_{\boldsymbol{p}}, \quad (4.15)$$

and the second derivative as

$$\nabla_{p}\nabla_{p}G(\boldsymbol{x}-\boldsymbol{x}_{p})\cdot[\boldsymbol{\nu}\times\boldsymbol{H}](\boldsymbol{x})$$

$$\stackrel{\cdot}{=} G(\boldsymbol{x}-\boldsymbol{x}_{p})\left[-\frac{(1-3\boldsymbol{\Theta}_{p}\boldsymbol{\Theta}_{p}\cdot)}{|\boldsymbol{x}-\boldsymbol{x}_{p}|^{2}}+\frac{\mathrm{i}k_{0}(1-3\boldsymbol{\Theta}_{p}\boldsymbol{\Theta}_{p}\cdot)}{|\boldsymbol{x}-\boldsymbol{x}_{p}|}\right]$$

$$-k_{0}^{2}\boldsymbol{\Theta}_{p}\boldsymbol{\Theta}_{p}\cdot\right][\boldsymbol{\nu}\times\boldsymbol{H}](\boldsymbol{x}),$$

$$(4.16)$$

in which

$$\Theta_{p} = \nabla_{p}|x - x_{p}| = -\frac{x - x_{p}}{|x - x_{p}|}$$

$$(4.17)$$

is the unit vector in the negative $(x - x_p)$ -direction.

4.3. Discretization of integral equations

As argued in the previous chapter, we only consider the magnetic-field integral equation given by

$$\nu_p \times \boldsymbol{H}^{i}(\boldsymbol{x}_p) = \frac{1}{2}\nu_p \times \boldsymbol{H}(\boldsymbol{x}_p) - \nu_p \times \left[\nabla_p \times \oint_S G(\boldsymbol{x} - \boldsymbol{x}_p)[\boldsymbol{\nu} \times \boldsymbol{H}](\boldsymbol{x}) \, \mathrm{d}A \right], \qquad (4.18)$$

in which the point of observation x_p is taken at the surface S. Studying the kernel in more detail, we observe that it is a bounded, continuous function of x and x_p , except for $x = x_p$, where it is not defined. When both points x and x_p are located on a planar surface area and do not coincide, the kernel function vanishes. In view of the continuity of the kernel, it is allowed to replace the Green function in a discretized configuration by its spherical mean [26], and this weak form of the Green function is defined everywhere, including the point $x = x_p$. In this thesis we operate a little different. A simpler procedure is to take only the mean of $1/|x - x_p|$ over a spherical domain with a radius of Δ , where Δ is the average sampling width of the discretized surface. Then our weak form of the derivative of the Green function is obtained as (see Appendix B)

$$\nabla_{p}\mathcal{G}(\boldsymbol{x}-\boldsymbol{x}_{p}) = -(\boldsymbol{x}-\boldsymbol{x}_{p})\partial G(|\boldsymbol{x}-\boldsymbol{x}_{p}|)$$
(4.19)

with

$$\partial G(R) = \begin{cases} (\mathrm{i}k_0 R - 1) \frac{\exp(\mathrm{i}k_0 R)}{4\pi\Delta^3}, & \text{when } 0 \le R < \Delta, \\ (\mathrm{i}k_0 R - 1) \frac{\exp(\mathrm{i}k_0 R)}{4\pi R^3}, & \text{when } \Delta \le R < \infty. \end{cases}$$
(4.20)

Since this weak form of the Green function is continuous and bounded everywhere, we are able discretize the integral of Eq. (4.18) straightforwardly, using a linear interpolation of integrand. After interchanging the order of differentiation and integration, we obtain

$$\nu_p \times \boldsymbol{H}^{\mathrm{i}}(\boldsymbol{x}_p) = \frac{1}{2}\nu_p \times \boldsymbol{H}(\boldsymbol{x}_p) \\ -\nu_p \times \left[\sum_{n=1}^{N} \sum_{i=1}^{3} \frac{A_n}{3} \nabla_p \mathcal{G}(\boldsymbol{x}_{n,i} - \boldsymbol{x}_p) \times [\boldsymbol{\nu} \times \boldsymbol{H}](\boldsymbol{x}_{n,i}) \right]. (4.21)$$

The summation with respect to n denotes the summation over the triangles, while the summation with respect to i denotes the summation over the particular nodes of the triangle with ordinal number n. Finally, we consider a finite set of equations by requiring consistency in each node j of a each triangle m with normal vector $\boldsymbol{\nu}_m$. We then end up with a linear set of equations

$$[\boldsymbol{\nu} \times \boldsymbol{H}^{i}](\boldsymbol{x}_{m,j}) = \frac{1}{2}[\boldsymbol{\nu} \times \boldsymbol{H}](\boldsymbol{x}_{m,j}) - \boldsymbol{\nu}_{m} \times \left[\sum_{n=1}^{N} \sum_{i=1}^{3} \frac{A_{n}}{3} \nabla_{p} \mathcal{G}(\boldsymbol{x}_{n,i} - \boldsymbol{x}_{m,j}) \times [\boldsymbol{\nu} \times \boldsymbol{H}](\boldsymbol{x}_{n,i}) \right], m = 1, 2, \dots, N, \quad j = 1, 2, 3.$$
 (4.22)

Note that in Eq. (4.22), $\nabla_p \mathcal{G}(\boldsymbol{x}_{n,i} - \boldsymbol{x}_{m,j})$ denotes the value of $\nabla_p \mathcal{G}(\boldsymbol{x}_{n,i} - \boldsymbol{x}_p)$ when $\boldsymbol{x}_p = \boldsymbol{x}_{m,j}$. This is a linear system of 6N equations for the 6N unknown surface field quantities, $\boldsymbol{\nu} \times \boldsymbol{H}$, at the 3N nodal points $\boldsymbol{x}_{n,i}$. In view of our application we are interested in objects which are large compared to the wavelength of the incident field. In practice, we need at least five to six discretization points per wavelength [27]. Hence, for large objects, the storage of the system matrix and its inversion becomes unrealistic with the present-day computer power. We therefore aim for an iterative solution of the system of equations. Starting with the (high-frequency) physical-optics approximation [3], where we take the surface field

$$[\boldsymbol{\nu} \times \boldsymbol{H}](\boldsymbol{x}_{m,j}) = 2 [\boldsymbol{\nu} \times \boldsymbol{H}^{i}](\boldsymbol{x}_{m,j}), \qquad (4.23)$$

on the 'illuminated' part of the object surface, and equal to zero on the 'dark' part of the object, we anticipate that a conjugate gradient scheme would be able to compute an improved approximation efficiently, within some imposed error criterion.

4.4. Conjugate gradient method

In this section we discuss the iterative solution of Eq. (4.22) using a conjugate gradient scheme. For the description it is convenient to introduce a operator notation, an inner product and a norm. We start with writing Eq. (4.22) in an operator form by introducing a linear operator \mathcal{L} acting on a vector function $[\nu \times \mathbf{H}]$ as

$$\mathcal{L}[\boldsymbol{\nu} \times \boldsymbol{H}] = [\boldsymbol{\nu} \times \boldsymbol{H}^{i}], \quad \text{on } S, \tag{4.24}$$

where

$$\mathcal{L}[\nu \times H] = \frac{1}{2}[\nu \times H] + \mathcal{K}[\nu \times H]. \tag{4.25}$$

Here, the operator \mathcal{K} acting on $[\nu \times H]$ is defined as

$$\mathcal{K}[\boldsymbol{\nu} \times \boldsymbol{H}] \equiv \boldsymbol{\nu}_{m} \times \left[\sum_{n=1}^{N} \sum_{i=1}^{3} \frac{A_{n}}{3} \nabla \mathcal{G}(\boldsymbol{x}_{n,i} - \boldsymbol{x}_{m,j}) \times [\boldsymbol{\nu} \times \boldsymbol{H}]_{n,i} \right],$$

$$m = 1, 2, \dots, N, \quad j = 1, 2, 3, \qquad (4.26)$$

with

$$[\boldsymbol{\nu} \times \boldsymbol{H}]_{n,i} \equiv [\boldsymbol{\nu} \times \boldsymbol{H}](\boldsymbol{x}_{n,i}), \quad n = 1, 2, \dots, N, \quad i = 1, 2, 3, (4.27)$$

while the known vector is defined as

$$[\boldsymbol{\nu} \times \boldsymbol{H}^{i}] \equiv [\boldsymbol{\nu} \times \boldsymbol{H}^{i}](\boldsymbol{x}_{m,j}), \quad m = 1, 2, \dots, N, \quad j = 1, 2, 3.$$
 (4.28)

Note that in Eq. (4.26), $\nabla \mathcal{G}(\boldsymbol{x}_{n,i} - \boldsymbol{x}_{m,j})$ denotes the value of $\nabla \mathcal{G}(\boldsymbol{x} - \boldsymbol{x}_{m,j})$ when $\boldsymbol{x} = \boldsymbol{x}_{n,i}$. The gradient acting on the Green function denotes now the spatial differentiation with respect to $\boldsymbol{x}_{n,i}$. Further, we define an inner product of two vector functions on S as

$$\langle [\boldsymbol{\nu} \times \boldsymbol{f}], [\boldsymbol{\nu} \times \boldsymbol{g}] \rangle_{S} \equiv \sum_{n=1}^{N} \sum_{i=1}^{3} \frac{A_{n}}{3} [\boldsymbol{\nu} \times \boldsymbol{f}] (\boldsymbol{x}_{n,i}) \cdot [\boldsymbol{\nu} \times \boldsymbol{g}] (\boldsymbol{x}_{n,i}), \quad (4.29)$$

where the overline denotes complex conjugate. The norm is defined as

$$\|\boldsymbol{\nu} \times \boldsymbol{f}\|_{S} = \left[\langle [\boldsymbol{\nu} \times \boldsymbol{f}], [\boldsymbol{\nu} \times \boldsymbol{f}] \rangle_{S} \right]^{\frac{1}{2}}. \tag{4.30}$$

We also need an adjoint operator \mathcal{L}^{\star} defined via the inner product as

$$\langle [\boldsymbol{\nu} \times \boldsymbol{f}], \boldsymbol{\mathcal{L}}[\boldsymbol{\nu} \times \boldsymbol{g}] \rangle_S = \langle \boldsymbol{\mathcal{L}}^*[\boldsymbol{\nu} \times \boldsymbol{f}], [\boldsymbol{\nu} \times \boldsymbol{g}] \rangle_S.$$
 (4.31)

This adjoint operator is obtained as

$$\mathcal{L}^{\star}[\nu \times f] = \frac{1}{2}[\nu \times f] + \mathcal{K}^{\star}[\nu \times f]. \tag{4.32}$$

with

$$\mathcal{K}^{\star}[
u imes f]$$

$$\equiv \boldsymbol{\nu}_{m} \times \left\{ \boldsymbol{\nu}_{m} \times \left[\sum_{n=1}^{N} \sum_{i=1}^{3} \frac{A_{n}}{3} \nabla \overline{\mathcal{G}}(\boldsymbol{x}_{n,i} - \boldsymbol{x}_{m,j}) \times \{\boldsymbol{\nu}_{n} \times [\boldsymbol{\nu} \times \boldsymbol{f}]_{n,i} \} \right] \right\},$$

$$m = 1, 2, \dots, N, \quad j = 1, 2, 3. \tag{4.33}$$

With these definitions we now formulate the conjugate gradient scheme that minimizes iteratively the error norm

$$[\operatorname{ERR}_S]^2 = \frac{\|\boldsymbol{\rho}\|_S^2}{\|\boldsymbol{\nu} \times \boldsymbol{H}^{\mathsf{i}}\|_S^2}, \tag{4.34}$$

where the residual error on S is defined as

$$\rho = [\nu \times \mathbf{H}^{i}] - \mathcal{L}[\nu \times \mathbf{H}]. \tag{4.35}$$

We start the conjugate gradient scheme with the physical-optics approximation, Eq. (4.23), as initial estimate, denoted by $[\nu \times H]^{(0)}$. Then, it computes

$$\rho^{(0)} = [\boldsymbol{\nu} \times \boldsymbol{H}^{\mathrm{i}}] - \boldsymbol{\mathcal{L}}[\boldsymbol{\nu} \times \boldsymbol{H}]^{(0)}.$$

Next the scheme chooses

$$m{v}^{(1)} = m{g}^{(1)} = m{\mathcal{L}}^{\star} m{
ho}^{(0)} \,, \quad m{lpha}^{(1)} = rac{\langle m{
ho}^{(0)}, m{\mathcal{L}} m{v}^{(1)}
angle_S}{\|m{\mathcal{L}} m{v}^{(1)}\|_S^2} \,,$$

with the updates

$$[\boldsymbol{\nu} \times \boldsymbol{H}]^{(1)} = [\boldsymbol{\nu} \times \boldsymbol{H}]^{(0)} + \alpha^{(1)} \boldsymbol{v}^{(1)}, \quad \boldsymbol{\rho}^{(1)} = \boldsymbol{\rho}^{(0)} - \alpha^{(1)} \boldsymbol{\mathcal{L}} \boldsymbol{v}^{(1)},$$

and computes successively for $p=2,3,\ldots,P$,

$$m{g}^{(p)} = m{\mathcal{L}}^{\star} m{
ho}^{(p-1)} \,, \quad m{v}^{(p)} = m{g}^{(p)} + rac{\|m{g}^{(p)}\|_S^2}{\|m{g}^{(p-1)}\|_S^2} \, m{v}^{(p-1)} \,,$$

$$lpha^{(p)} = rac{\langle oldsymbol{
ho}^{(p-1)}, oldsymbol{\mathcal{L}} oldsymbol{v}^{(p)}
angle_S}{\| oldsymbol{\mathcal{L}} oldsymbol{v}^{(p)} \|_S^2} \,,$$

with the updates

$$[\nu \times H]^{(p)} = [\nu \times H]^{(p-1)} + \alpha^{(p)} v^{(p)}, \quad \rho^{(p)} = \rho^{(p-1)} - \alpha^{(p)} \mathcal{L} v^{(p)}.$$

In fact, this conjugate gradient scheme solves iteratively the symmetrized integral equation

$$\mathcal{L}^{\star}\mathcal{L}[\nu \times H] = \mathcal{L}^{\star}[\nu \times H^{i}], \quad \text{on } S,$$
(4.36)

When this integral equation is uniquely solvable, the symmetrized operator $\mathcal{L}^{\star}\mathcal{L}$ does not have a null-space and is positive, so that the conjugate gradient scheme (for the non-discretized problem) converges to the exact solution [28, 29]

4.4.1. An additional error criterion

From Chapter 3, we also know that on an interior closed surface $S_{\rm int}$ the interior representation of Eq. (3.47) should hold. We therefore define an additional error criterion

$$ERR_{S_{int}} = \frac{\|\boldsymbol{\rho}_{int}\|_{S_{int}}}{\|\boldsymbol{H}^{i}\|_{S_{int}}},$$
(4.37)

where the residual error on S_{int} is defined as

$$\rho_{\text{int}}(\boldsymbol{x}_p) = \boldsymbol{H}^{\text{i}}(\boldsymbol{x}_p) + \boldsymbol{\nabla}_p \times \oint_{S} G(\boldsymbol{x} - \boldsymbol{x}_p) \boldsymbol{\nu} \times \boldsymbol{H}(\boldsymbol{x}) \, dA.$$
 (4.38)

Since the precise form of the interior surface is not important, we subdivide $S_{\rm int}$ is into $N_{\rm int}$ planar triangles $S_{{\rm int},m}$ and we require consistency of the interior integral representation at one single point on each patch. On each planar triangle we determine the barycenter as

$$\boldsymbol{b}_{m} = \frac{1}{3} \sum_{j=1}^{3} \boldsymbol{x}_{m,j} \,. \tag{4.39}$$

Then our discrete error norm is defined as

$$ERR_{S_{int}} = \frac{\sum_{m=1}^{N_{int}} \|\boldsymbol{\rho}_{int}(\boldsymbol{b}_m)\|^2}{\sum_{m=1}^{N_{int}} \|\boldsymbol{H}^{i}(\boldsymbol{b}_m)\|^2},$$
(4.40)

while the discretized residual error at a point $\boldsymbol{b_m} \in S_{\mathrm{int}}$ is given by

$$\boldsymbol{\rho}_{\text{int}}(\boldsymbol{b}_{m}) = H^{\text{i}}(\boldsymbol{b}_{m}) - \sum_{n=1}^{N} \sum_{i=1}^{3} \frac{A_{n}}{3} \nabla \mathcal{G}(\boldsymbol{x}_{n,i} - \boldsymbol{b}_{m}) \times [\boldsymbol{\nu} \times \boldsymbol{H}]_{n,i},$$

$$m = 1, 2, \dots, N_{\text{int}}. \tag{4.41}$$

We shall use this additional error norm as a check of the numerical results.

In order to guarantee that in the discretized counterpart of $S_{\rm int}$ the field variation is computable within the present computer accuracy, we take care that $S_{\rm int}$ encloses a sphere with a diameter of a half wavelength, and on $S_{\rm int}$ we take a discretization of five to six points per wavelength. Taking a larger interior surface and/or a finer is discretization is always allowed, but it will increase the computation time without any benefit.

4.4.2. Numerical example of a sphere

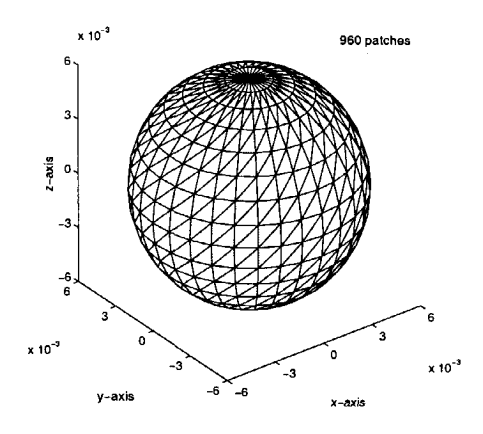
As a first test example we consider the scattering of a plane wave by a perfectly conducting sphere with radius a. We assume that its center coincides with the origin of our coordinate system. For this particular scattering problems analytical results are available. In a spherical coordinate system, the incident and the scattered field are expanded in terms of regular and singular vector eigenfunctions, respectively. Each term of this type of expansions satisfies Maxwell equations in spherical coordinates. The coefficients of the scattered-field expansions (Mie series [23]) are obtained by requiring the boundary condition that the tangential electric field vanish at a radial coordinate r=a. For comparison we have computed the tangential magnetic field at the boundary of the sphere in terms of these Mie series.

The incident plane wave is obtained by putting our dipole antenna (see Chapter 2) very far from our scattering object and normalizing the results with the normalization factor $4\pi r/(k_0I_{ant})$, where r is the distance between the antenna and the origin of the coordinate system. For our examples we take r=1000 m. The wave is travelling in the negative z-direction towards the scattering object. We take the polarization of the electric field in the x-direction and in the y-direction, respectively.

In the several figures in this chapter, we present the error only for the case that the electric field of the incident wave is polarized in the y-direction.

We consider three frequencies of operation, such that the normalized wave numbers are $k_0a=4$, 4.973 and 6, respectively. At $k_0a=4.973$ a spurious solution can occur due to the non-uniqueness of the magnetic field equation at the eigenfrequency of an interior resonance. We discretize the boundary surface S of the sphere in 960 plane triangles patches (see Fig. 4.2).

In Fig. 4.4 (top), we present the normalized error norm, ERR_S, as a function of the number of iterations. From this figure we observe that the error on S in the conjugate gradient scheme remains decreasing, although at an interior resonance ($k_0a = 4.973$) with a much slower speed. To investigate the problem of the occurrence of a spurious field solution related to the occurrence of an interior resonance in more detail, we compute our additional error norm over an interior surface $S_{\rm int}$ as well. To save computation time the interior surface $S_{\rm int}$ is taken as small as possible, but this surface should be large enough such that the field variation of the incident field is visible within



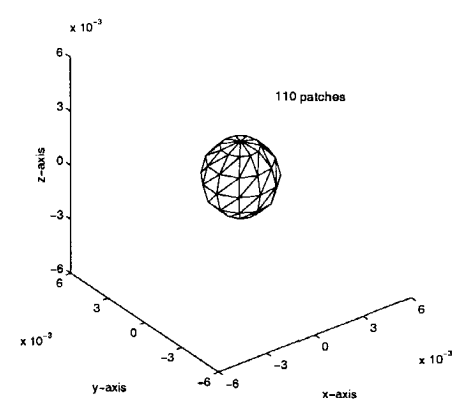


Figure 4.2: Sphere of radius a = 6 mm, discretized in 960 patches.

Figure 4.3: Interior sphere of radius $\frac{1}{3}a$, discretized in 110 patches.

numerical accuracy. Here, we take a sphere with a radius of $\frac{1}{3}a$, subdivided in 110 plane triangular patches (see Fig. 4.3). The extra computation time to compute the error on $S_{\rm int}$ is less than 3%. In Fig. 4.4 (bottom), we present the normalized error on the interior surface $S_{\rm int}$, ERR $_{S_{\rm int}}$, as a function of the number of iterations of the conjugate gradient scheme. From this figure it appears that the final error on $S_{\rm int}$ is more indicative for the actual error due to the discretization of integral equation on S and the presence of an interior resonance. At the interior resonance ($k_0a = 4.973$) we clearly observe an increase of the error at iterations where the conjugate gradient scheme adds field components of the interior resonance to the actual surface field.

For $k_0a = 4.973$, in Fig. 4.5, we present the absolute value of the surface field $\nu \times H$ as a function of the angular coordinate along the surface of the sphere in the cross-sectional plane x = 0, for a increasing number, p, of iterations. We consider the two cases of polarization, viz., an incident plane wave with electric field in the x-direction and an incident plane wave with electric field in the y-direction. To compare the results we have also presented the results obtained from an analytical solution of the scattering problem of the sphere in terms of the Mie-series [23]. In each figure, these analytical results are represented by the heavy solid line. In accordance with the results of our additional interior error criterion given in Fig. 4.4 (bottom) we observe that for increasing number of iterations up to p = 10 - 17 the results are approximating the analytical results, but from p = 17 the surface

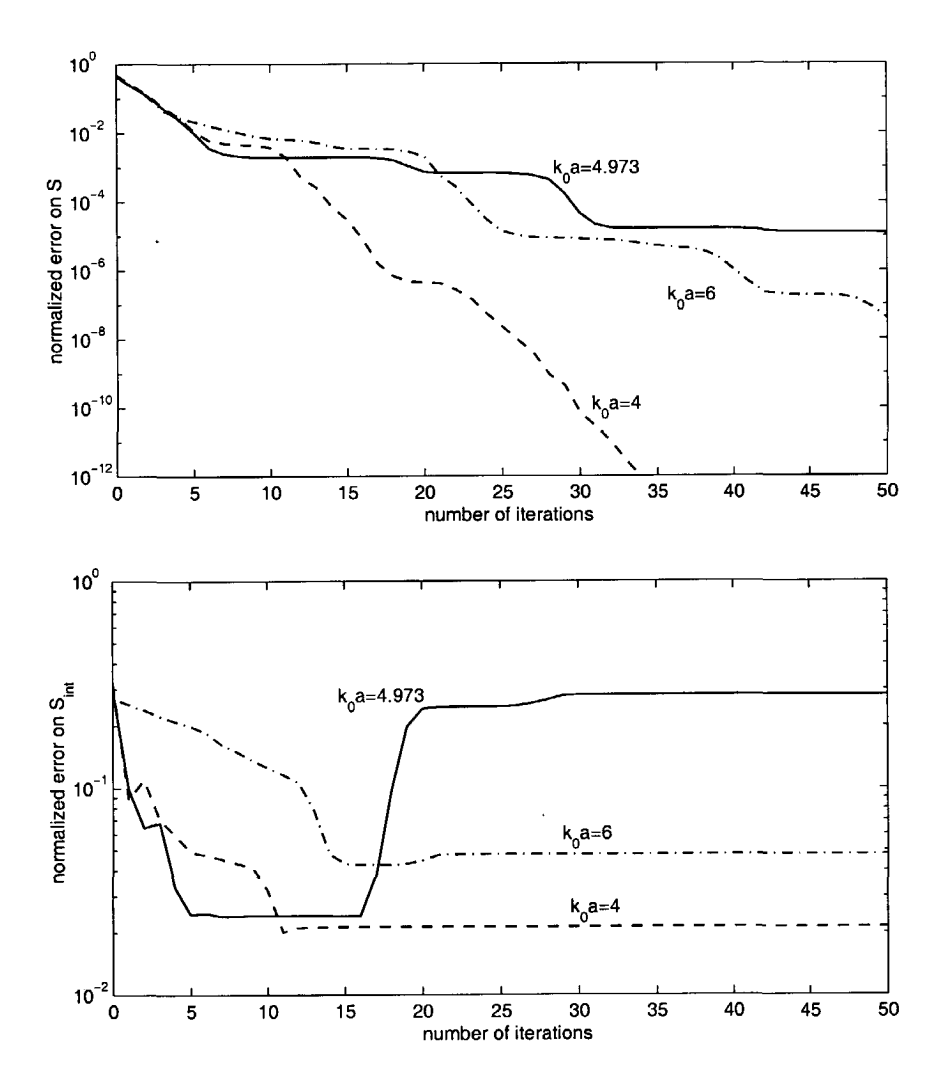


Figure 4.4: Normalized errors on S (top) and $S_{\rm int}$ (bottom) in conjugate gradient scheme.

field starts to deviate. From these results, we draw the conclusion that our additional error criterion seems to be a sufficient error norm to judge the final solution for the surface field $\boldsymbol{\nu} \times \boldsymbol{H}$ on S.

The present numerical results inspired us to use the interior norm on

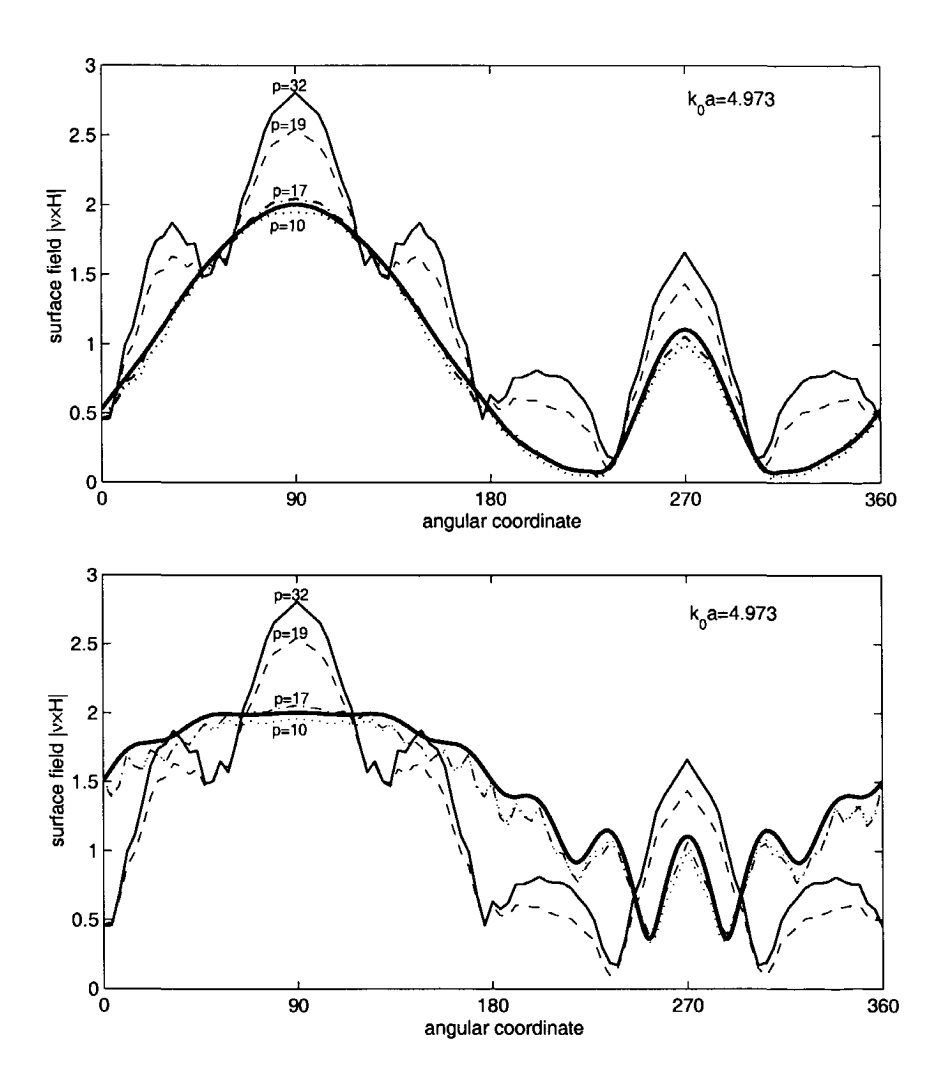


Figure 4.5: Tangential magnetic surface field for plane wave incidence with electric field vector in the x-direction (top) and y-direction (bottom), for increasing number, p, of iterations; the heavy solid line denotes the analytical results.

 S_{int} as a (sufficient) constraint for the magnetic-field integral equation, that eliminates the occurrence of spurious solutions due to interior resonances. Instead of a conjugate gradient scheme that minimizes the error norm on the surface S of the object, we propose to use a conjugate gradient scheme

that minimizes the sum of the two norms, viz.,

$$ERR = \left[ERR_S^2 + ERR_{S_{int}}^2\right]^{\frac{1}{2}}.$$
(4.42)

Later, we discuss that for the continuous (i.e. the non-discretized case) the conjugate gradient method, minimizing this sum of norms, provides a convergent iterative scheme that leads to the exact solution of our scattering problem.

4.5. Constrained conjugate gradient method

The conjugate gradient scheme that minimizes the combined error criterion of Eq. (4.42) is a modification of the previous one. To describe the modifications due to the presence of the error norm on $S_{\rm int}$, for the discretize quantities it is convenient to introduce an operator and an inner product on $S_{\rm int}$. We introduce a linear operator $\mathcal{L}_{\rm int}$ acting on a vector function $[\nu \times H]$ as

$$\mathcal{L}_{\text{int}}[\boldsymbol{\nu} \times \boldsymbol{H}] \equiv \left[\sum_{n=1}^{N} \sum_{i=1}^{3} \frac{A_n}{3} \nabla \mathcal{G}(\boldsymbol{x}_{n,i} - \boldsymbol{b}_m) \times [\boldsymbol{\nu} \times \boldsymbol{H}]_{n,i} \right],$$

$$m = 1, 2, \dots, N_{\text{int}}, \qquad (4.43)$$

and the vector function for a point $b_m \in S_{int}$,

$$\mathbf{H}^{\mathrm{i}} \equiv \mathbf{H}^{\mathrm{i}}(\mathbf{b}_{m}), \quad m = 1, 2, \dots, N_{\mathrm{int}}.$$
 (4.44)

Further, we define an inner product of two vector functions on $S_{\rm int}$ as

$$\langle \boldsymbol{f}, \boldsymbol{g} \rangle_{S_{\text{int}}} \equiv \sum_{m=1}^{N_{\text{int}}} A_m \boldsymbol{f}(\boldsymbol{b}_m) \cdot \overline{\boldsymbol{g}}(\boldsymbol{b}_m).$$
 (4.45)

The norm on S_{int} is defined as

$$\|\boldsymbol{f}\|_{S_{\text{int}}} = \left[\langle \boldsymbol{f}, \boldsymbol{f} \rangle_{S_{\text{int}}}\right]^{\frac{1}{2}}.$$
 (4.46)

We also need an adjoint operator $\mathcal{L}_{\mathrm{int}}^{\star}$ defined via the inner product as

$$\langle f, \mathcal{L}_{\text{int}}[\nu \times g] \rangle_{S_{\text{int}}} = \langle \mathcal{L}_{\text{int}}^{\star} f, [\nu \times g] \rangle_{S}.$$
 (4.47)

This adjoint operator mapping S_{int} into S is obtained as

$$\mathcal{L}_{\text{int}}^{\star} f \equiv -\nu_{m} \times \left\{ \nu_{m} \times \left[\sum_{n=1}^{N_{\text{int}}} A_{n} \nabla \overline{\mathcal{G}}(\boldsymbol{b}_{n} - \boldsymbol{x}_{m,j}) \times \boldsymbol{f}(\boldsymbol{b}_{n}) \right] \right\},$$

$$m = 1, 2, \dots, N, \quad j = 1, 2, 3. \tag{4.48}$$

With these extra definitions for the constraining error norm on S_{int} , we now formulate our conjugate gradient scheme that minimizes iteratively the combined error norm

$$ERR^{2} = \left(\frac{\|\boldsymbol{\rho}\|_{S}}{\|\boldsymbol{\nu} \times \boldsymbol{H}^{i}\|_{S}}\right)^{2} + \left(\frac{\|\boldsymbol{\rho}_{int}\|_{S_{int}}}{\|\boldsymbol{H}^{i}\|_{S_{int}}}\right)^{2}, \tag{4.49}$$

where the residual error on S and S_{int} are defined as

$$\rho = [\nu \times H^{i}] - \mathcal{L}[\nu \times H], \quad \rho_{int} = H^{i} - \mathcal{L}_{int}[\nu \times H]. \tag{4.50}$$

We start the conjugate gradient scheme with the physical-optics approximation, Eq. (4.23), as initial estimate, denoted by $[\nu \times H]^{(0)}$. Then, it computes

$$\boldsymbol{
ho}^{(0)} = [\boldsymbol{
u} \times \boldsymbol{H}^{\mathrm{i}}] - \boldsymbol{\mathcal{L}}[\boldsymbol{
u} \times \boldsymbol{H}]^{(0)}, \quad \boldsymbol{
ho}_{\mathrm{int}}^{(0)} = \boldsymbol{H}^{\mathrm{i}} - \boldsymbol{\mathcal{L}}_{\mathrm{int}}[\boldsymbol{
u} \times \boldsymbol{H}]^{(0)}.$$

Next the scheme chooses

$$oldsymbol{v}^{(1)} = oldsymbol{g}^{(1)} = rac{oldsymbol{\mathcal{L}}^{\star}oldsymbol{
ho}^{(0)}}{\|oldsymbol{
u} imesoldsymbol{H}^{ ext{i}}\|_S^2} + rac{oldsymbol{\mathcal{L}}_{ ext{int}}^{\star}oldsymbol{
ho}_{ ext{int}}^{(0)}}{\|oldsymbol{H}^{ ext{i}}\|_{S_{ ext{int}}}^2},$$

$$\alpha^{(1)} = \frac{\frac{\langle \boldsymbol{\rho}^{(0)}, \boldsymbol{\mathcal{L}} \boldsymbol{v}^{(1)} \rangle_{S}}{\|\boldsymbol{\nu} \times \boldsymbol{H}^{\mathrm{i}}\|_{S}^{2}} + \frac{\langle \boldsymbol{\rho}_{\mathrm{int}}^{(0)}, \boldsymbol{\mathcal{L}}_{\mathrm{int}} \boldsymbol{v}^{(1)} \rangle_{S_{\mathrm{int}}}}{\|\boldsymbol{H}^{\mathrm{i}}\|_{S_{\mathrm{int}}}^{2}}}{\frac{\|\boldsymbol{\mathcal{L}} \boldsymbol{v}^{(1)}\|_{S}^{2}}{\|\boldsymbol{\nu} \times \boldsymbol{H}^{\mathrm{i}}\|_{S}^{2}} + \frac{\|\boldsymbol{\mathcal{L}}_{\mathrm{int}} \boldsymbol{v}^{(1)}\|_{S_{\mathrm{int}}}^{2}}{\|\boldsymbol{H}^{\mathrm{i}}\|_{S_{\mathrm{int}}}^{2}}},$$

with the updates

$$[oldsymbol{
u} imes oldsymbol{H}]^{(1)} = [oldsymbol{
u} imes oldsymbol{H}]^{(0)} + lpha^{(1)} oldsymbol{v}^{(1)} \,,$$
 $oldsymbol{
ho}^{(1)} = oldsymbol{
ho}^{(0)} - lpha^{(1)} oldsymbol{\mathcal{L}}_{\mathrm{int}} oldsymbol{v}^{(1)} \,,$ $oldsymbol{
ho}^{(1)}_{\mathrm{int}} = oldsymbol{
ho}^{(0)}_{\mathrm{int}} - lpha^{(1)} oldsymbol{\mathcal{L}}_{\mathrm{int}} oldsymbol{v}^{(1)} \,,$

and computes successively for $p = 2, 3, \ldots, P$,

$$m{g}^{(p)} = rac{m{\mathcal{L}}^{\star}m{
ho}^{(p-1)}}{\|m{
u} imesm{H}^{
m i}\|_S^2} + rac{m{\mathcal{L}}_{
m int}^{\star}m{
ho}_{
m int}^{(p-1)}}{\|m{H}^{
m i}\|_{S_{
m int}}^2}\,, \quad m{v}^{(p)} = m{g}^{(p)} + rac{\|m{g}^{(p)}\|_S^2}{\|m{g}^{(p-1)}\|_S^2}\,m{v}^{(p-1)}\,,$$

$$\alpha^{(p)} = \frac{\frac{\langle \boldsymbol{\rho}^{(p-1)}, \boldsymbol{\mathcal{L}}\boldsymbol{v}^{(p)}\rangle_{S}}{\|\boldsymbol{\nu}\times\boldsymbol{H}^{\mathrm{i}}\|_{S}^{2}} + \frac{\langle \boldsymbol{\rho}_{\mathrm{int}}^{(p-1)}, \boldsymbol{\mathcal{L}}_{\mathrm{int}}\boldsymbol{v}^{(p)}\rangle_{S_{\mathrm{int}}}}{\|\boldsymbol{H}^{\mathrm{i}}\|_{S_{\mathrm{int}}}^{2}}}{\frac{\|\boldsymbol{\mathcal{L}}\boldsymbol{v}^{(p)}\|_{S}^{2}}{\|\boldsymbol{\nu}\times\boldsymbol{H}^{\mathrm{i}}\|_{S}^{2}} + \frac{\|\boldsymbol{\mathcal{L}}_{\mathrm{int}}\boldsymbol{v}^{(p)}\|_{S_{\mathrm{int}}}^{2}}{\|\boldsymbol{H}^{\mathrm{i}}\|_{S_{\mathrm{int}}}^{2}}},$$

with the updates

$$[\boldsymbol{\nu} \times \boldsymbol{H}]^{(p)} = [\boldsymbol{\nu} \times \boldsymbol{H}]^{(p-1)} + \alpha^{(p)} \boldsymbol{v}^{(p)},$$

$$\boldsymbol{\rho}^{(p)} = \boldsymbol{\rho}^{(p-1)} - \boldsymbol{\alpha}^{(p)} \boldsymbol{\mathcal{L}} \boldsymbol{v}^{(p)} \,, \quad \boldsymbol{\rho}_{\mathrm{int}}^{(p)} = \boldsymbol{\rho}_{\mathrm{int}}^{(p-1)} - \boldsymbol{\alpha}^{(p)} \boldsymbol{\mathcal{L}}_{\mathrm{int}} \boldsymbol{v}^{(p)} \,.$$

In fact, this constrained conjugate gradient scheme solves iteratively the symmetrized integral equation

$$\left(\frac{\mathcal{L}^{\star}\mathcal{L}}{\|\boldsymbol{\nu}\times\boldsymbol{H}^{i}\|_{S}^{2}} + \frac{\mathcal{L}_{\text{int}}^{\star}\mathcal{L}_{\text{int}}}{\|\boldsymbol{H}^{i}\|_{S_{\text{int}}}^{2}}\right)[\boldsymbol{\nu}\times\boldsymbol{H}]$$

$$= \left(\frac{\mathcal{L}^{\star}[\boldsymbol{\nu}\times\boldsymbol{H}^{i}]}{\|\boldsymbol{\nu}\times\boldsymbol{H}^{i}\|_{S}^{2}} + \frac{\mathcal{L}_{\text{int}}^{\star}\boldsymbol{H}^{i}}{\|\boldsymbol{H}^{i}\|_{S_{\text{int}}}^{2}}\right), \text{ on } S. \tag{4.51}$$

For the non-discretized problem, this integral equation is uniquely solvable, since the symmetrized operator $\mathcal{L}^{\star}\mathcal{L}$ is non-negative and the symmetrized operator $\mathcal{L}^{int}_{int}\mathcal{L}_{int}$ is positive, because the latter operator does not have a null-space. Hence, the complete operator is positive and the conjugate gradient scheme (for the non-discretized problem) converges to the exact solution [28, 29], even for frequencies coinciding with an eigenfrequency of interior resonance.

In view of the definition of the two error norms of Eq. (4.42), the extra computation time per iteration to take the second error norm into account is roughly of the order $\frac{1}{3}N_{\rm int}/N$, so that the objective is to minimize $N_{\rm int}$ as much as possible.

4.5.1. Numerical example of a sphere

As an example, we again consider the problem of scattering of a plane wave by a sphere, where analytical results in terms of the Mie series are available. The precise shape of the interior surface is not essential, in fact the only important requirement is that the discretized version of the interior object prescribes a closed interior surface within numerical accuracy. In order to guarantee that in the discretized counterpart of $S_{\rm int}$ the field variation is computable within the present computer accuracy, we use the same arguments as before and we take care that $S_{\rm int}$ encloses a sphere with a diameter of a half wavelength, and on $S_{\rm int}$ we take a discretization of five to six points per wavelength. Taking a larger interior surface and/or a finer discretization is always allowed, but it will increase the computation time without any benefit.

We start with the same discretization as before and discretize the boundary S of the sphere in 960 patches and the interior surface $S_{\rm int}$ in 110 patches (see Figs. 4.2 and 4.3). For the present case, our constrained conjugate gradient method needs only 3% more computer time than the unconstrained one.

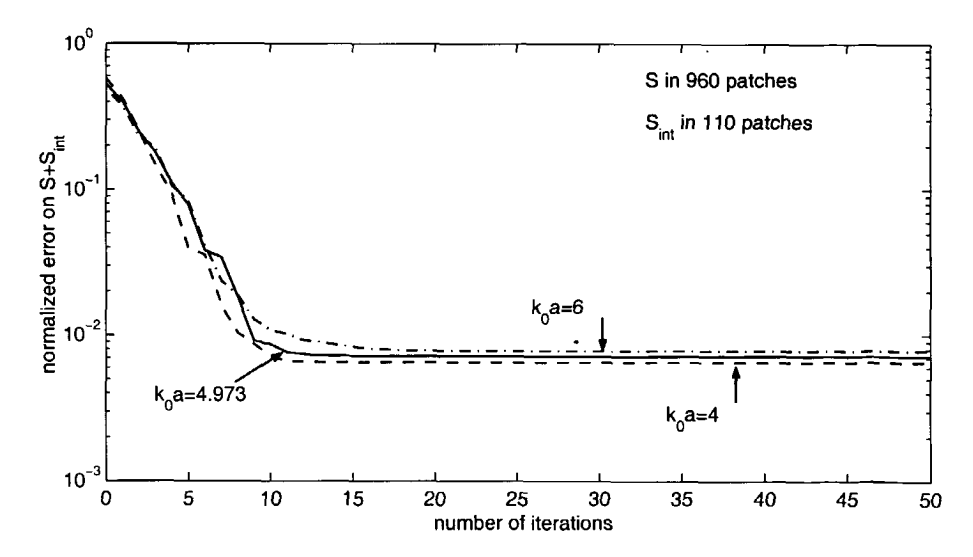


Figure 4.6: Normalized error on $S + S_{\text{int}}$ in the constrained conjugate gradient iterative scheme.

	S in 110 patches	S in 960 patches	S in 9800 patches
$S_{ m int}$ in 110 patches	ERR = 0.0457	ERR = 0.0072	ERR = 0.0006
$S_{ m int}$ in 960 patches	ERR = 0.0464	ERR = 0.0072	ERR = 0.0006
$S_{ m int}$ in 9800 patches	ERR = 0.0465	ERR = 0.0072	ERR = 0.0006

Table 4.1: Final normalized error on $S + S_{int}$ for different discretizations ($k_0 a = 4.973$)

We again consider the three frequencies corresponding to $k_0a = 4$, 4.973 and 6, respectively.

In Fig. 4.6, we present the normalized error, see Eq. (4.42) as a function of the number of iterations, using the constrained conjugate gradient scheme. We observe that, for $k_0a=4.973$, where the unconstrained conjugate gradient methods yields a spurious solution due to an interior resonance, the error minimized by the constrained conjugate gradient method decreases monotonically to some constant value. It is further observed that the final error (after 50 iterations) increases with increasing k_0a and this fact gives the impression that this final error is a measure for the quality of the computed surface field. We therefore investigate the discretization errors in more detail, by taking different discretizations of the boundary surface S of the scattering object and the interior surface $S_{\rm int}$.

In Table 4.1, the normalized combined error ERR is presented for the various discretizations. We observe that the discretization of the interior surface in 110 patches is sufficient. This is roughly a discretization of five to six points per wavelength. In order to be sure to eliminate spurious solutions due to interior resonances, a smaller discretization of this interior surface is not allowed. Using a discretization of the interior surface in 110 patches, we further observe that the error decreases from 0.0457 to 0.0006 when we refine the discretization of the boundary surface S from 110 patches to 9800 patches, which is roughly a discretization of 2 points per wavelength to 20

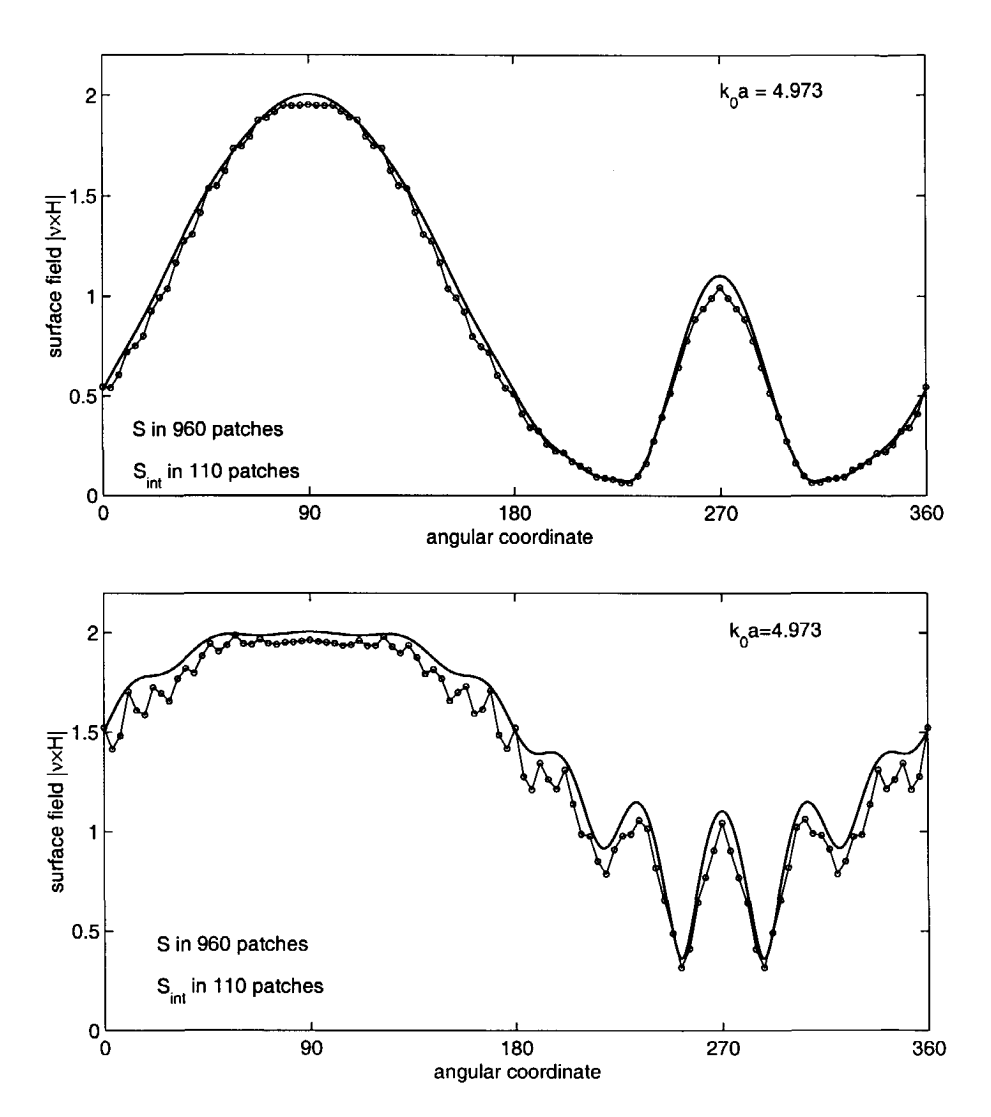


Figure 4.7: Tangential magnetic surface field for plane wave incidence with electric field vector in the x-direction (top) and y-direction (bottom); solid line: analytical results; circles: numerical results based on minimization of combined error criterion.

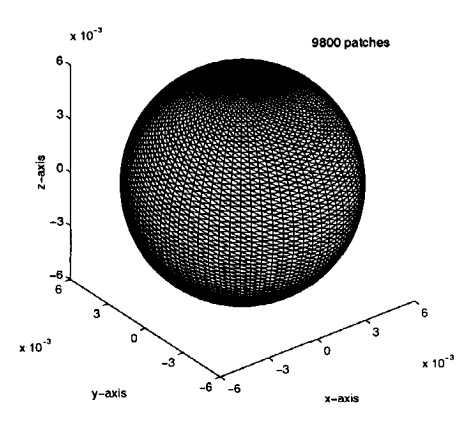
points per wavelength, respectively. This confirms our expectation that the normalized error over both S and $S_{\rm int}$ is a sufficient error criterion, not only theoretically, but also in computational sense.

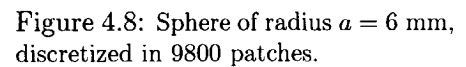
In Fig. 4.7, we present the absolute value of the surface field $\nu \times H$ as a function of the angular coordinate along the surface of the sphere in the cross-sectional plane x=0, for an incident plane wave with electric field vector in the x-direction (top figure) and y-direction (bottom figure), respectively. The circles denote our computed solution based on minimization of the combined error criterion, while the solid lines denote the computed results using the analytic expression of the surface field in terms of the Mie series.

Before discussing objects of more complicated shapes, we consider the spherical object with a finer discretization and subsequently for an increased frequency.

Finer discretization

Subsequently, we study the effect of a finer discretization of the boundary surface S. We take a discretization of 9800 patches instead of 960 patches, while keeping the discretization of the interior surface in 110 patches (see Figs. 4.8 and 4.9). In Fig. 4.10, we present the results for the absolute value of the surface field $\nu \times H$. We observe excellent agreement with the analytical solution based on the Mie series. We certainly may conclude that the presence of a spurious field due to interior resonances at the frequency belonging to $k_0a = 4.973$ has been eliminated by the method of minimizing





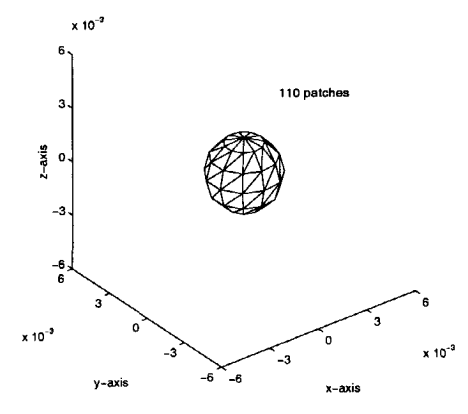


Figure 4.9: Interior sphere of radius $\frac{1}{3}a$, discretized in 110 patches.

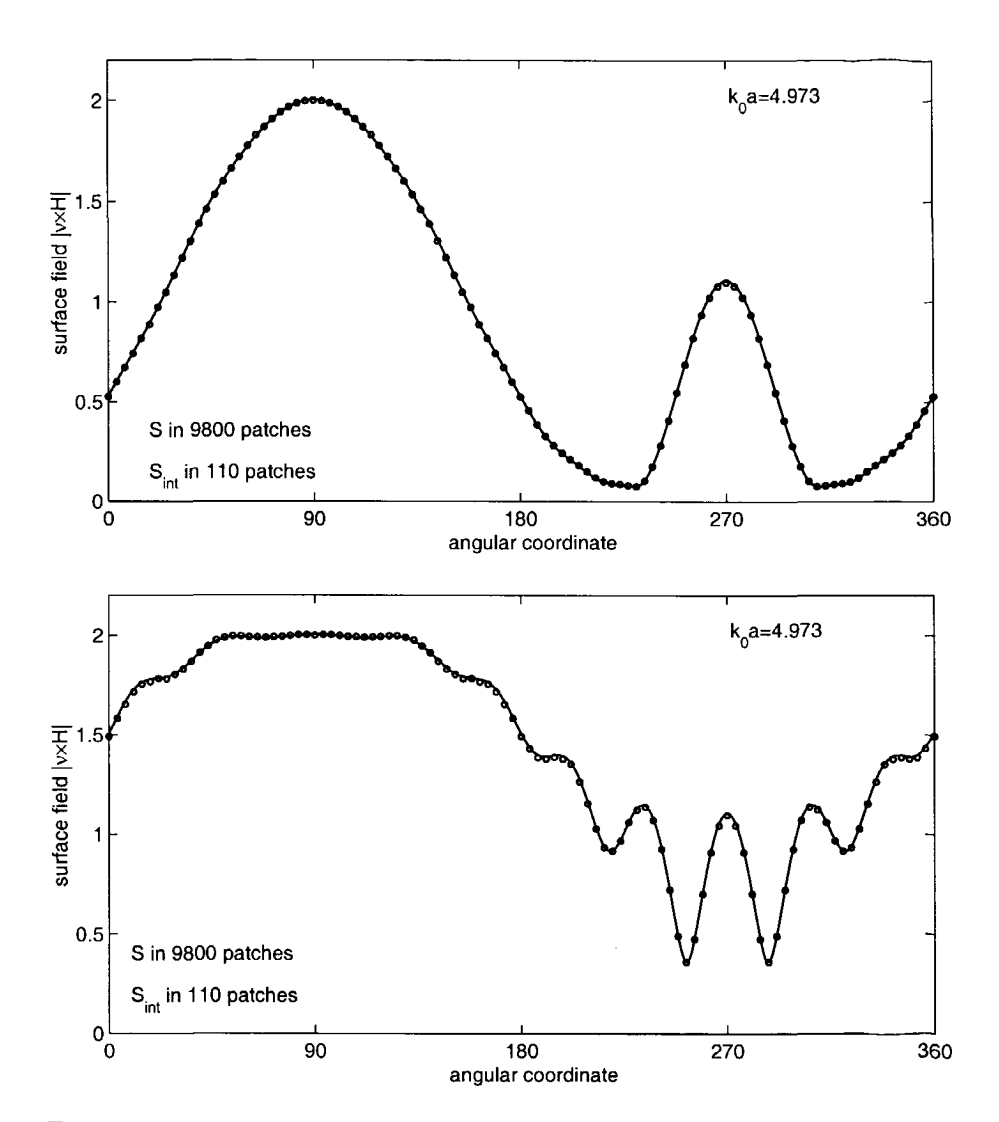


Figure 4.10: Tangential magnetic surface field for plane wave incidence with electric field vector in the x-direction (top) and y-direction (bottom); solid line: analytical results, circles: numerical results based on minimization of combined error criterion.

the combined error criterion, combining the error on the boundary S and the interior surface $S_{\rm int}.$

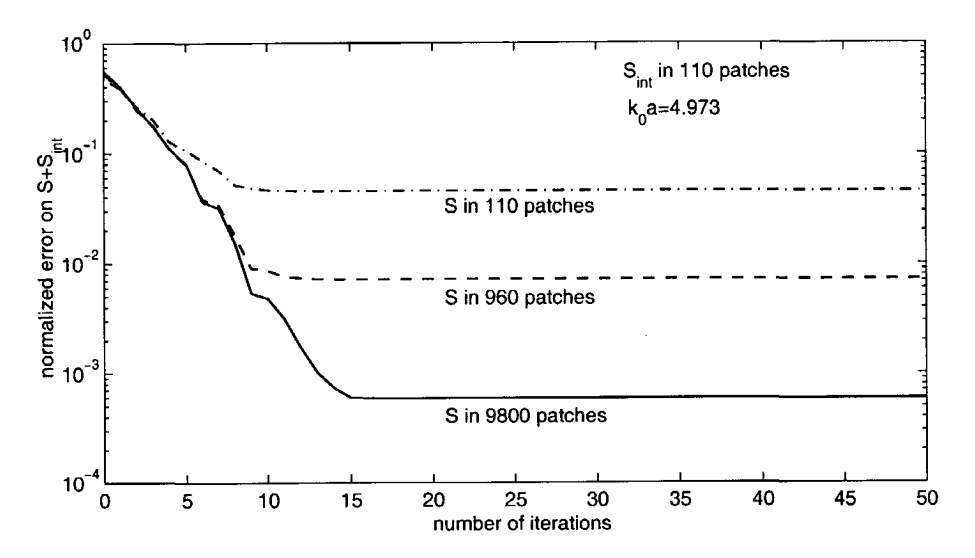


Figure 4.11: Normalized error on $S + S_{int}$ in the constrained conjugate gradient iterative scheme.

In Fig. 4.11, we present the error as a function of the number of iterations. For comparison we plot the errors for a rough discretization as well. It seems that the combined error is a measure for the error in the discretization of the boundary surface of the object; refining the discretization with a factor of ten yields a reduction of an order in the final error ERR. Note further that the error (see Fig. 4.11) converges very fast (within 20 iterations) to the final error value. In view of the fast convergence, our new, constrained, conjugate gradient scheme offers the possibility to compute the scattered field from objects which are large compared to the wavelength.

Increased frequency

We now increase the frequency and consider a normalized wavenumber of $k_0a = 15$. We take a discretization of 9800 patches on the boundary surface S and 960 points on the interior surface S_{int} , see Figs. 4.12 and 4.13. This means that on both surfaces we have discretizations of roughly 6 points per wavelength.

In Fig. 4.14, we present the error as function of the number of iterations for $k_0a = 15$. For comparison, we present the results for a discretization of the interior surface in 110 patches as well (dotted line). For further compar-

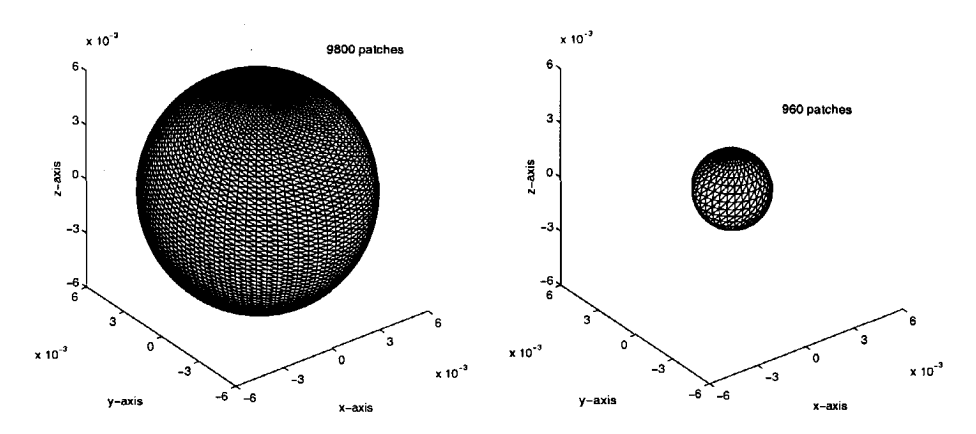


Figure 4.12: Sphere of radius a=6 mm, discretized in 9800 patches.

Figure 4.13: Interior sphere of radius $\frac{1}{3}a$, discretized in 960 patches.

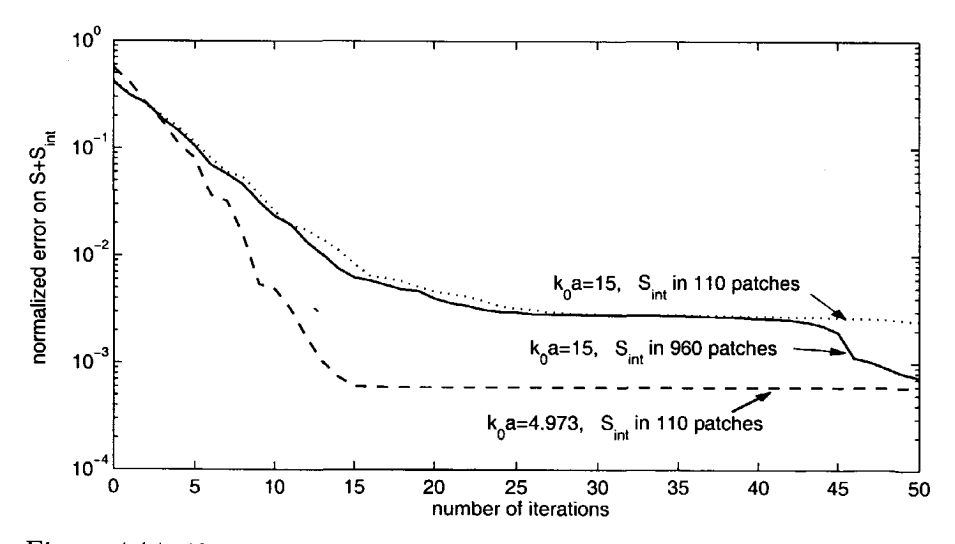


Figure 4.14: Normalized error on $S+S_{\rm int}$ in the constrained conjugate gradient iterative scheme.

ison, we have copied the results for ka=4.973 from Fig. 4.11 and plotted as dashed line. Although, for both cases, the boundary surface of the object is discretized in the same number of points, it seems that the discretization

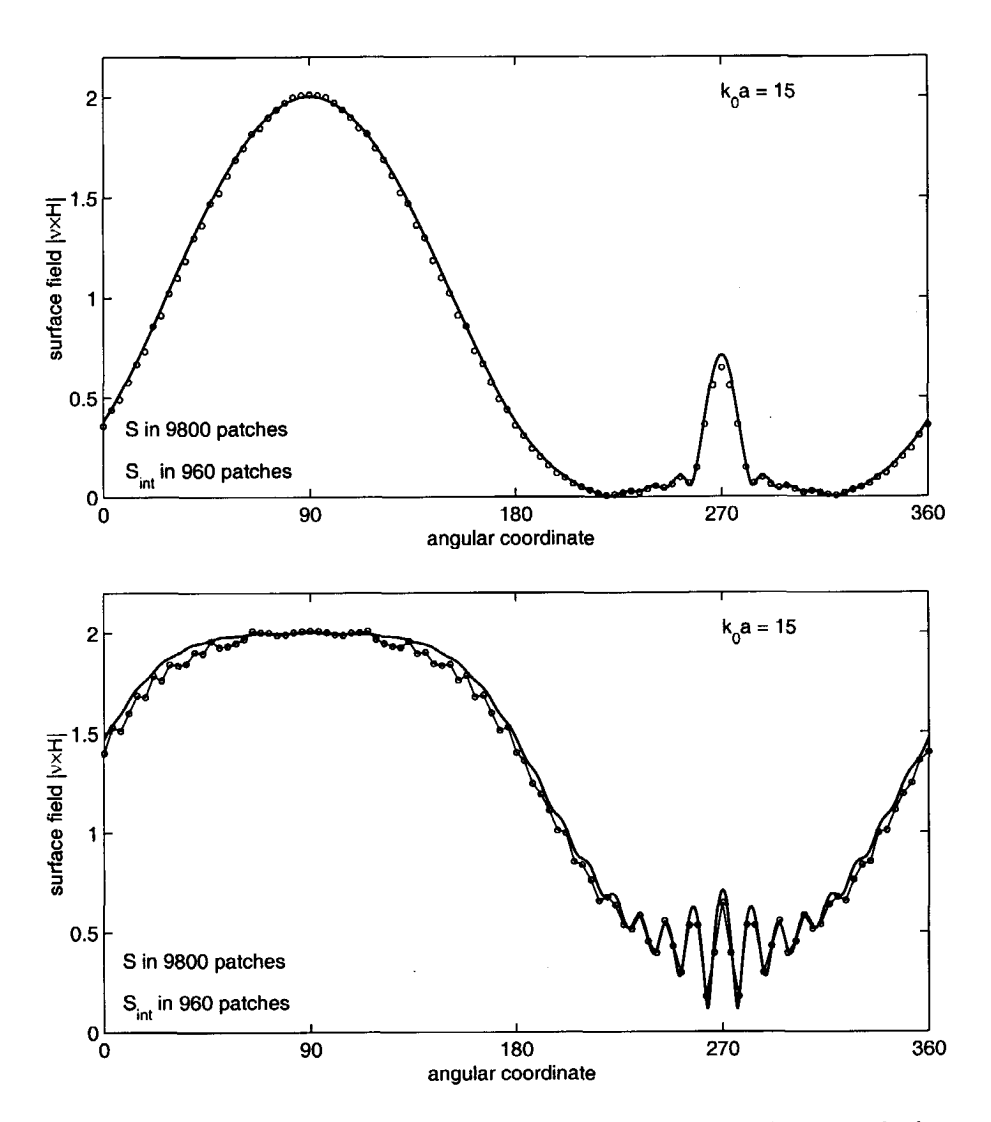


Figure 4.15: Tangential magnetic surface field for plane wave incidence with electric field vector in the x-direction (top) and y-direction (bottom); solid line: analytical results, circles: numerical results based on minimization of combined error criterion.

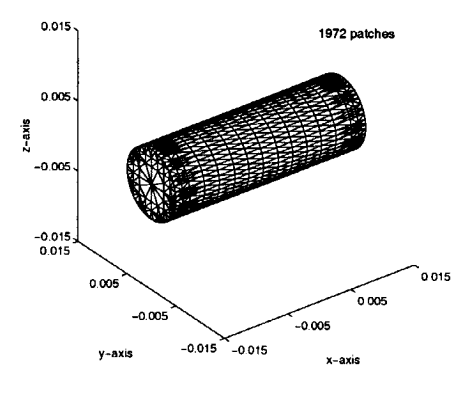
errors, made for higher values of ka, becomes relatively smaller. In addition a finer discretization of the interior surface helps to decrease the error after

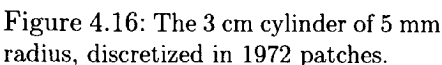
a large number of iterations. This fact is not observed for lower frequencies (see Table 4.1). In Fig. 4.15 we present, for $k_0a = 15$, the absolute values of the surface field $\nu \times H$.

So far we have carried out a number of numerical experiments for the spherical scattering object to illustrate the performance of the constrained conjugate gradient method. However, one can argue that the sphere is a too simple shape to validate the proposition and actual implementation of the combined error norm. We therefore carry out more experiments with scattering objects, we are using in our experiments of Chapter 5.

4.5.2. Numerical results of a finite cylinder

One of the targets we consider in our experiments of the next chapter is the finite cylinder with circular cross-section. Here, we again assume that the incident field is a plane wave incident in the negative z-direction. We further assume that the incident electric field vector is oriented in the y-direction. The cylinder has a radius of 5 mm and a length of 3 cm. The frequency of operation is 35.06 GHz and the wavelength is 0.856 cm. We discretize the boundary surface into 1972 patches (Fig. 4.16), which is a discretization of five to six points per wavelength. The interior surface is the same as before, viz., a sphere with a radius of 2 mm, and discretized into





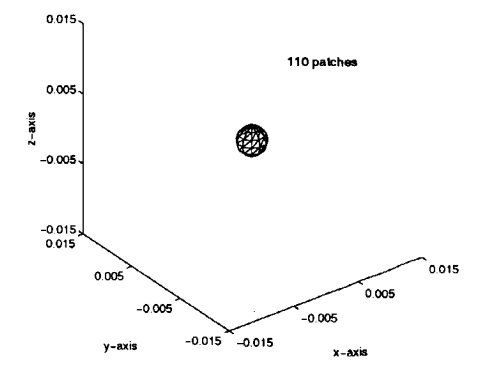


Figure 4.17: Interior sphere of 2 mm radius, discretized in 110 patches.

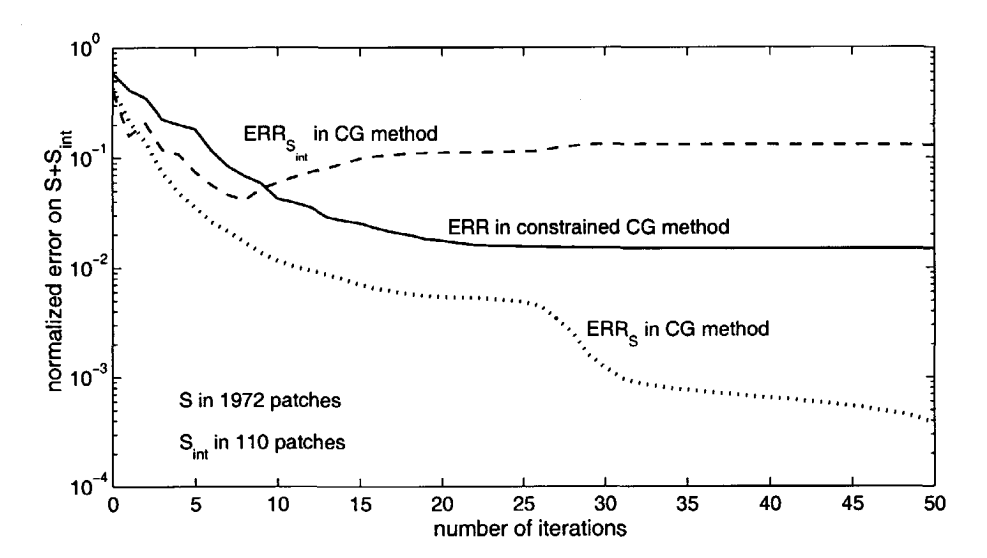


Figure 4.18: Normalized error on $S + S_{int}$ in the constrained conjugate gradient iterative scheme.

110 patches (Fig. 4.17).

We compute the surface field $\nu \times H$ with the conjugate gradient method that minimizes the error ERR_S in the magnetic-field integral equation. In Fig. 4.18, the normalized error, ERR_S, as a function of the number of iterations is presented as the dotted line. Simultaneously, we check the interior error by presenting the normalized error, ERR_{Sint}, as the dashed lines. We observe that after 10 iterations the interior error increases, while the boundary error decreases rapidly. From our experience of the previous example we know that this is an indication that we compute a spurious solution due to an interior resonances. When we compute the surface field with our constrained conjugate gradient method that minimizes the combined error, ERR, we observe that the latter scheme converges to a minimum that is a measure for the discretization error (see solid line in Fig. 4.18).

4.5.3. Numerical results of a plate

So far we have considered rotationally symmetric targets. Since our computational method can handle arbitrarily closed objects, we now consider a

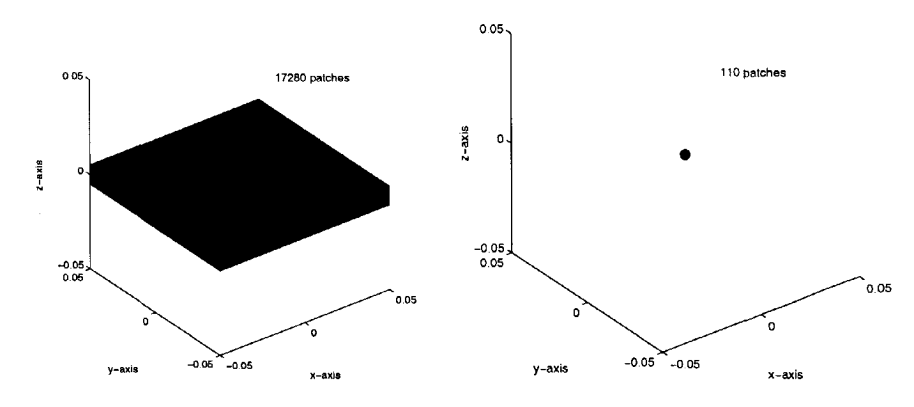


Figure 4.19: Plate of $10 \times 10 \times 1 \text{ cm}^3$, discretized in 17280 patches.

Figure 4.20: Interior sphere of 2 mm radius, discretized in 110 patches.

square plate of dimensions 10 cm by 10 cm and thickness of 1 cm (Fig. 4.19). The incident field is a plane wave incident in the negative z-direction, with polarization of the electric field in the y-direction. The frequency of operation is 35.06 GHz and the wavelength is 0.856 cm. We discretize the boundary surface into 17280 patches, which is a discretization of roughly five points per wavelength. The interior surface $S_{\rm int}$ is the same as before, viz., a sphere of radius 2 mm, and discretized into 110 patches. We locate this sphere in the center of the plate domain (Fig. 4.20).

We first compute the surface field $\nu \times H$ with the conjugate gradient method that minimizes the error ERR_S in the magnetic-field integral equation. In Fig. 4.21, the normalized error, ERR_S, as a function of the number of iterations is presented as the dotted line. Simultaneously, we check the interior error by presenting the normalized error, ERR_{Sint}, as the dashed lines. We observe that already after five iterations the interior error increases, while the boundary error remains decreasing. In view of the increasing error on the interior surface, we note that we again deal with an interior resonance and that we compute a spurious solution. However, when compute the surface field with our constrained conjugate gradient method that minimizes the combined error, ERR, we observe again that the latter scheme converges to a minimum that is a measure for the discretization error (see solid line in Fig. 4.21). Although we have many $(2 \times 3 \times 17280)$ unknowns, still the

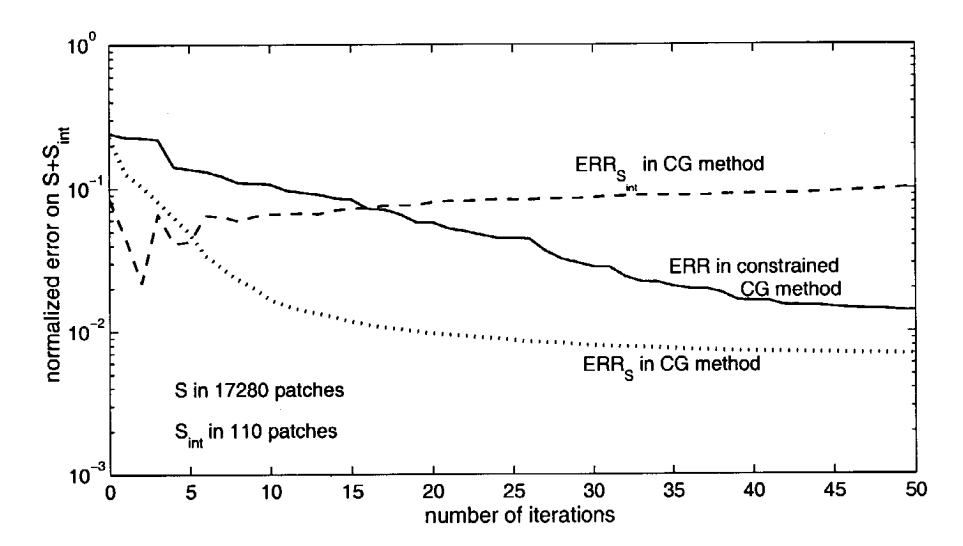


Figure 4.21: Normalized error on $S + S_{int}$ in the constrained conjugate gradient iterative scheme.

constrained conjugate gradient method reaches its minimum in roughly 50 iterations.

So far we have located the interior sphere in the center of the targets. In order to show that the location is not important, as long as the interior surface is not too close the boundary surface of the object (to stay away from the singular point of the Green function), we locate the interior sphere near a corner of the plate (see Figs. 4.22 and 4.23). We take the center of the interior sphere at $\{-0.04, 0.04, 0\}$ m. The various error quantities are presented in Fig. 4.24. Comparing these results with the ones of Fig. 4.21 we observe that the interior error starts in the first few iterations at a much larger value and for further iterations it remains at that value, while the combined error (ERR) of the constrained conjugate gradient method starts at a much higher level, but converges rapidly to the same error value as obtained for the case of the centered interior sphere. Obviously, by moving the interior sphere to the corner of the plate, we visualize that the local errors, certainly in the first iterations, are larger at the corner than in the middle of the plate; the internal error criterion indicates this phenomenon.

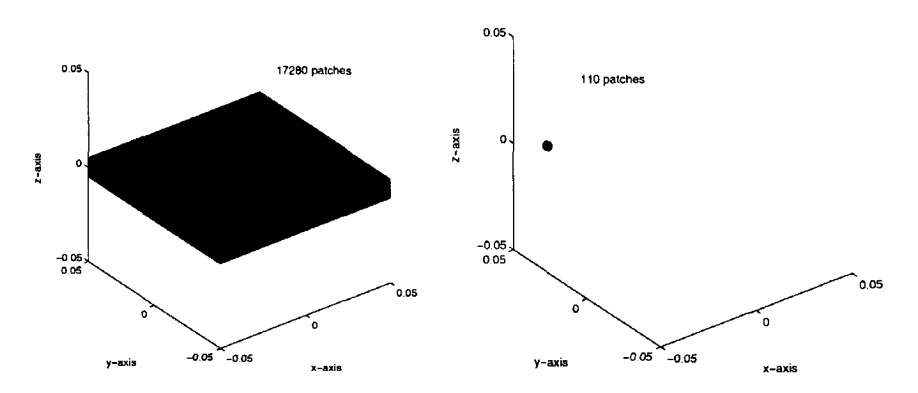


Figure 4.22: Plate of $10 \times 10 \times 1 \text{ cm}^3$, discretized in 17280 patches.

Figure 4.23: Interior sphere of 2 mm radius, discretized in 110 patches.

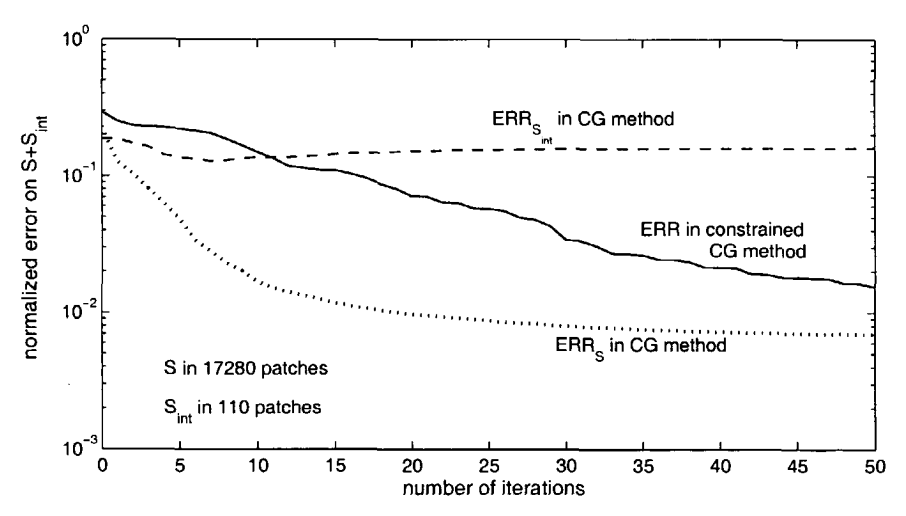


Figure 4.24: Normalized error on $S + S_{\rm int}$ in the constrained conjugate gradient iterative scheme.

4.5.4. Numerical results of a capped box

We finally consider a more complicated object. We take a box capped with three cones. The incident field is a plane wave incident in the negative z-direction, while the electric field vector is oriented in the y-direction. The

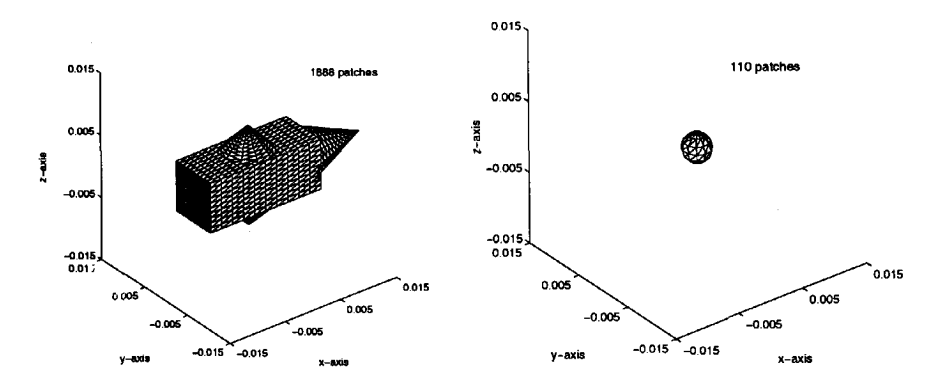


Figure 4.25: The capped box discretized in 1888 patches.

Figure 4.26: Interior sphere of 2 mm radius, discretized in 110 patches.

box has a length of 3 cm and a cross-section of 0.8×0.8 cm². At the end, the box is capped with a right circular cone; this cone has a height of 1 cm and a basis cross-section with a radius of 0.4 cm. In addition on two opposite sides we have placed cones with a height of 0.4 cm and a basis cross-section with a radius of 0.4 cm. The frequency of operation is 35.06 GHz and the wavelength is 0.856 cm. We discretize the boundary surface into 1888 patches (Fig. 4.25), which is a discretization of five to six points per wavelength. The interior surface is the same as before, viz., a sphere with a radius of 2 mm, and discretized into 110 patches (Fig. 4.26).

We compute the surface field $\nu \times H$ with the conjugate gradient method that minimizes the error ERR_S in the magnetic-field integral equation. In Fig. 4.27, the normalized error, ERR_S, as a function of the number of iterations is presented as the dotted line. Simultaneously, we check the interior error by presenting the normalized error, ERR_{Sint}, as the dashed lines. We see that the initial estimate of the physical-optics approximation yields a normalized error larger than 100 % and this indicates that the physical-optics approximation without further improvement cannot be used for these types of targets. We further observe that the interior error ERR_{Sint} after 10 iterations does not decrease anymore and remains at a high error level of about 20 %, while the boundary error ERR_S decreases rapidly. When we compute the surface field with our constrained conjugate gradient method that minimizes the combined error, ERR, we observe that the latter scheme converges to a minimum that is a measure for the discretization error (see solid line

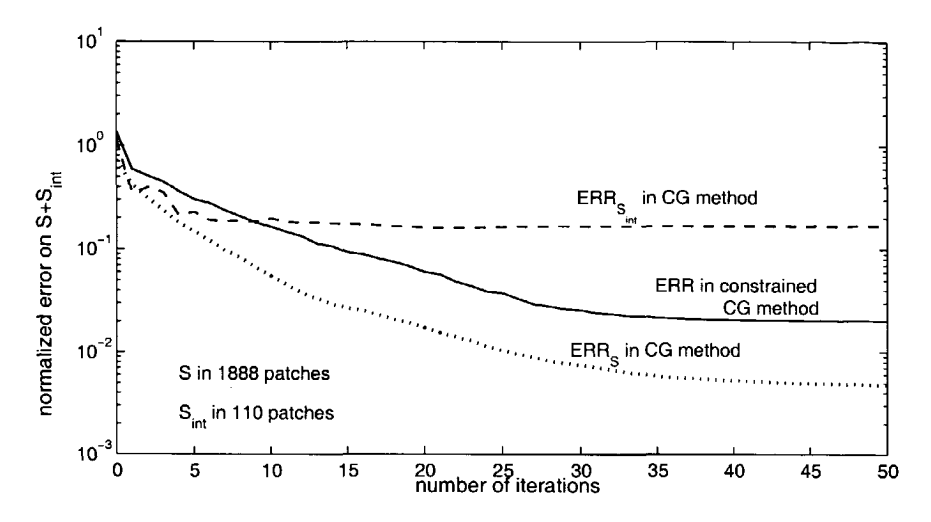


Figure 4.27: Normalized error on $S + S_{\text{int}}$ in the constrained conjugate gradient iterative scheme.

in Fig. 4.27). The conclusions is that for complex objects, where the behavior and occurrence of interior resonances are completely unpredictable, the method dealing with the magnetic-field integral equation only is unreliable and has to be used in combination with our interior error constraint.

With this example we conclude our numerical approach. In the next chapter we compare our numerical results for the scattered field with measurements, when the transmitting/receiving antenna is moved towards the target.



Chapter 5

Comparison of Experimental and Numerical Results

In this Chapter, we compare our numerically computed results and the measured results for various objects. We use a measurement setup, where the antenna is moved to the object under consideration. We assume that the speed of movement is much smaller than the wave speed in vacuum, so that no relativistic corrections are needed. This means that for each location of the transmitting/receiving antenna the scattering problem can be handled as a stationary one. The measurements are performed in an anechoic chamber and the experimental setup is the same as described in Chapter 2. In the experimental setup, the received signals are processed by a microwave mixer, such that the output voltage is proportional to the real part of the complex value of the measured electric field component [1]. Therefore we have multiplied our computed results with the calibration constant calculated in Chapter 2. In addition, we use the correction of the positioning of the antenna configuration determined in Chapter 2. The measurements are performed at 35.06 GHz.

5.1. Experiments with a sphere

We first present the results for a sphere made of aluminum. In our numerical modeling we assume that it is equivalent to a perfectly conducting scattering object. The radius, a, of the sphere is 6 mm, so that we deal with the

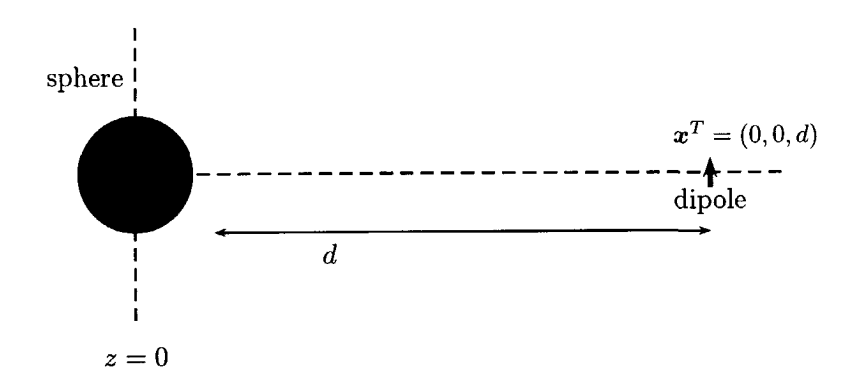


Figure 5.1: Dipole antenna moving towards the sphere.

normalized wave number $k_0a = 4.4$. The sphere is suspended from the sledge of the upper rail, while the dipole antenna which is located at the lower sledge is moved towards the sphere. The center of the sphere coincides with the origin of the coordinate system. In our computations, the position of the transmitting and receiving dipole is given by $x^T = \{0, 0, d + \Delta d\},\$ where the value of Δd =0.58 mm is found from the shift correction explained in Chapter 2. The dipole antenna is moved along the z-axis towards the sphere, see Fig. 5.1. The parameter d is the varying distance between the dipole antenna and the scattering surface. The dipole is oriented in the ydirection with a dipole moment $I_{ant}L = \{0, C, 0\}$, where the amplitude C of the dipole moment is found from the calibration procedure explained in Chapter 2. Since only the y-component of the scattered field is measured, we suffice by computing the y-component of the scattered field and the real part of this field component represents the reflected field amplitude E^r measured by the antenna system. When the antenna is moved towards the sphere, the scattered electromagnetic fields are measured at certain discrete points along the range of 19.7 mm $< d_k < 169.7$ mm with a sampling unit of 0.04 mm. From the measured response we subtract its DC value. We calculated this DC value by taking the mean value of all the measurements.

In our computations we discretize the boundary surface S of the sphere in 960 plane triangular patches and the internal spherical surface $S_{\rm int}$ in 110 patches, which is sufficient to obtain the accuracy within not too much computation time (see Chapter 4).

Constrained conjugate gradient method (CG)

We first compute the surface field $\nu \times H$ with the constrained conjugate gradient method (CG) as developed in Chapter 4. We stop the iteration once an error less than 2 % is arrived at. The maximum number of iterations to meet this error criterion is denoted as P. Since we compute the scattered fields at certain discrete points, $k = 1, 2, \dots, 300$, along the measurement range, the field changes roughly with the factor

$$C_{k,k-1} = \exp\left[\mathrm{i}k_0|\boldsymbol{x}_k^T - \boldsymbol{x}_{k-1}^T|\right] \frac{|\boldsymbol{x}_k^T|}{|\boldsymbol{x}_k^T|}, \quad \boldsymbol{x}_k^T = \{0, 0, d_k + \Delta d\},$$
 (5.1)

and we use this factor to improve the initial estimate, when we change the antenna position from d_{k-1} to d_k . Our computational procedure is as follows. We start for k=1 with the physical-optics approximation, using Eq. (4.23), as an initial estimate and let the constrained conjugate gradient method iterate P times until it satisfies the error criterion of 2 %. For each new position of the dipole antenna we use the following initial estimate,

$$[\nu \times H]^{(0,k)} = C_{k,k-1}[\nu \times H]^{(P,k-1)},$$
 (5.2)

where $[\boldsymbol{\nu} \times \boldsymbol{H}]^{(P,k-1)}$ denotes the updated surface field in the last iteration of the previous location of the antenna, while $[\boldsymbol{\nu} \times \boldsymbol{H}]^{(0,k)}$ denotes the initial

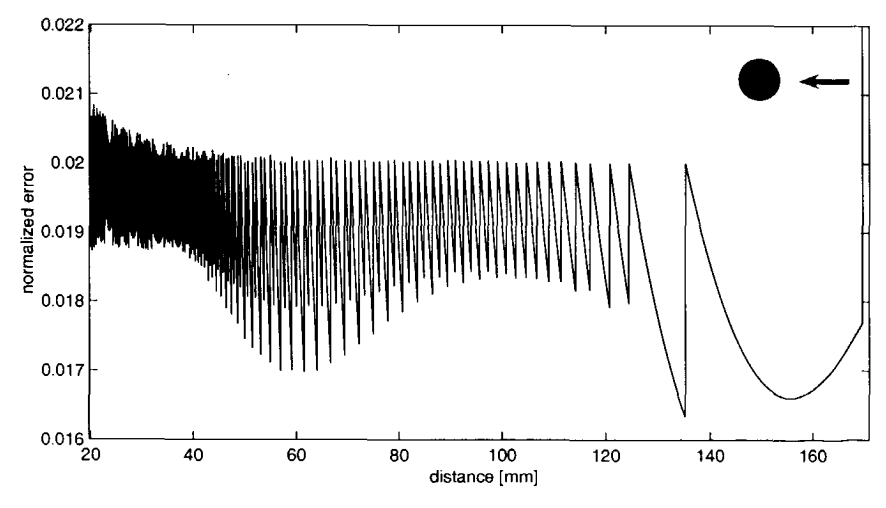


Figure 5.2: The error, ERR, as a function d_k in the simulation procedure.

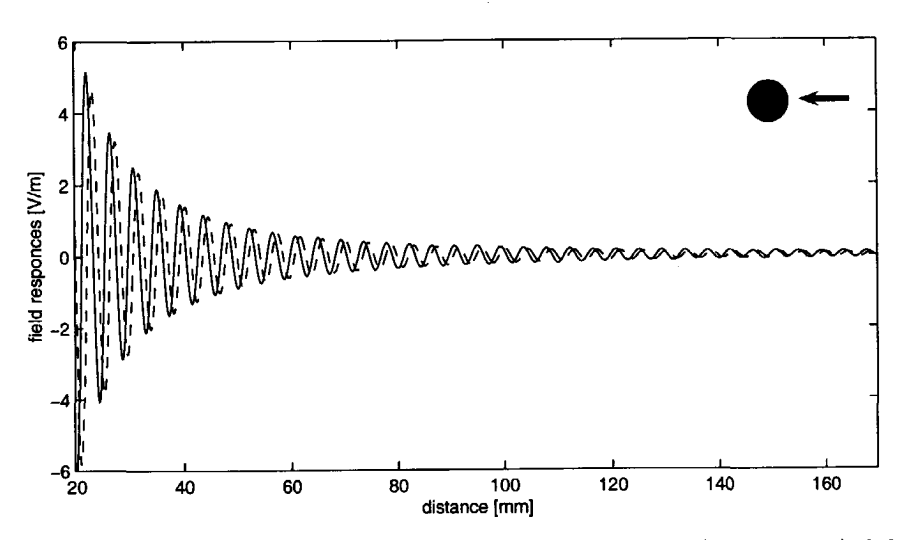


Figure 5.3: The measured (solid line) and simulated CG (dashed line) field responses as a function of distance d_k .

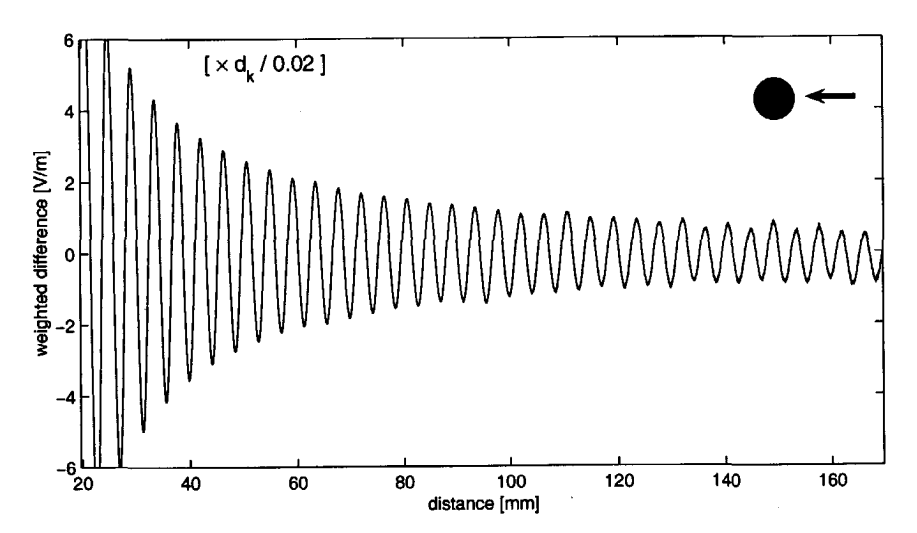


Figure 5.4: The weighted difference between the measured and simulated CG field responses, as a function of distance d_k .

estimate at the new antenna location. With this initial estimate the number of iterations needed to meet our error criterion of 2 % varies between P=0 and P=1. The values of the error during this procedure are plotted in

Fig. 5.2. From the starting point at $d_k = 169.7$ mm to 145 mm, the new initial estimate yields an error less than 2 % and no further iterations are needed (P = 0). Closer to the sphere, often one extra iteration (P = 1) is needed to meet the error criterion.

After computation of the surface field $\nu \times H$, we compute the scattered field with the representation of Eq. (4.13). In Fig. 5.3 we present the measured results (solid lines) and the computed results (dashed lines). We further want to quantify the difference between the results in more detail. In addition, to make the differences in the far field more visible we have multiplied the difference between the two results with a factor $d_k/0.02$, where d_k is the distance in meters. The results for this weighted difference are plotted in Fig. 5.4. From the latter two figures we observe that, the amplitudes of the field responses do match properly, but we observe a shift between the curves, which indicates that the shift calculated in Chapter 2 is not good enough. Probably, in the actual positioning of the sphere a small location error is made, and for a fair comparison we need a second calibration. To find the proper shift we perform exactly the same procedure as in Chapter 2, by shifting the computed results in such a way that the correlation of both responses is maximized. Before we carry out this second calibration we have to mention that the accuracy of the measurement is not reliable in the near field close to the sphere due to additional reflections from the antenna and the sledge of the antenna. For this reason we have performed the calibration in the range of 40 mm $< d_k < 160$ mm to find the proper shift. We find that the antenna configuration in the modeling has to be shifted over a distance of 1 mm.

After performing the second calibration, the measured and the simulated scattered field responses along the measurement range are depicted in Fig. 5.5 and the weighted difference between the two responses is plotted in Fig. 5.6. In these figures the two vertical dotted lines indicate the begin and end of our calibration range. We observe that the results match very good in the calibration area (see Fig. 5.6) and close to the sphere discrepancies occur. As already mentioned, these discrepancies are caused by mutual reflections between the sphere and the antenna configuration.

Physical-optics approximation (PO)

Next, we compare the measured result with a simulated result when we take the physical-optics (PO) approximation for the surface field. After

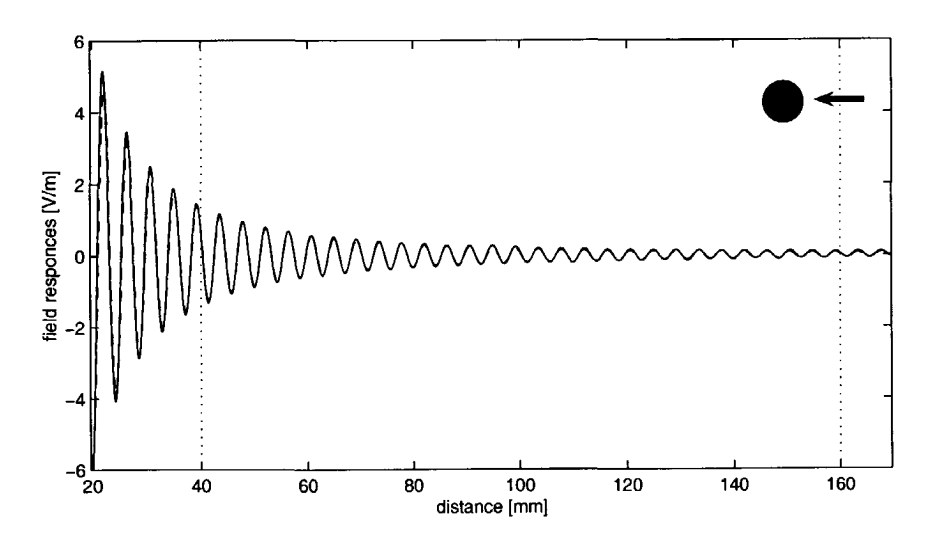


Figure 5.5: The measured (solid line) and simulated CG (dashed line) field responses as a function of distance d_k , after second calibration.

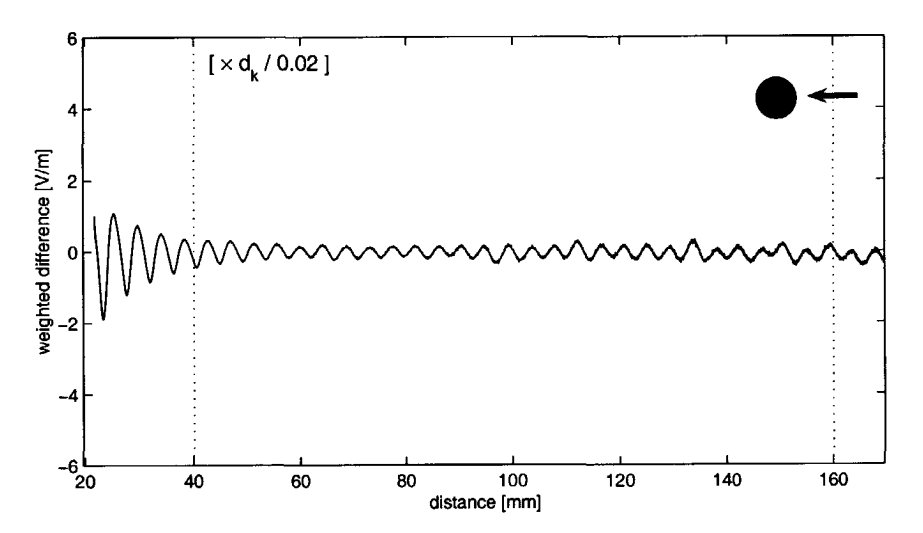


Figure 5.6: The weighted difference between the measured and simulated CG field responses, as a function of distance d_k , after second calibration.

computing the scattered field using this physical-optics approximation, and applying the extra shift found from the second calibration with the CG simulations, the results are depicted in Fig. 5.7 and the weighted difference

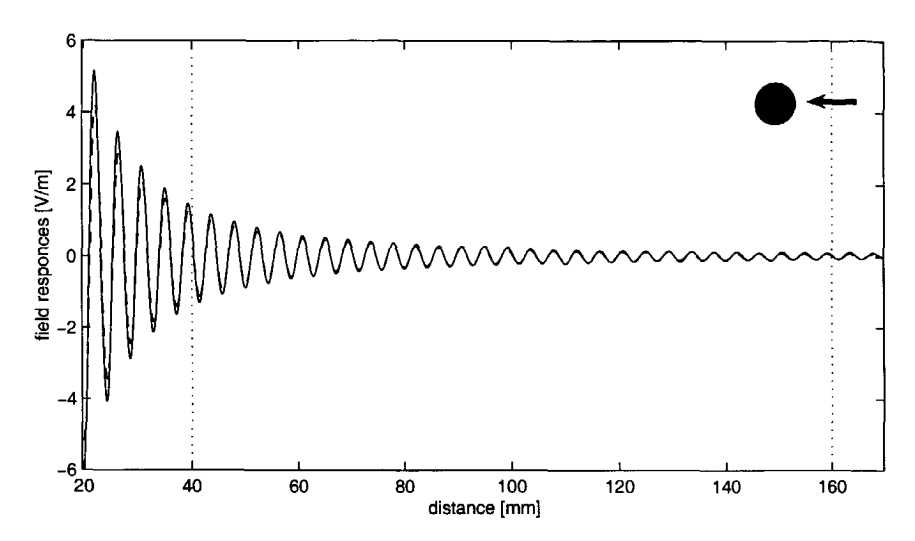


Figure 5.7: The measured (solid line) and simulated PO (dashed line) field responses as a function of distance d_k after second calibration.

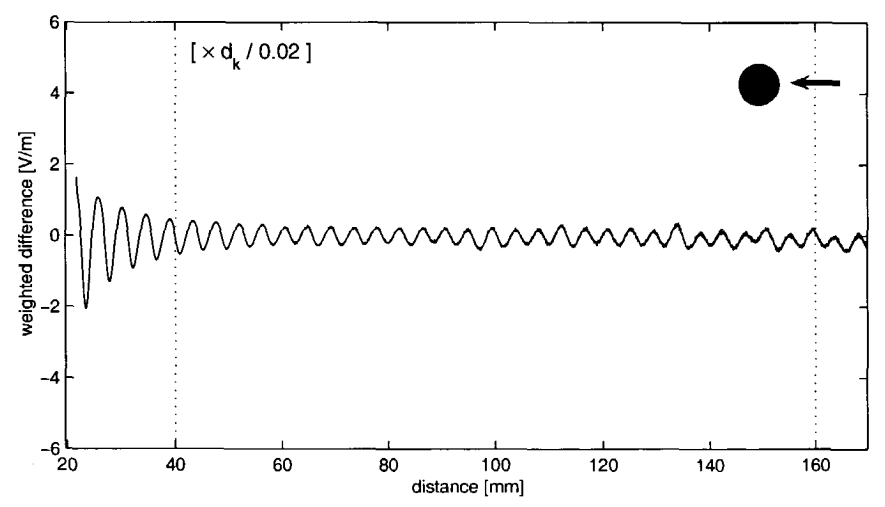


Figure 5.8: The weighted difference between the measured and simulated PO field responses as a function of distance d_k after second calibration.

between these two results in Fig. 5.8. We observe that the field responses do match properly. When we compare Fig. 5.8 with Fig. 5.6 we can conclude for this simple spherical-shaped scatterer the physical-optics approximations

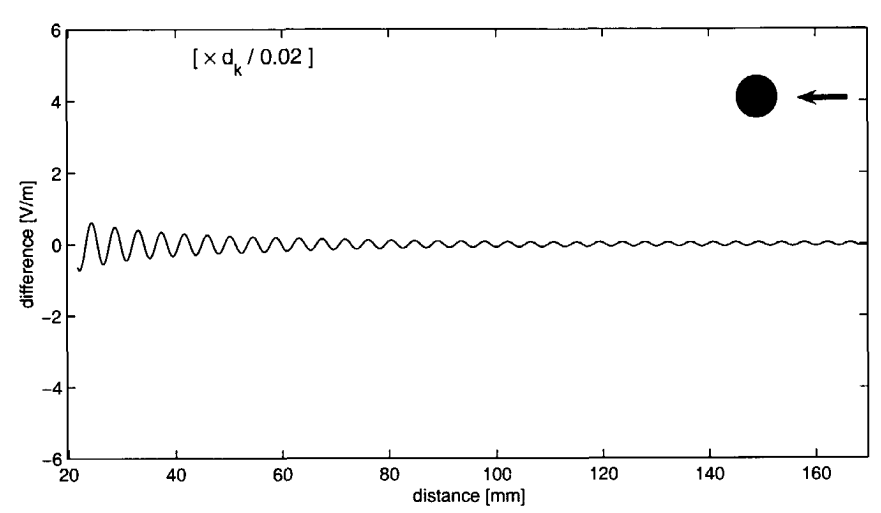


Figure 5.9: The weighted difference between the simulated CG and PO responses as a function of distance d_k .

performs very well.

In order to quantify the differences between the simulated CG results and the simulated PO results, we present the differences between these two results in Fig. 5.9. We note that these differences become larger in the near field of the scattering object.

5.2. Experiments with a finite cylinder

Secondly, we present the results for a finite cylinder made of aluminum. The radius, a, of the cylinder is 5 mm and the length is 30 mm. The cylinder is suspended from the sledge of the upper rail, while the dipole antenna which is located at the lower sledge is moved towards the barycenter of the cylinder. We consider again the barycenter of the cylinder as the origin of the coordinate system. In our computations, the dipole is positioned at $\mathbf{x}^T = \{0, 0, d + \Delta_d\}$, where the value of $\Delta d = 0.58$ mm is found from the shift correction explained in Chapter 2. The dipole antenna is moved along the z-axis towards the cylinder (Fig. 5.10). The parameter d is the varying distance between the dipole antenna and the scattering surface. The dipole is oriented in the y-direction with a dipole moment $I_{ant}\mathbf{L} = \{0, C, 0\}$, where the

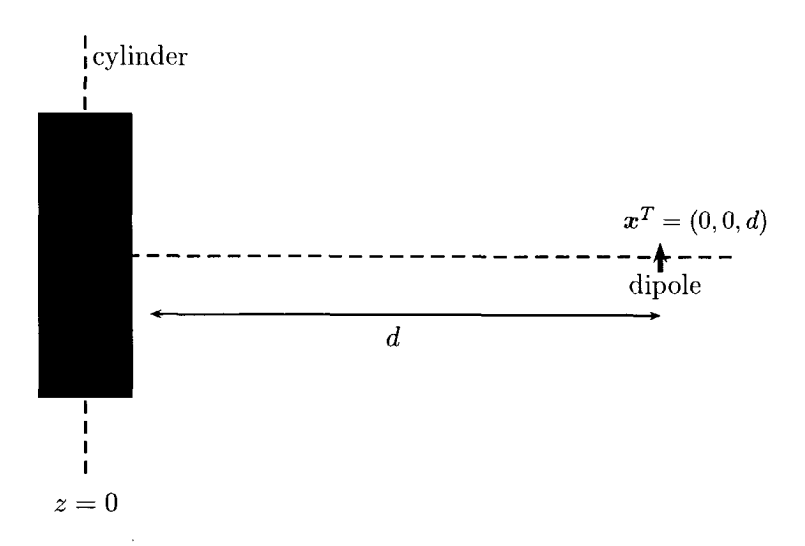


Figure 5.10: Dipole antenna moving towards the cylinder.

amplitude C of the dipole moment is found from the calibration procedure explained in Chapter 2. Since only the y-component of the scattered field is measured, we suffice by computing the y-component of the scattered field and the real part of this field component represents the reflected field amplitude E^r measured by the antenna system. When the antenna is moved towards the cylinder, the scattered electromagnetic fields are measured at certain discrete points along the range of 17 mm $< d_k < 157$ mm with a sampling unit of 0.04 mm. From the measured response we subtract its DC value. We calculated this DC value by taking the mean value of all the measurements.

In our computations we discretize the boundary surface S of the cylinder in 1972 plane triangular patches and the internal spherical surface S_{int} in 110 patches, which is sufficient enough to obtain the accuracy within not too much computation time (see Chapter 4).

Constrained conjugate gradient method (CG)

We first compute the surface field $\nu \times H$ with the constrained conjugate gradient method (CG) as developed in Chapter 4. We stop the iteration once an error less than 2 % is arrived at. The maximum number of iterations to

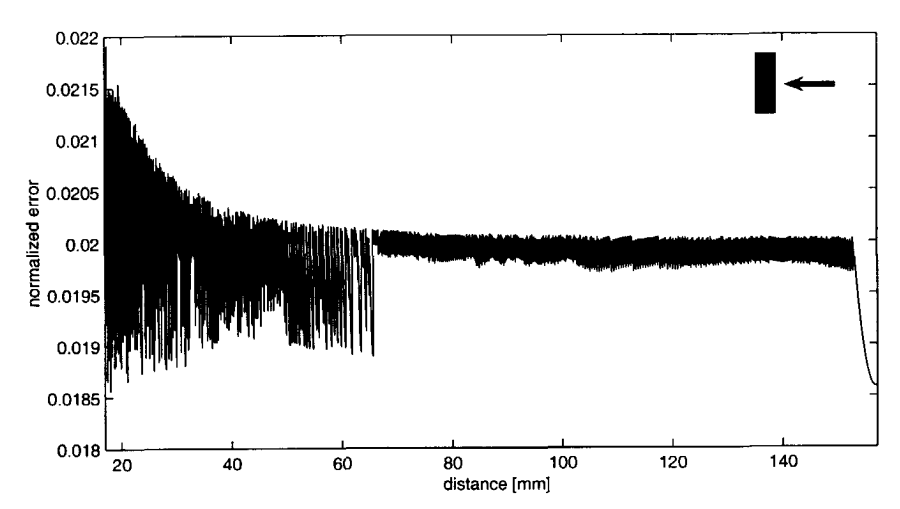


Figure 5.11: The error, ERR, as a function d_k in the simulation procedure.

meet this error criterion is denoted as P. Since we compute the scattered fields at certain discrete points, $k=1,2,\cdots,300$, along the measurement range, the field changes roughly with the factor $C_{k,k-1}$ of Eq. (5.1), and we use this factor to improve the initial estimate, when we change the antenna position from d_{k-1} to d_k . Our computational procedure is as follows. We start for k=1 with the physical-optics approximation, using Eq. (4.23), as an initial estimate and let the constrained conjugate gradient method iterate P times until it satisfies the error criterion of 2 %. For each new position of the dipole antenna we use the initial estimate of Eq. (5.2). With this initial estimate the number of iterations needed to meet our error criterion of 2 % varies between P=0 and P=4. The values of the error during this procedure are plotted in Fig. 5.11. From the starting point at $d_k=157$ mm to 70 mm, we need either the zero iteration or one extra iteration, while closer to the cylinder, two to four iterations are needed to meet the error criterion.

After computation of the surface field $\nu \times H$, we compute the scattered field with the representation of Eq. (4.13). In Fig. 5.12 we present the measured results (solid lines) and the computed results (dashed lines). We further want to quantify the difference between the results in more detail. In addition, to make the differences in the far field more visible we have multiplied the difference between the two results with a factor $d_k/0.02$,

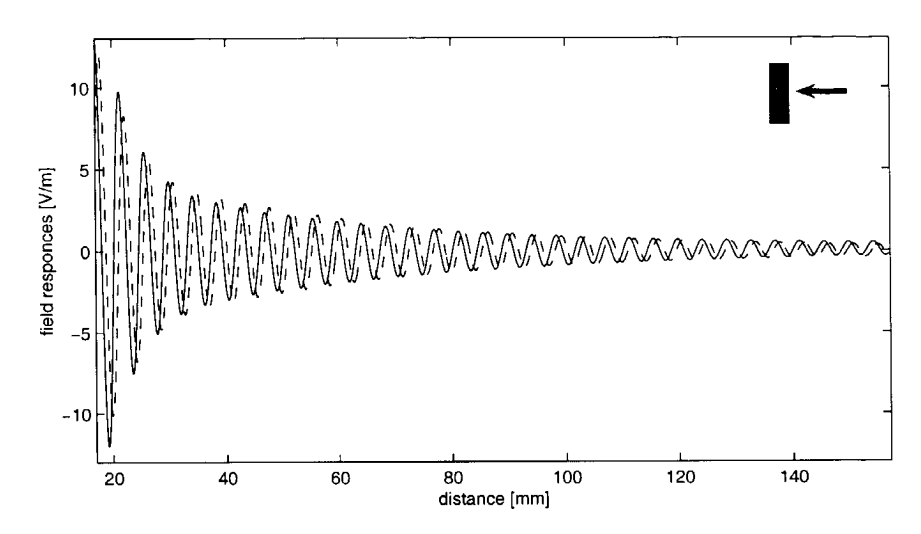


Figure 5.12: The measured (solid line) and simulated CG (dashed line) field responses as a function of distance d_k .

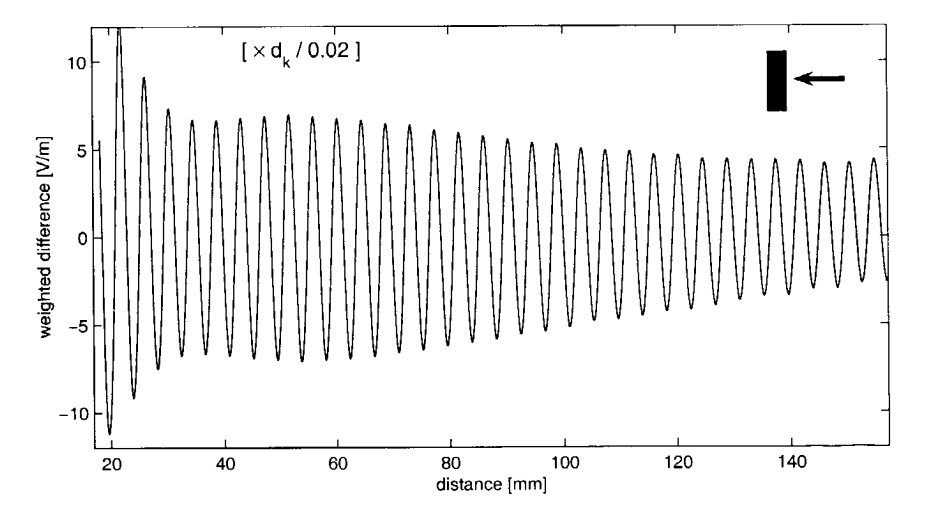


Figure 5.13: The weighted difference between the measured and simulated CG field responses as a function of distance d_k .

where d_k is the distance in meters. The results for this weighted difference are plotted in Fig. 5.13. From the latter two figures we observe that, the amplitudes of the field responses do match properly, but we observe a shift

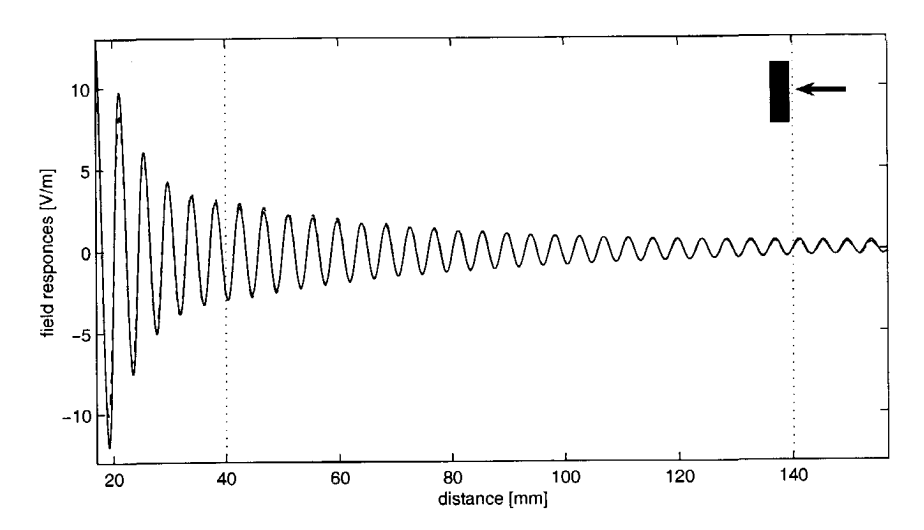


Figure 5.14: The measured (solid line) and simulated CG (dashed line) field responses as a function of distance d_k after second calibration.

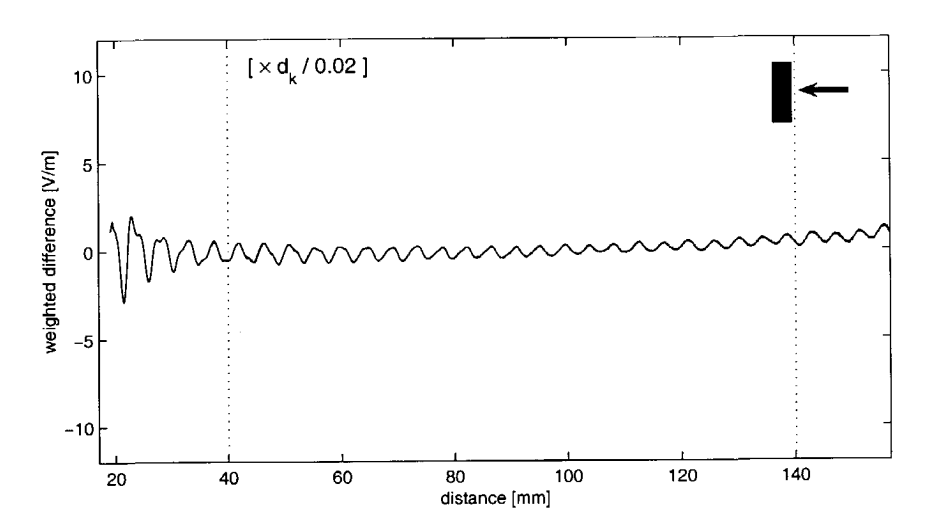


Figure 5.15: The weighted difference between the measured and simulated CG field responses as a function of distance d_k after second calibration.

between the curves, which indicates that the shift calculated in Chapter 2 is not good enough. Probably, again in the actual positioning of the cylinder a small location error is made, and for a fair comparison we need a second

calibration. To find the proper shift we perform exactly the same procedure as in Chapter 2, by shifting the computed results in such a way that the correlation of both responses is maximized. Before we carry out this second calibration we have to mention that the accuracy of the measurement is not reliable in the near field close to the cylinder due to additional reflections from the antenna and the sledge of the antenna. For this reason we have performed the calibration in the range of 40 mm $< d_k < 140$ mm to find the proper shift. We again find that the antenna configuration in the modeling has to be shifted over a distance of 1 mm.

After performing the second calibration, the measured and the simulated scattered field responses along the measurement range are depicted in Fig. 5.14, while the weighted difference between the two responses is plotted in Fig. 5.15. In these figures the two vertical dotted lines indicate the begin and end of our calibration range. We observe that the results match very good in the calibration range (see Fig. 5.15) and close to the cylinder discrepancies occur. As already mentioned, these discrepancies are caused by mutual reflections between the cylinder and the antenna configuration.

Physical-optics approximation (PO)

Next, we compare the measured result with a simulated result when we take the physical-optics (PO) approximation for the surface field. After computing the scattered field using this physical-optics approximation, and applying the extra shift found from the second calibration with the CG simulations, the results are depicted in Fig. 5.16 and the weighted difference between these two results in Fig. 5.17. We observe that the field responses do match properly. When we compare Fig. 5.17 with Fig. 5.15 we can conclude that for this simple scatterer the physical-optics approximations performs reasonably well.

In order to quantify the differences between the simulated CG results and the simulated PO results, we present the differences between these two results in Fig. 5.18. When we compare these differences with the ones of Fig. 5.9 we observe that, for the scattering by a sphere, the physical-optics approximation was a reasonable approximation, certainly in the far-field zone, but that in the present case of the scattering by a finite cylinder the discrepancies become more pronounced in the intermediate-field and near-field zones. Furthermore, at the start of the measurements, a DC value is present. This is caused by the presence of some residual charge in the elec-

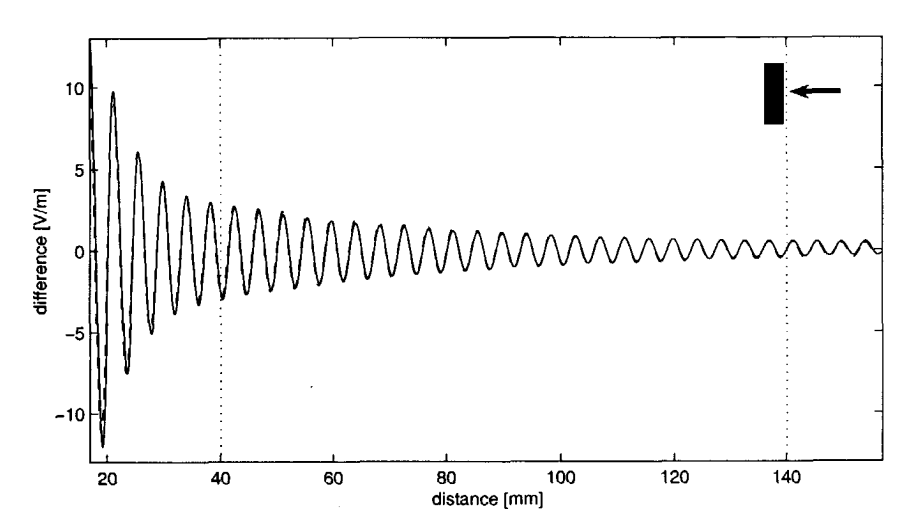


Figure 5.16: The measured (solid line) and simulated PO (dashed line) field responses as a function of distance d_k after second calibration.

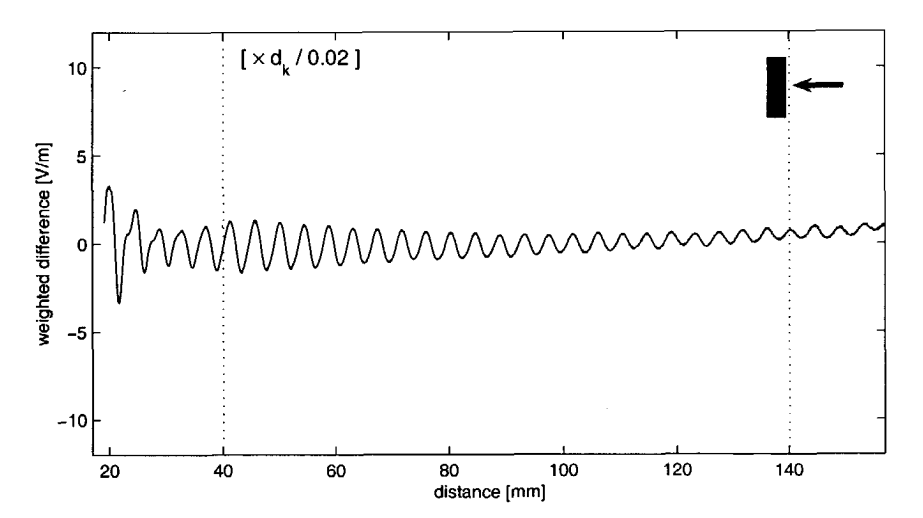


Figure 5.17: The weighted difference between the measured and simulated PO field responses as a function of distance d_k after second calibration.

tronic system. This charge decreases as a function of time, which is visible as a function of position. Although the differences between the CG results and the PO results are of the same order as the differences between the mea-

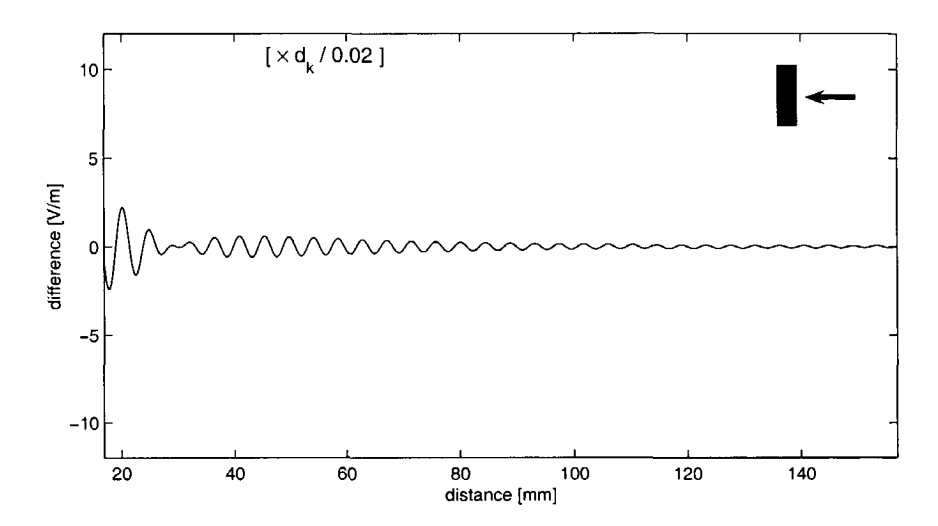


Figure 5.18: The weighted difference between the simulated CG and PO field responses as a function of distance d_k .

surements and the CG results we surmise that for a more complicated object the physical-optics approximation will not be useful anymore. Therefore, at the end of this chapter we model a more complicated object, viz., the capped box. But first we discuss the experiments with a finite flat plate.

5.3. Experiments with a finite flat plate

Thirdly, we present the results for a finite plate made of aluminum. The plate has a dimension of $20 \times 20 \text{ mm}^2$ base and 3 mm thickness. In able to support the plate a small box is attached on the back side with dimensions of $6 \times 6 \text{ mm}^2$ base and 7 mm thickness. This support box has a small hole to be fixed on a bar. The plate and the support box form one aluminum object. The dipole antenna which is located at the lower sledge is moved towards the barycenter of the plate (Fig. 5.19). We consider again the barycenter of the plate as the origin of the coordinate system. In our computations, the dipole is positioned at $x^T = \{0, 0, d + \Delta d\}$, where the value of $\Delta d = 0.58$ mm is found from the shift correction explained in Chapter 2. The dipole antenna is moved along the z-axis towards the plate (Fig. 5.20). The parameter d is the varying distance between the dipole antenna and the

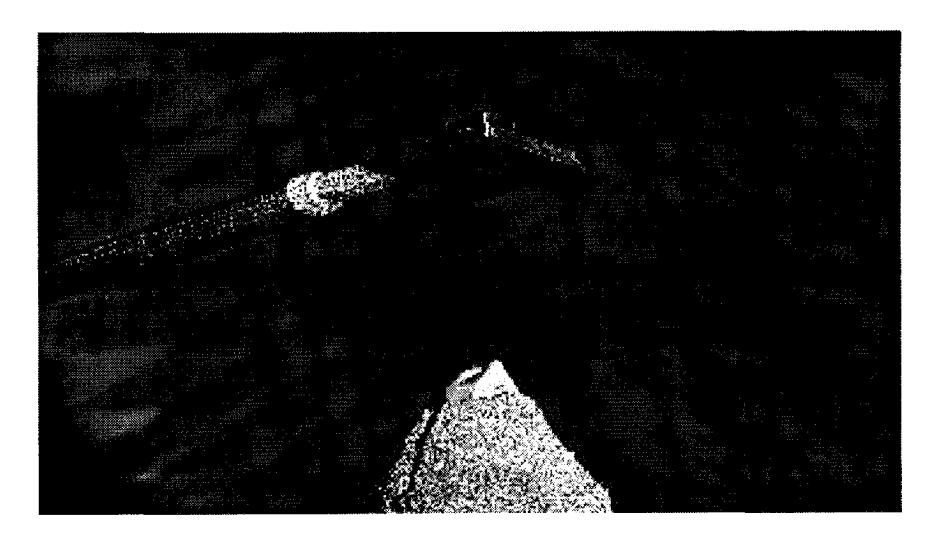


Figure 5.19: The finite plate.

scattering surface. The dipole is oriented in the y-direction with a dipole moment $I_{ant}L = \{0, C, 0\}$, where the amplitude C of the dipole moment is found from the calibration procedure explained in Chapter 2. Since only the y-component of the scattered field is measured, we suffice by computing the y-component of the scattered field and the real part of this field component represents the reflected field amplitude E^r measured by the antenna system. When the antenna is moved towards the plate, the scattered electromagnetic fields are measured at certain discrete points along the range of 6 mm $< d_k < 100$ mm with a sampling unit of 0.04 mm. From the measured response we subtract its DC value. We calculated this DC value by taking the mean value of all the measurements.

In our computations we discretize the boundary surface S of the plate with support box in 5400 plane triangular patches and the internal spherical surface S_{int} in 110 patches, which is sufficient enough to obtain the accuracy within not too much computation time (see Chapter 4).

Constrained conjugate gradient method (CG)

We first compute the surface field $\nu \times H$ with the constrained conjugate gradient method (CG) as developed in Chapter 4. We stop the iteration once an error less than 4 % is arrived at. The maximum number of iterations to

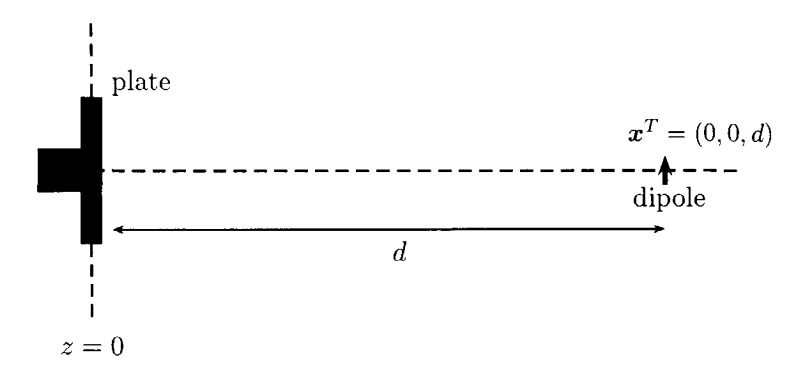


Figure 5.20: Dipole antenna moving towards the finite plate.

meet this error criterion is denoted as P. Since we compute the scattered fields at certain discrete points, $k=1,2,\cdots,300$, along the measurement range, the field changes roughly with the factor $C_{k,k-1}$ of Eq. (5.1), and we use this factor to improve the initial estimate, when we change the antenna position from d_{k-1} to d_k . Our computational procedure is as follows. We start for k=1 with the physical-optics approximation, using Eq. (4.23), as an initial estimate and let the constrained conjugate gradient method iterate P times until it satisfies the error criterion of 4 %. For each new position of the dipole antenna we use the initial estimate of Eq. (5.2). With this initial estimate the number of iterations needed to meet our error criterion of 4 % varies between P=0 and P=8. The values of the error during this procedure are plotted in Fig. 5.21. In this figure we observe that closer to the scattering object the error with respect to the initial estimate increases and the number of iterations needed to meet the error criterion increases as well.

After computation of the surface field $\nu \times H$, we compute the scattered field with the representation of Eq. (4.13). In Fig. 5.22 we present the measured results (solid lines) and the computed results (dashed lines). We further want to quantify the difference between the results in more detail. In addition, to make the differences in the far field more visible we have multiplied the difference between the two results with a factor $d_k/0.02$, where d_k is the distance in meters. The results for this weighted difference are plotted in Fig. 5.23. From the latter figure we observe that, the amplitudes of the field responses do match properly until $d_k = 30$ mm and after that the measured result shows an amplifier error since the mixer of the trajectory

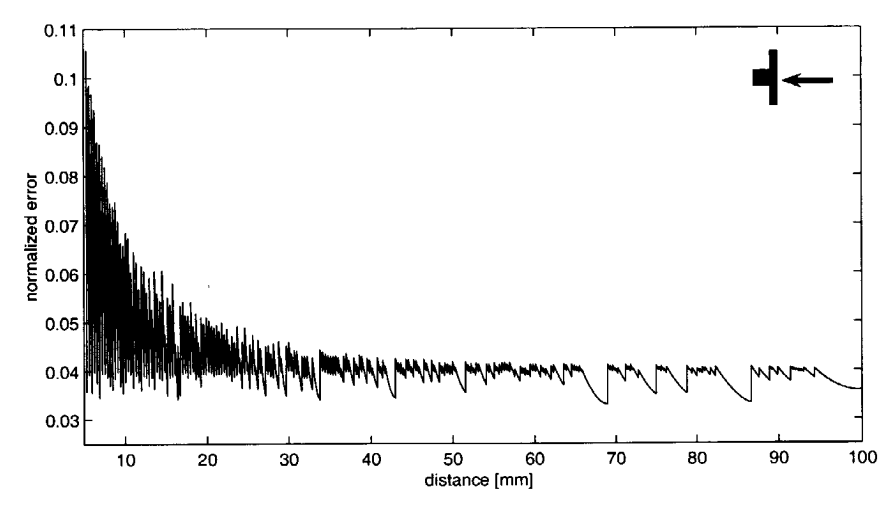


Figure 5.21: The error, ERR, as a function d_k in the simulation procedure.

simulator do not operate properly anymore. Further we also observe a shift between the curves, which indicates that the shift calculated in Chapter 2 is not good enough. Probably, again in the actual positioning of the plate a small location error is made, and for a fair comparison we need a second calibration. To find the proper shift we perform exactly the same procedure as in Chapter 2, by shifting the computed results in such a way that the correlation of both responses is maximized. Before we carry out this second calibration we have to mention that the accuracy of the measurement is not reliable in the near field close to the plate due to additional reflections from the antenna and the sledge of the antenna. For this reason we have performed the calibration in the range of 35 mm $< d_k < 90$ mm to find the proper shift. We find that the antenna configuration in the modeling has to be shifted over a distance of 0.4 mm.

After performing the second calibration, the measured and the simulated scattered field responses along the measurement range are depicted in Fig. 5.24, while the weighted difference between the two responses is plotted in Fig. 5.25. In these figures the two vertical dotted lines indicate the begin and end of our calibration range. We observe that the results match very good in the calibration range (see Fig. 5.25) and close to the cylinder discrepancies occur. As already mentioned, these discrepancies are caused by mutual reflections between the scatterer and the antenna configuration.

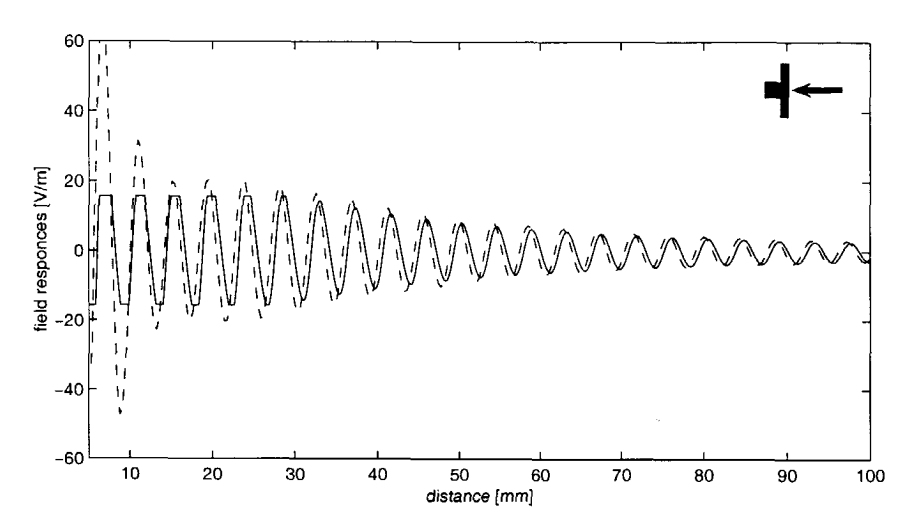


Figure 5.22: The measured (solid line) and simulated CG (dashed line) field responses as a function of distance d_k .

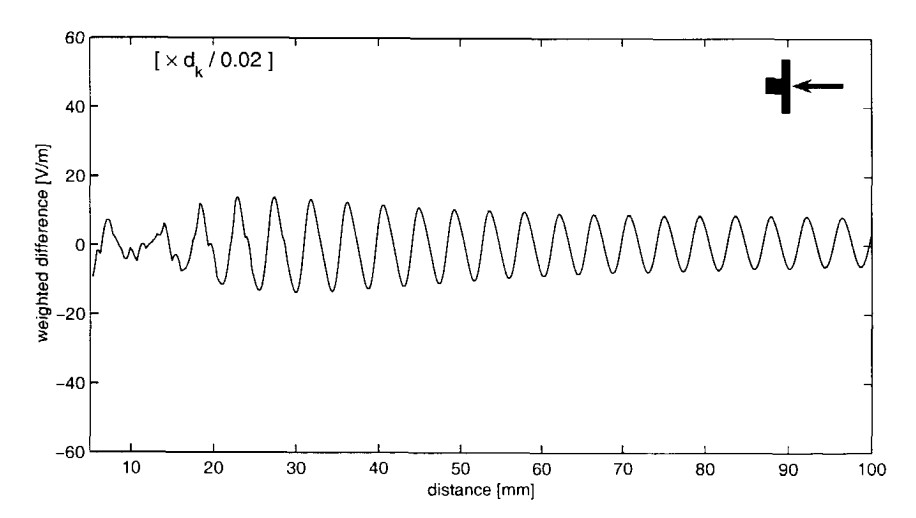


Figure 5.23: The weighted difference between the measured and simulated CG field responses as a function of distance d_k .

Physical-optics approximation (PO)

Next, we compare the measured result with a simulated result when we take the physical-optics (PO) approximation for the surface field. After

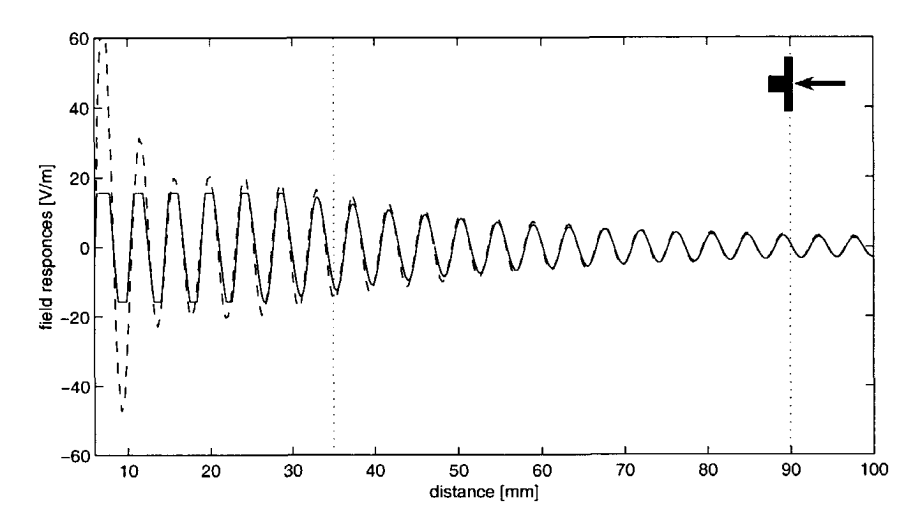


Figure 5.24: The measured (solid line) and simulated CG (dashed line) field responses as a function of distance d_k after second calibration.

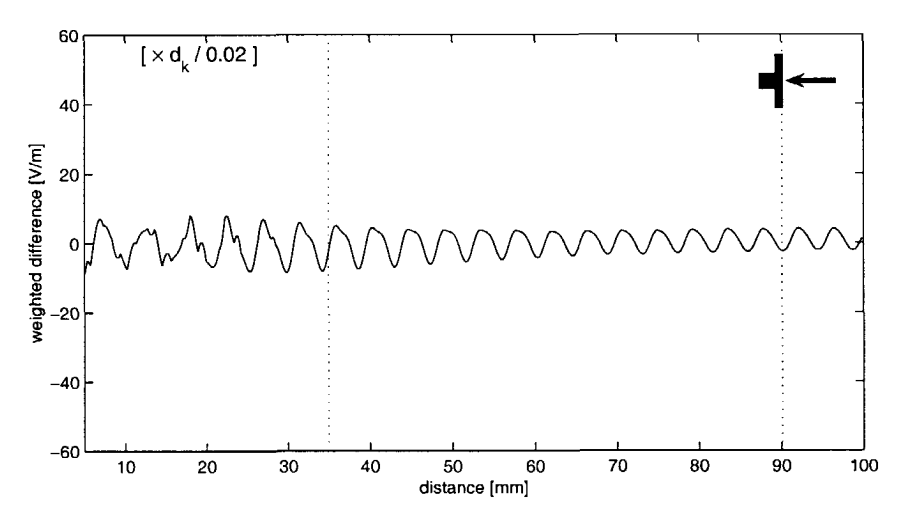


Figure 5.25: The weighted difference between the measured and simulated CG field responses as a function of distance d_k after second calibration.

computing the scattered field using this physical-optics approximation, and applying the extra shift found from the second calibration with the CG simulations, the results are depicted in Fig. 5.26 and the weighted difference between these two results in Fig. 5.27. We observe that the field responses do

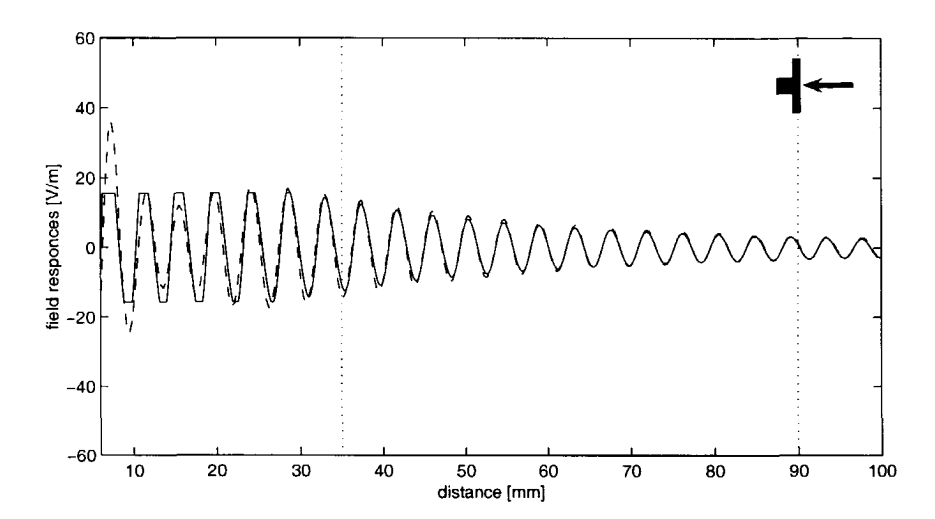


Figure 5.26: The measured (*solid line*) and simulated PO (*dashed line*) responses as a function of distance d_k after second calibration.

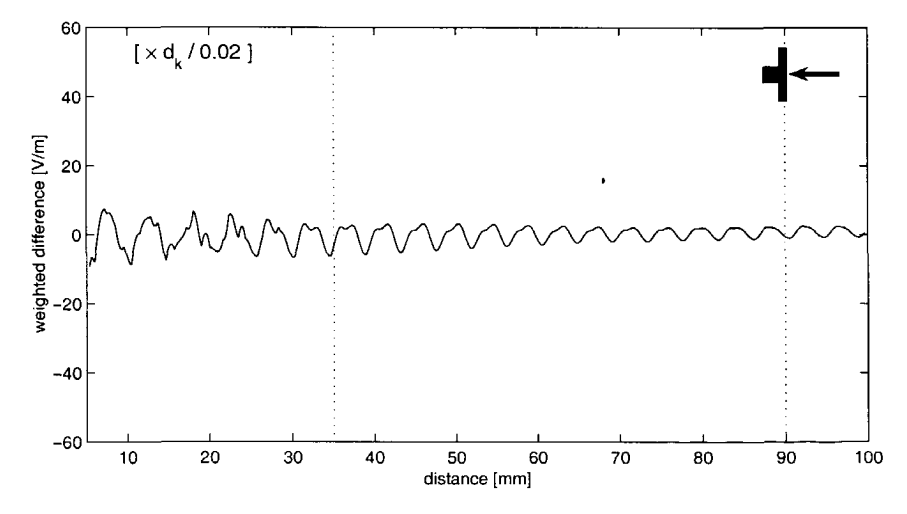


Figure 5.27: The weighted difference between the measured and simulated PO field responses as a function of distance d_k after second calibration.

match properly. When we compare Fig. 5.27 with Fig. 5.25 we can conclude that for this simple finite plate the physical-optics approximations performs reasonably well.

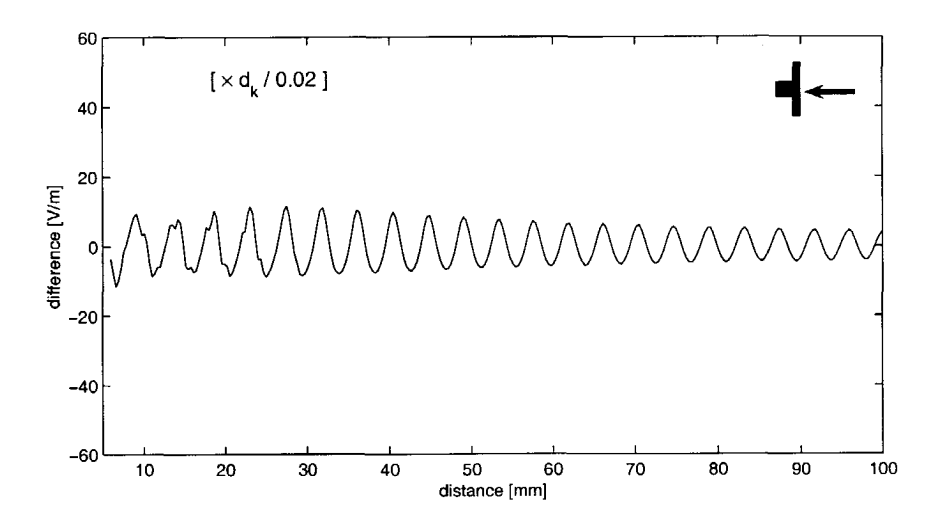


Figure 5.28: The weighted difference between the simulated CG and PO field responses as a function of distance d_k .

In order to quantify the differences between the simulated CG results and the simulated PO results, we present the differences between these two results in Fig. 5.28. When we compare these differences with the ones of Fig. 5.9, we observe that, for the scattering by a sphere, the physical-optics approximation was a reasonable approximation, certainly in the far-field zone, but that in the present case of the scattering by a finite plate the discrepancies becomes more pronounced in the intermediate-field and near-field zones. Although the differences between the CG results and the PO results are of the same order as the differences between the measurements and the CG results we surmise that for a more complicated object the physical-optics approximation will not be useful anymore.

5.4. Experiments with a capped box

In the previous sections, for some simple canonical objects (sphere, cylinder and plate), we compared the measured results and computed results using both the physical-optics approximation and the conjugate gradient method for simple objects. In these comparisons we observed that the results using the physical-optics approximation are slightly worse than the results using

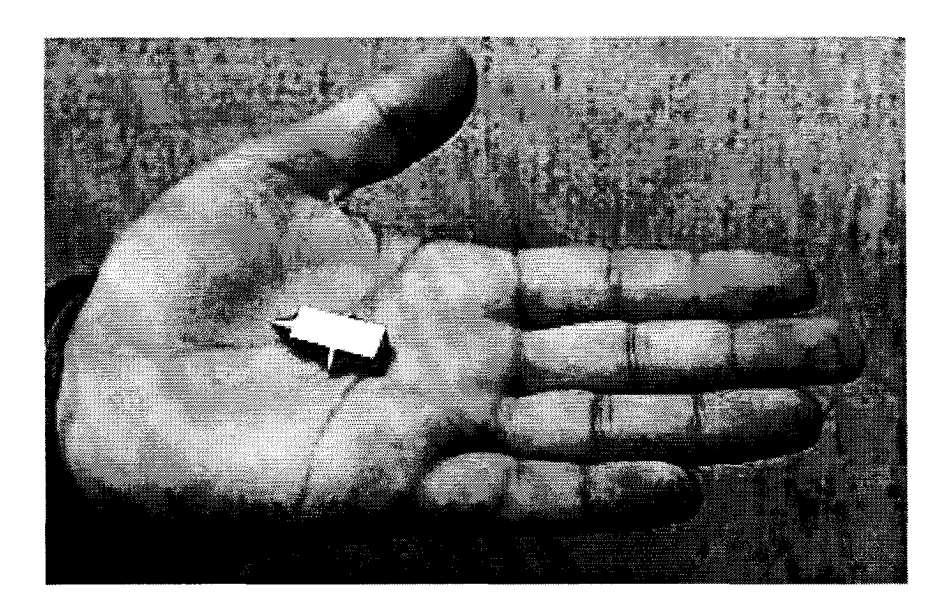


Figure 5.29: The capped box in a hand.

the conjugate gradient method, but still one can conclude that the physicaloptics approximation is a reasonable approximation.

In this section we consider a more complicated object. We present the results simulated numerically, using either the physical-optics approximation or the conjugate gradient method. We take a box capped with three cones made of aluminum (see Fig. 5.29 and Fig. 5.30). The box has a length of 2 cm and a cross-section of 0.8×0.8 cm². At the front end, the box is capped with a right circular cone; this cone has a height of 1 cm and a basis cross-section with a radius of 0.4 cm. In addition on two opposite sides we have placed cones with a height of 0.4 cm and a basis cross-section with a radius of 0.4 cm. We consider the barycenter of the box of the capped box as the origin of the coordinate system. In our computations, the dipole is positioned at $\mathbf{x}^T = \{0, 0, d\}$. The dipole antenna is moved along the z-axis towards the cylinder (Fig. 5.31). The parameter d is the varying distance between the dipole antenna and the scattering surface. The dipole is oriented in the y-direction with a dipole moment $I_{ant}L = \{0, C, 0\}$. We compute only the y-component of the scattered field in accordance with measurements and the real part of this field component represents the reflected field amplitude E^r measured by the antenna system. When the antenna is moved towards the

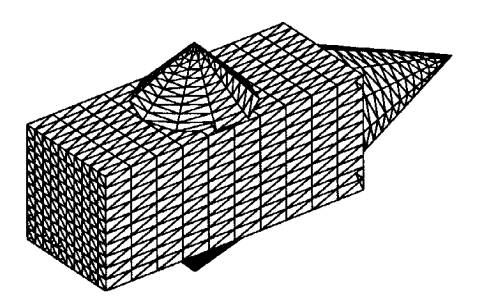


Figure 5.30: The capped box.

capped box, the scattered electromagnetic fields are computed at certain discrete points along the measurement range with a sampling unit of 0.5 mm. We compare the results for three different orientations of the capped box. The results are presented after the amplitude and phase correction as performed in previous sections.

In our computations we discretize the boundary surface into 1888 patches, which is a discretization of five to six points per wavelength. The interior surface is the same as before, viz., a sphere with a radius of 2 mm, and discretized into 110 patches.

(i) Firstly, we position the capped box as depicted in Fig. 5.31 and move the antenna to the front cone of the scattering object. The measurement range is 20 mm $< d_k < 110$ mm. We compute the surface field $\nu \times H$ with the constrained conjugate gradient method (CG) as developed in Chapter 4. We stop the iteration once an error less than 5 % is arrived at. The maximum number of iterations to meet this error criterion is denoted as P. Since we compute the scattered fields at certain discrete points, $k = 1, 2, \dots, 300$, along the computation range, the field changes roughly with the factor $C_{k,k-1}$ of Eq. (5.1), and we use this factor to improve the initial estimate, when we change the antenna position from d_{k-1} to d_k . We start for k=1 with the physical-optics approximation, using Eq. (4.23), as an initial estimate. The error when using this physical-optics approximation as initial estimate is 123 % and in the first iteration it decreases to 70 %. For each new position of the dipole antenna we use the initial estimate of Eq. (5.2). Then, the number of iterations needed to meet our error criterion of 5 % varies between P=0 and P=8. The values of the error during this procedure are plotted in Fig. 5.32, except for the first antenna position (k = 1). In this figure we observe that

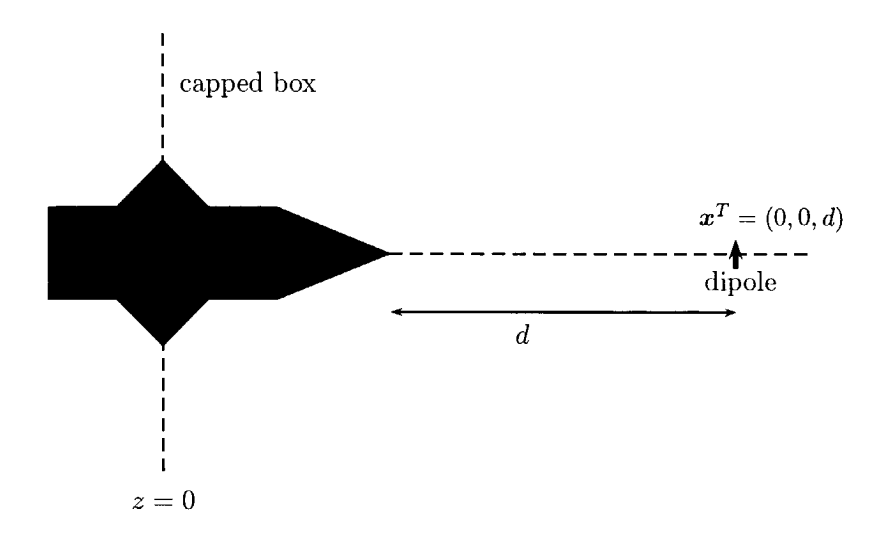


Figure 5.31: Dipole antenna moving towards the front cone of the capped box.

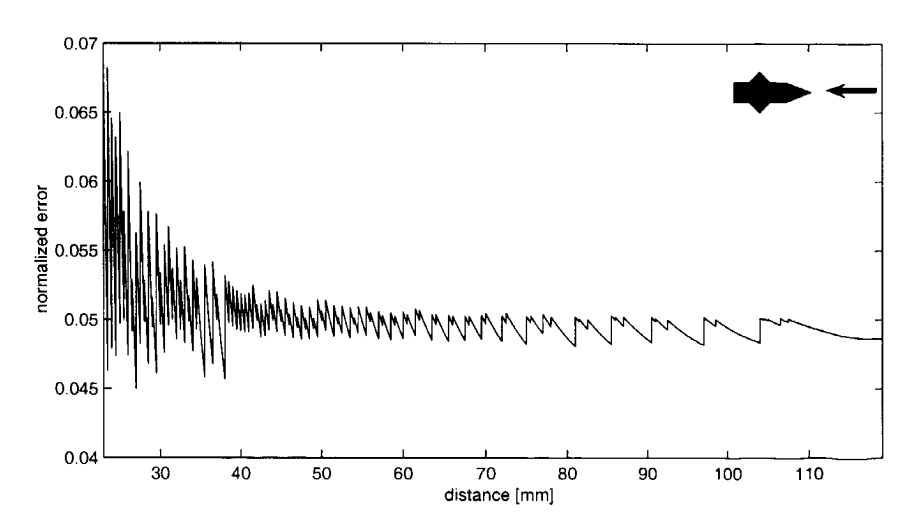


Figure 5.32: The error, ERR, as a function d_k in the simulation procedure.

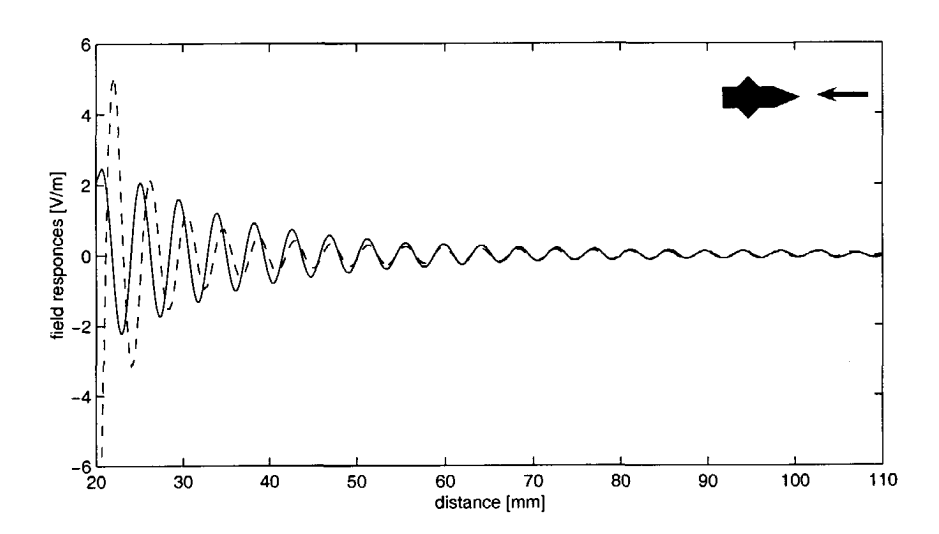


Figure 5.33: The measured (solid line) and simulated CG (dashed line) field responses as a function of distance d_k .

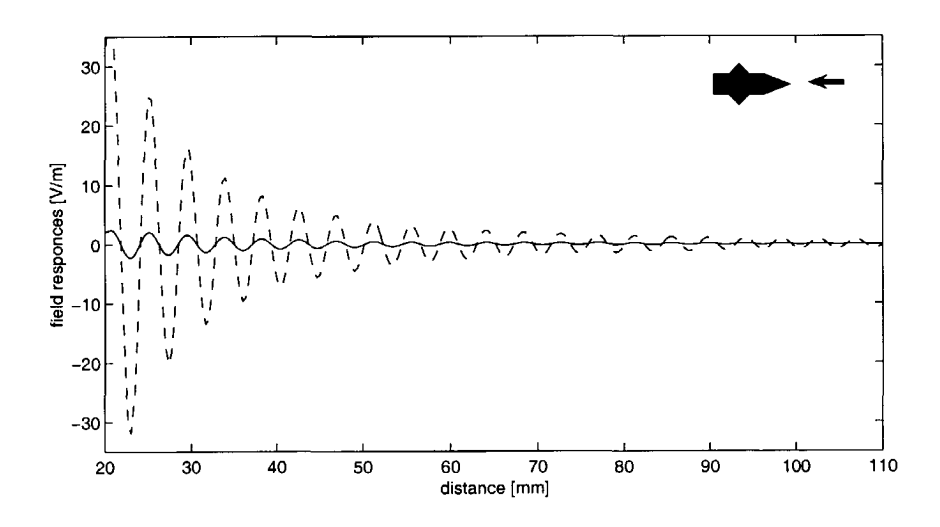


Figure 5.34: The measured (solid line) and simulated PO (dashed line) field responses as a function of distance d_k .

closer to the scattering object the error with respect to the initial estimate increases and the number of iterations needed to meet the error criterion increases as well. After computation of the surface field $\nu \times H$ with the CG method and the PO method, we compute the scattered fields with the representation of Eq. (4.13). In Fig. 5.33 we present the measured results (solid lines) and computed results with CG (dashed lines). We observe that the computed results with CG do match reasonable in the far field but closer to the scatterer a phase shift occurs. This is probably due to the difference between the modeled and actual form and position of the apex of the front cone. A different location between the modeled and actual one may be responsible for the shift observed in the near-field responses. In Fig. 5.34 we present the measured results (solid lines) and computed results with PO (dashed lines). We observe that the results with PO differs apparently from the measured results. This is also in accordance with the 123 % error when we take PO as initial estimate for CG.

(ii) Secondly, we position the capped box as depicted in Fig. 5.35 and

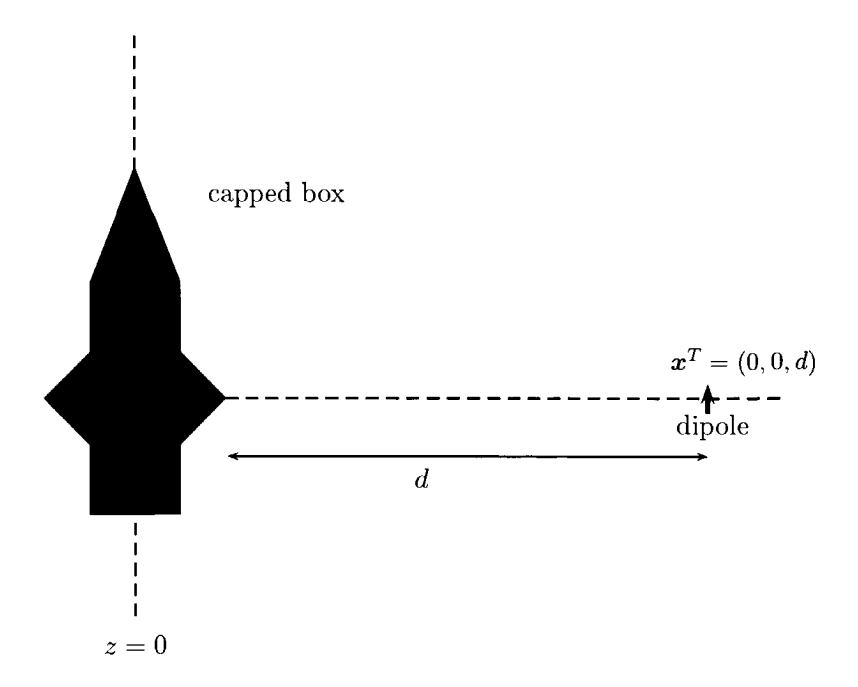


Figure 5.35: Dipole antenna moving towards a side cone of the capped box.

move the antenna to a side cone of the capped box. The measurement range is 17 mm $< d_k < 110$ mm. We used the same computation procedure as described in the first positioning. The error with physical-optics approximation as initial estimate is 135 % and in the first iteration it decreases to 59%. For each new position of the dipole antenna we use the initial estimate of Eq. (5.2). With this initial estimate the number of iterations needed to meet our error criterion of 5 % varies between P=0 and P=7. The values of the error during this procedure are plotted in Fig. 5.36, except for the first antenna position. After computation of the surface field $\nu \times H$ both with the CG method and the PO method, we compute the scattered fields with the representation of Eq. (4.13). In Fig. 5.37 we present the measured results (solid lines) and computed results with CG (dashed lines). We observe that the computed results with CG do match properly in the far field and intermediate field but in the near field a slight difference occurs in the amplitude. Again this is probably due to the difference in form and position between the modeled one and the actual apex of the side cone, although the present discrepancies are much smaller than the ones of the former case, where the front cone has been approached. In Fig. 5.38 we again present the measured results (solid lines) and computed results with PO (dashed lines). We observe that the results with PO differs apparently from the measured results, but less worse than in the previous case, where the front cone has

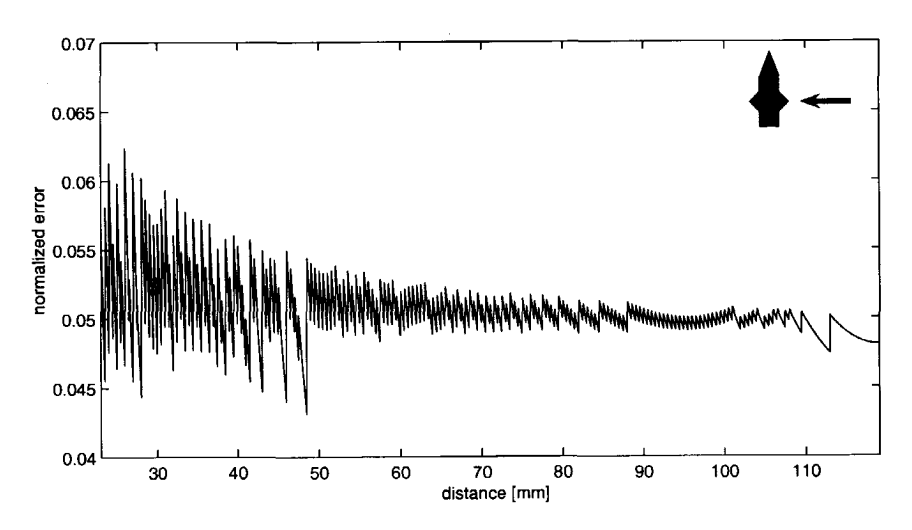


Figure 5.36: The error, ERR, as a function d_k in the simulation procedure.

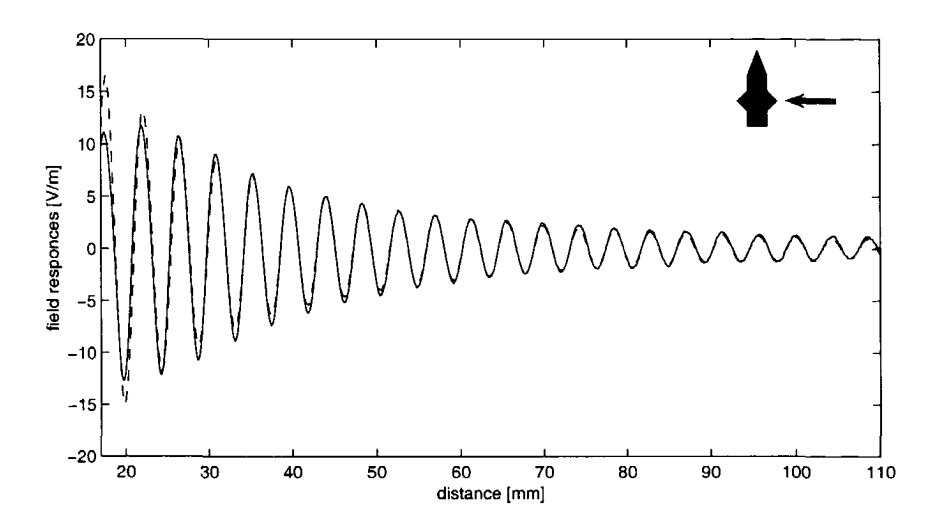


Figure 5.37: The measured (solid line) and simulated CG (dashed line) field responses as a function of distance d_k .

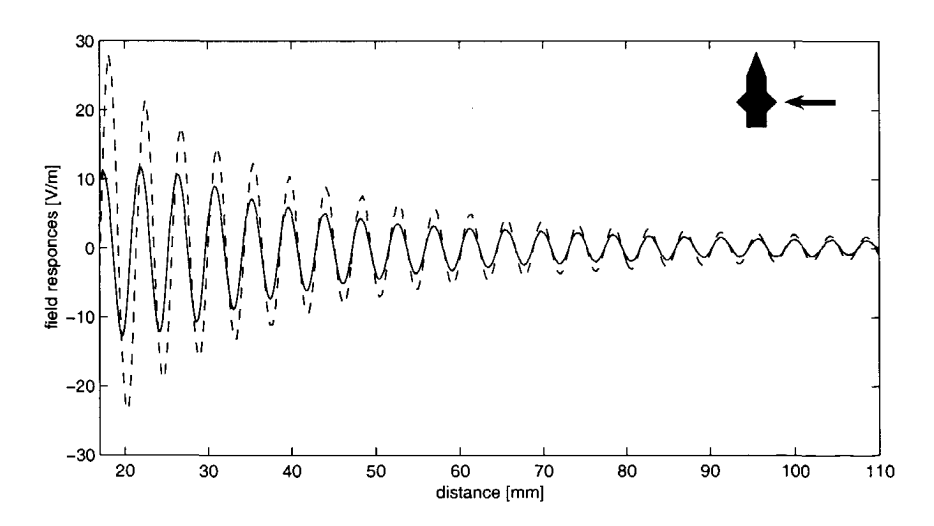


Figure 5.38: The measured (solid line) and simulated PO (dashed line) field responses as a function of distance d_k .

been approached. The side cone has a less pronounced apex.

(iii) Thirdly, we position the capped box as depicted in Fig. 5.35 and move the antenna to the bulk of the capped box. We used the same computation procedure as described for the first orientation of the object. By computing the surface field $\nu \times H$ with the constrained conjugate gradient method (CG) we start again for k=1 with the physical-optics approximation, using Eq. (4.23), as an initial estimate and let the constrained conjugate gradient method iterate P times until it satisfies the error criterion of 5 %. The error with physical-optics approximation as initial estimate is 75 % and in the first iteration it decreases to 53 %. For each new position of the dipole antenna we use the initial estimate of Eq. (5.2). With this initial estimate the number of iterations needed to meet our error criterion of 5 % varies between P=0 and P=3. The values of the error during this procedure are plotted in Fig. 5.40, except the first point. After computation of the surface field $\nu \times H$ with the CG method and the PO method, we compute the scattered

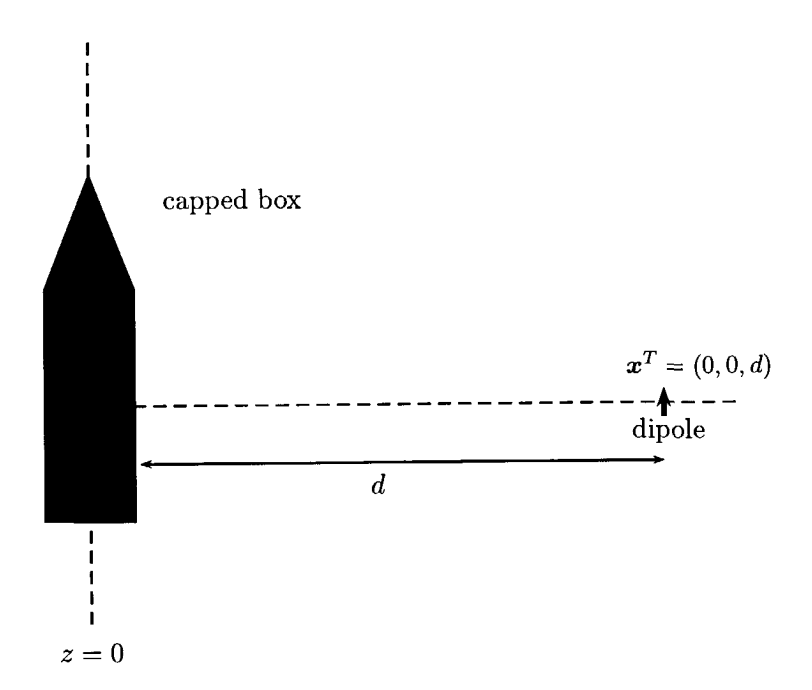


Figure 5.39: Dipole antenna moving towards the plane side of the capped box.

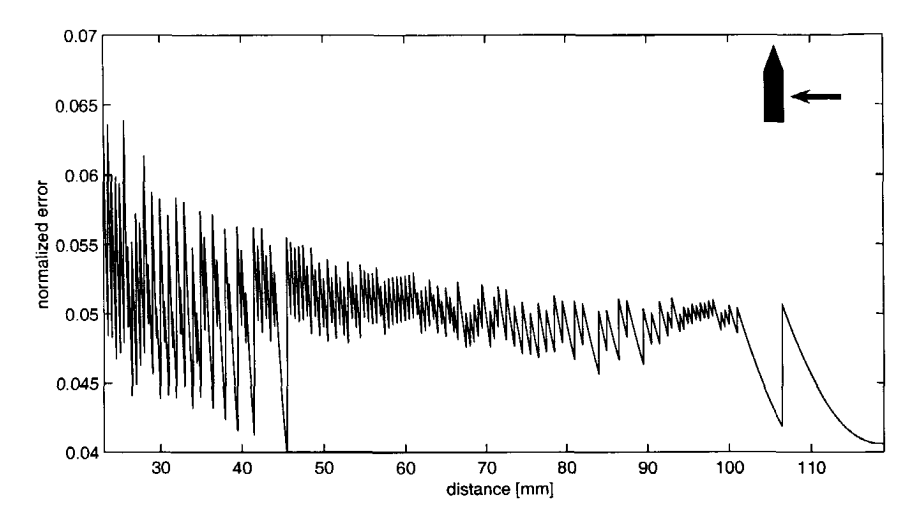


Figure 5.40: The error, ERR, as a function d_k in the simulation procedure.

fields with the representation of Eq. (4.13). In Fig. 5.41 we present the measured results (solid lines) and computed results with CG (dashed lines). We observe that the computed results with CG do match very good in the far field and intermediate field but in the near field an amplifier error occurs during the measurement. This also occurs in the case of the flat plate. In the near field, the strong reflected field response causes problems in the electronic circuit of the mixer of the trajectory simulator. In Fig. 5.42 we present the measured results (solid lines) and computed results with PO (dashed lines). We observe that the results with PO do match properly in the far field and intermediate field. In the near field discrepancies show up, but they are not as pronounced as in the former cases where the front and side cones have been approached.

When we compare the figures for the three orientations of the capped box, we observe the following. In the first orientation, when the antenna moves to the front cone with a height of 1 cm, there are large discrepancies between the CG results and the PO results (see Fig. 5.33 and Fig. 5.34). In the second orientation, when the antenna moves to a side cone, the agreement between the two results are slightly better (see Fig. 5.37 and Fig. 5.38). The side-cone has a height of 0.4 cm, so that the side cone is less sharp than the front cone. Further, we note that the characteristic dimensions of the cones

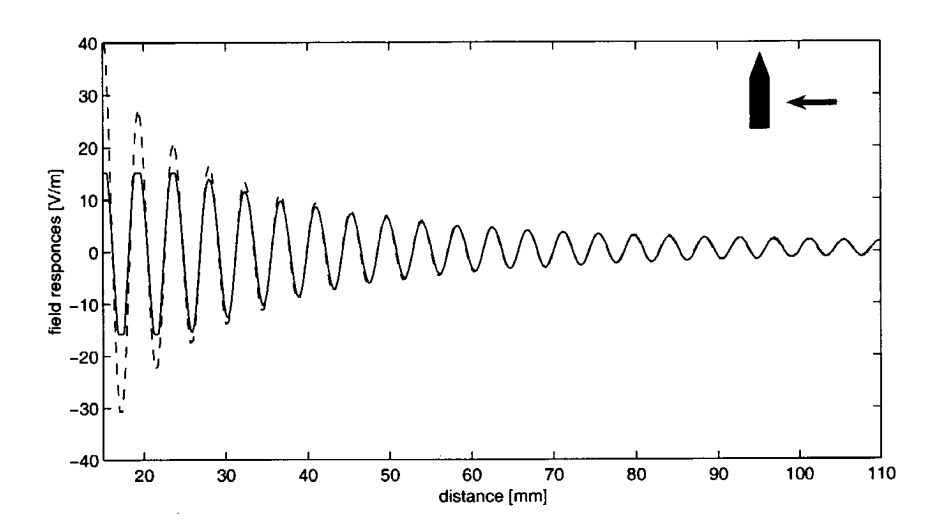


Figure 5.41: The measured (solid line) and simulated CG (dashed line) field responses as a function of distance d_k .

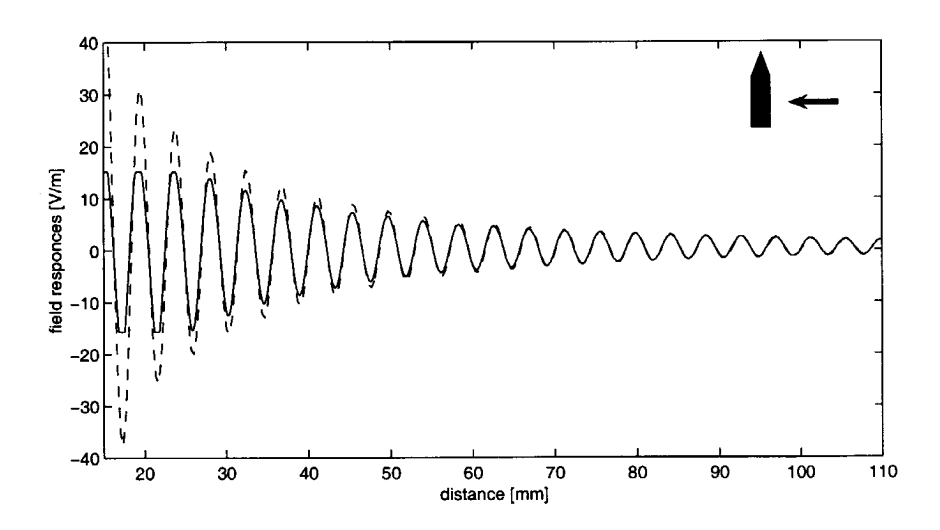


Figure 5.42: The measured (solid line) and simulated PO (dashed line) field responses as a function of distance d_k .

are less or equal to a wavelength, so that it is not expected that the physicaloptics approximation will yield acceptable results. In the third orientation, when the antenna moves to a flat side of the capped box, the agreement becomes better (see Fig. 5.41 and Fig. 5.42).

When we also compare the CG and PO results with the measurements, we conclude that our simulation based on the constrained CG method yields reliable results, as long as the modeled configuration presents the actual scatterer accurately enough. The physical-optics approximation, however, cannot be used for complicated scatterers.



Chapter 6

Conclusions

In this thesis we have developed a simple and efficient computational method to calculate the electromagnetic scattering for perfectly conducting objects. In particular, we derived integral representations for the scattered electromagnetic fields. Subsequently, in these representations the only unknown field quantity, the tangential component of the magnetic field, has been studied. We derived two types of boundary integral equations for this unknown surface field, one of the electric type and one of the magnetic type. In view of some non-uniqueness problems, we also required consistency of the integral representations in the interior of the scattering object. As a point of departure the magnetic-field boundary integral equation was chosen for solving the unknown surface field in view of the computational simplicity.

To solve the boundary integral equation of the magnetic type we used the conjugate gradient method as an iterative solver. We observed that the solution of our integral equation is not unique at certain frequencies in the presence of interior resonances. In order to restore uniqueness, we used the interior integral representation over a closed interior surface as a constraint for the conjugate gradient method. To that end, the problem is posed as an optimization problem in which an error norm of two terms is minimized. The first term is the normalized error norm with respect to the boundary integral equation, while the second term is the normalized error with respect to the interior equation over a closed interior surface. In order to limit the extra computation time due to the presence of the constraint, the interior surface has been chosen as small as possible, but such

98 CONCLUSIONS

that the field variation over this surface remains visible in computational sense. Therefore, we have chosen the interior surface to enclose a sphere with a diameter of at least half a wavelength. Then, for realistic objects the extra computation time is less than 3%. Numerical examples have shown that the proposed computational method produces stable results even for frequencies corresponding to the interior resonances of the scatterer. We also observed that the location of the interior surface is not important as long as the interior surface is not too close to the boundary surface of the object. Very close to the boundary, numerical problems may occur due to the singular point of the Green function. Furthermore, we have observed that the constrained conjugate gradient scheme converges to a minimum that is representative for the discretization error made in the boundary integral equation. Improving the discretization leads to a lower minimum. With this feature we have arrived at a quantitative criterion for the global error made in the discretization.

In addition, we have developed a calibration scheme in order to be able to compare the numerically computed results with the measured results. Since we model the antenna as an electric dipole source, we determined the effective dipole moment. First we calibrated the modeled field from this dipole source; in fact we determined the actual magnitude of the dipole antenna by means of determining a multiplicative constant between the measured signal and simulated field responces. Next, after presenting the measured and calibrated computed results, we observed a phase shift between the two results. This may be due to the actual positioning of the scatterer, where a small location error is made. Hence we further developed a calibration procedure to find an improved estimate for the location of the origin of the dipole antenna.

We performed a limited number of measurements in an anechoic chamber by moving the dipole antenna to various perfectly conducting objects (targets) in order to compare the measured field responses with simulated results. Since the speed of movement is much smaller than the wave speed in vacuum we considered it as a monostatic scattering problem. This means that for each location of the transmitter/receiver antenna the scattering problem has been handled as a stationary one. The experiments have shown that the method we have developed is successful. In our simulations, we have first computed the surface field with the constrained conjugate gradient method. We stopped the iteration once an error tolerance had been reached. Since we computed the scattered fields at certain discrete points along the mea-

CONCLUSIONS 99

surement range we determined a factor which is roughly proportional to the field change along the movement. We used this factor to improve the initial estimate when we change the antenna position. This leads to a substantial decrease in simulation time. After computation of the surface field we compute the scattered field. We also compared the measured results with simulated results when we take the physical-optics approximation for the surface field. We note that a further reduction in simulation time may be obtained, when we use the extrapolation technique suggested by Tijhuis et al. [30].

After the comparisons of the measured results and the simulated results for some simple canonical objects (sphere, cylinder and plate), we also made some numerical simulations using both the physical-optics approximation and the constrained conjugate gradient method for a capped box, in order to study the accuracy of the physical-optics approximation for a more complicated scatterer. We compared the results for three different orientations of the capped box. In the first orientation, when the antenna moves to the top-cone, the results were the worst. In the second orientation, when the antenna moves to the side-cone, the results were slightly better, because the side-cone is less sharp than the top-cone. Furthermore, we note that the characteristic dimensions are less or equal to a wavelength, so it is not expected that the physical-optics approximation will yield acceptable results. In the third orientation, when the antenna moves to the flat side of the capped box, the results become better. From these facts we conclude that the physical-optics approximation cannot be used for complicated (non-flat) scatterers.

The knowledge about the scattering properties of targets is not only useful for the evaluation of the performance of proximity fuzes, but it can also be used to design proximity fuzes that recognize their target and the geometry of interception. This would lead to an optimization of the burst point, and an increase the effectivity of the fuze.

Future Research

We further remark that, for simplicity reasons, the computational research in this thesis is restricted to the solution of the magnetic-field integral equation over the boundary of the scattering object. The disadvantage is that this equation can only handle closed surfaces with a non-zero volume. For open surfaces (e.g. an infinitely thin plate), one has to use the

100 CONCLUSIONS

electric field integral equation over the boundary, which is a singular first kind equation. For open surfaces this integral has always a unique solution, because there is no interior domain to contain resonant fields. However, the electric-field equation can handle also combinations of open and closed surfaces, as it occurs in the case where the target has the form of a closed object of non-zero volume with some very thin wings. Then, non-uniqueness is again a problem and it is suggested to supplement the electric-field integral equation over the boundary with either the electric-field equation or the magnetic-field equation over a small interior surface. In view of its simplicity we prefer the latter one.

In addition, more research is needed when the scattering object (target) is not electrically perfectly conducting. Actually, the nowadays targets such as missiles, consist of a combination of conducting and non-conducting materials. In that case the boundary integral equations will not be valid and the domain integral equations have to be introduced [32].

Appendix

A. Discretization of the geometry

In our analysis of Chapter 4, we need an expression for a linear interpolation function on a triangle S_n . We therefore define the vectors \mathbf{L}_i that are oriented along the outward normal to the respective edges in the plane of S_n , each of them having a magnitude that equals the length of the relevant edge (see Fig. A.1). We have

$$L_i = a_i \times \nu \,, \tag{A.1}$$

and

$$\sum_{i=1}^{3} \mathbf{L}_i = 0. \tag{A.2}$$

To arrive at a representation to express any quantity in the interior and on the boundary of each planar triangle, we introduce the barycentric coordinates of the position of observation in the triangle. Let $\{\lambda_i; i = 1, 2, 3\}$ denote the barycentric coordinates pertaining to S_n . Then, the position of observation \boldsymbol{x} in the interior and on the boundary of S_n can be specified by

$$\boldsymbol{x} = \sum_{i=1}^{3} \lambda_i \boldsymbol{x_i}, \quad \text{where } 0 \leq \lambda_i \leq 1 \text{ with } \sum_{i=1}^{3} \lambda_i = 1, \text{ for } \boldsymbol{x} \in S_n, \quad (A.3)$$

in which x_i are the position vectors of the respective vertices of S_n . Eq. (A.3) yields the value of x for given values of λ_i . However, we want an expression that yields the values of λ_i for a given value of $x \in S_n$. We can do that by selecting one of the vertices of S_n as the preferred one and eliminating the

102 APPENDIX

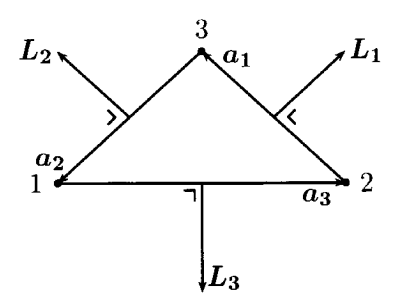


Figure A.1: Perpendicular view on S_n .

barycentric coordinate that has the value one at that vertex. As an example we choose λ_1 as the preferred vertex, and accordingly we eliminate λ_1 with using the relation $\lambda_1 = 1 - \lambda_2 - \lambda_3$. This yields,

$$\boldsymbol{x} - \boldsymbol{x_1} = \sum_{i=2}^{3} \lambda_i \left[\boldsymbol{x_i} - \boldsymbol{x_1} \right]. \tag{A.4}$$

Next, taking the dot product of ν with Eq. (4.3) and using Eq. (4.4), we can easily verify that

$$(\boldsymbol{x_2} - \boldsymbol{x_1}) \cdot \boldsymbol{L_2} = -2A, \tag{A.5}$$

and

$$(\boldsymbol{x_3} - \boldsymbol{x_1}) \cdot \boldsymbol{L_3} = -2A \tag{A.6}$$

Furthermore, applying Eq. (A.5) and Eq. (A.6) to Eq. (A.4) gives

$$(\boldsymbol{x} - \boldsymbol{x_1}) \cdot \boldsymbol{L_2} = -2A\lambda_2, \qquad (A.7)$$

and

$$(\boldsymbol{x} - \boldsymbol{x}_1) \cdot \boldsymbol{L}_3 = -2A\lambda_3. \tag{A.8}$$

where we have used that $(x_3 - x_1) \cdot L_2 = 0$ and $(x_2 - x_1) \cdot L_3 = 0$. Adding Eq. (A.7) with Eq. (A.8) and using the relation $L_1 = -L_2 - L_3$ gives

$$(\boldsymbol{x} - \boldsymbol{x_1}) \cdot \boldsymbol{L_1} = 2A(\lambda_2 + \lambda_3). \tag{A.9}$$

Applying the expressions, that result from Eqs. (A.7)-(A.8) for λ_2 , λ_3 and Eq. (A.9) for $\lambda_2 + \lambda_3$, in Eq. (A.4) yields,

$$\boldsymbol{x} - \boldsymbol{x_1} = \frac{-1}{2A} \sum_{i=1}^{3} \left[(\boldsymbol{x} - \boldsymbol{x_1}) \cdot \boldsymbol{L_i} \right] \boldsymbol{x_i}. \tag{A.10}$$

Results similar to Eq. (A.10) hold when x_1 is replaced by x_2 and x_3 , respectively. Upon adding the relevant results, we end up with the symmetrical expression

$$\boldsymbol{x} - \boldsymbol{b} = \frac{-1}{2A} \sum_{i=1}^{3} \left[(\boldsymbol{x} - \boldsymbol{b}) \cdot \boldsymbol{L}_{i} \right] \boldsymbol{x}_{i}, \qquad (A.11)$$

in which

$$\boldsymbol{b} = \frac{1}{3} \sum_{i=1}^{3} \boldsymbol{x_i} \tag{A.12}$$

is the position vector of the barycenter of S_n . Finally when we compare Eq. (A.11) with Eq. (A.3) we conclude that

$$\lambda_i = \frac{1}{3} - \frac{(\mathbf{x} - \mathbf{b}) \cdot \mathbf{L_i}}{2A}. \tag{A.13}$$

Eq. (A.13) gives the desired representation to express any quantity in the interior and on the boundary of each planar triangle S_n . That is why, we will use Eq. (A.13) as a linear interpolation function in the subsequent analysis. Regarding this aspect we shall write a more general form linear interpolation function $\Phi_{n,i}(x)$ instead of λ_i , i.e., Eq. (A.13) is rewritten as

$$\Phi_{n,i}(\boldsymbol{x}) = \frac{1}{3} - \frac{(\boldsymbol{x} - \boldsymbol{b_n}) \cdot \boldsymbol{L_{n,i}}}{2A_n}, \qquad (A.14)$$

in which b_n is the position vector of the barycenter of S_n and, $L_{n,i}$ are the vectors normal to the respective edges in the plane of S_n , and A_n is the scalar area of S_n . We can express now local expansion of any vectorial function A(x) as

$$F(x) = \sum_{i=1}^{3} F(x_i) \Phi_i(x). \qquad (A.15)$$

With the aid of Eq. (A.12) and Eqs. (4.2)-(A.1) we can easily show that Eq. (A.14) has the property

$$\Phi_{n,i}(\boldsymbol{x}_j) = \delta_{i,j} \,. \tag{A.16}$$

For our computations we use the software package Rhinoceros [31] to generate a discretization mesh of the surface of the object under consideration. Subsequently, the output is used to generate a data set containing the 104 APPENDIX

data of each triangle, such as the vertices, the vectorial edges, the normal vectors to the surface and to the edges.

B. Weak form of Green's function

In the discretized kernel of the magnetic field integral equation we have to compute the gradient of the Green function, viz.,

$$\nabla_p G(\boldsymbol{x} - \boldsymbol{x}_p) = -[\mathrm{i}k_0|\boldsymbol{x} - \boldsymbol{x}_p| - 1] \exp(\mathrm{i}k_0|\boldsymbol{x} - \boldsymbol{x}_p|) \frac{\boldsymbol{x} - \boldsymbol{x}_p}{4\pi|\boldsymbol{x} - \boldsymbol{x}_p|^3}.$$
 (B.1)

In view of the continuity of the kernel, it is allowed to replace the kernel in a discretized configuration by its spherical mean. The radius of the spherical domain is taken equal to the average discretization size Δ of the object under consideration. But we restrict the spherical mean over the singular part only. To this end we write the singular factor at the right-hand side of Eq. (B.1) as

$$\frac{\boldsymbol{x} - \boldsymbol{x}_p}{4\pi |\boldsymbol{x} - \boldsymbol{x}_p|^3} = \nabla_p \left(\frac{1}{4\pi |\boldsymbol{x} - \boldsymbol{x}_p|} \right). \tag{B.2}$$

Subsequently we define our mean of $\nabla_p G$ over a spherical domain D_{Δ} with radius Δ as

$$\nabla_{p} \mathcal{G}(\boldsymbol{x} - \boldsymbol{x}_{p}) = -[\mathrm{i}k_{0}|\boldsymbol{x} - \boldsymbol{x}_{p}| - 1] \exp(\mathrm{i}k_{0}|\boldsymbol{x} - \boldsymbol{x}_{p}|) \nabla_{p} g(\boldsymbol{x} - \boldsymbol{x}_{p}), \quad (B.3)$$

where

$$g(\boldsymbol{x} - \boldsymbol{x}_p) = \frac{3}{4\pi\Delta^3} \int_{\boldsymbol{x}' \in D_{\Delta}} \frac{1}{4\pi |\boldsymbol{x}' + \boldsymbol{x} - \boldsymbol{x}_p|} dV.$$
 (B.4)

The simplest way to evaluate this integral is to introduce spherical coordinates in the x'-space with center at x'=0 and the direction $x-x_p$ as polar axis. Let r=|x'| and θ the polar angle between x' and $x-x_p$, then the range of integration is $0 \le r \le \Delta$, $0 \le \theta \le \pi$, $0 \le \phi < 2\pi$, where ϕ is the azimuth angle in the plane perpendicular to $x-x_p$. Let further $R=|x-x_p|$. Then in the integral we have

$$|\mathbf{x}'+\mathbf{x}-\mathbf{x}_p| = \left[r^2 + R^2 + 2rR\cos(\theta)\right]^{\frac{1}{2}},$$
 (B.5)

and $dV = r^2 \sin(\theta) dr d\theta d\phi$. In the resulting integral we first carry out the integration with respect to ϕ . Since the integrand is independent of ϕ , this merely amounts to a multiplication by a function of 2π . Next we carry out the integration with respect to θ , which is elementary. After this we have

$$\int_{\mathbf{x}' \in D_{\Delta}} \frac{1}{4\pi |\mathbf{x}' + \mathbf{x} - \mathbf{x}_p|} dV = \frac{1}{2R} \int_0^{\Delta} [(R+r) - |R-r|] r dr.$$
 (B.6)

Integration with respect to r is straightforward and yields

$$\int_{\boldsymbol{x}' \in D_{\Delta}} \frac{1}{4\pi |\boldsymbol{x}' + \boldsymbol{x} - \boldsymbol{x}_p|} dV = \begin{cases} \frac{1}{2} \Delta^2 - \frac{1}{6} |\boldsymbol{x} - \boldsymbol{x}_p|^2, & \text{when } 0 \le |\boldsymbol{x} - \boldsymbol{x}_p| < \Delta, \\ \\ \frac{\Delta^3}{3|\boldsymbol{x} - \boldsymbol{x}_p|}, & \text{when } \Delta \le |\boldsymbol{x} - \boldsymbol{x}_p| < \infty. \end{cases}$$

Hence, the spherical mean of the inverse distance as defined in Eq. (B.4) is given by

$$g(\boldsymbol{x}-\boldsymbol{x}_p) = \begin{cases} \frac{3}{4\pi\Delta^3} \left(\frac{1}{2}\Delta^2 - \frac{1}{6}|\boldsymbol{x}-\boldsymbol{x}_p|^2\right), & \text{when } 0 \leq |\boldsymbol{x}-\boldsymbol{x}_p| < \Delta, \\ \\ \frac{1}{4\pi|\boldsymbol{x}-\boldsymbol{x}_p|}, & \text{when } \Delta \leq |\boldsymbol{x}-\boldsymbol{x}_p| < \infty. \end{cases}$$
(B.8)

The gradient of this function is obtained as

$$\nabla_{p}g(\boldsymbol{x}-\boldsymbol{x}_{p}) = \begin{cases} \frac{\boldsymbol{x}-\boldsymbol{x}_{p}}{4\pi\Delta^{3}}, & \text{when } 0 \leq |\boldsymbol{x}-\boldsymbol{x}_{p}| < \Delta, \\ \frac{\boldsymbol{x}-\boldsymbol{x}_{p}}{4\pi|\boldsymbol{x}-\boldsymbol{x}_{p}|^{3}}, & \text{when } \Delta \leq |\boldsymbol{x}-\boldsymbol{x}_{p}| < \infty. \end{cases}$$
(B.9)

With this result, substituted into Eq. (B.3) we arrive at our desired expression for the weak form of $\nabla_{p}\mathcal{G}$, i.e.,

$$\nabla_{p}G(x - x_{p}) = -(x - x_{p})\partial G(|x - x_{p}|)$$
(B.10)

with

$$\partial G(R) = \begin{cases} (\mathrm{i}k_0 R - 1) \frac{\exp(\mathrm{i}k_0 R)}{4\pi\Delta^3}, & \text{when } 0 \le R < \Delta, \\ (\mathrm{i}k_0 R - 1) \frac{\exp(\mathrm{i}k_0 R)}{4\pi R^3}, & \text{when } \Delta \le R. \end{cases}$$
(B.11)

106 APPENDIX

These expressions are used in Chapter 4 in the discretization of the magnetic field equation. Note that the expression for $R \geq \Delta$ is exactly equal to the strong form as given in Eq. (B.1).

Bibliography

- [1] M.H. Vogel, Electromagnetic Scattering by a Moving Object, Ph.D. Thesis, Delft, 1991.
- [2] A.T. de Hoop, *Handbook of Radiation and Scattering of Waves*, Academic Press, Delft, 1995.
- [3] A.J. Poggio and E.K. Miller, Integral Equations for three dimensional scattering problems, in *Computer Techniques for Electromagnetics*, R. Mittra, Ed., Pergamon Press, New York, pp. 159-264, 1973.
- [4] N. Morita, N. Kumaga and J.R. Mautz, Integral Equation Methods for Electromagnetics, Artech House, Boston, 1990.
- [5] D. Colton and R. Kress, Integral Equations Methods in Scattering Theory, John Wiley & Sons, New York, 1983.
- [6] K.J. Langenberg, A thorough look at the non-uniqueness of the electromagnetic scattering integral equation solutions as compared to the scalar acoustic ones, *Radio Science*, to be published, 2002.
- [7] K.K. Mei and J.G. van Bladel, Scattering by perfectly-conducting rectangular cylinders, *IEEE Trans. Antennas Propagat.*, AP-11, pp. 185-192, 1963.
- [8] M. Hestenes and E. Steifel, Method of conjugate gradients for solving linear systems, J. Res. Nat. Bur. Stand., 49, pp. 409-436, 1952.
- [9] T.K. Sarkar (Ed.), Application of Conjugate Gradient Method to Electromagnetics and Signal Analysis, PIER 5, Elsevier, Amsterdam, 1991.

108 BIBLIOGRAPHY

[10] K.M. Mitzner, Numerical solution of the exterior scattering problem and eigenfrequencies of the interior problem, *Digest 1968 URSI Radio Science Meeting*, Boston, MA, p. 75, 1968.

- [11] J.R. Mautz and R.F. Harrington, H-field, E-field and combined-field solutions for conducting bodies of revolution, A.E.Ü., 32, pp. 157-163, 1978.
- [12] A.F. Peterson, The interior resonance problem associated with surface integral equations of electromagnetics: Numerical consequences and a survey of remedies, *Electromagn.*, **10**, pp. 293-312, 1990.
- [13] A.D. Yaghjian, Augmented electric- and magnetic-field integral equations, *Radio Sci.*, **16**, pp. 987-1001, 1981.
- [14] R.E. Kleinman and P.M. van den Berg, A modified gradient method for two-dimensional problems in tomography, J. Comput. appl. math, 42, pp. 17-35, 1992.
- [15] S. Markarov and R. Vedantham, Performance of GMRES iterative solution for the magnetic field integral equation, *Radio Sci.*, to be published.
- [16] M.B. Woodworth and A.D. Yaghjian, Derivation, application and CG solution of dual-surface integral equation equations for threedimensional, multi-wavelength perfect conductors, in Application of Conjugate Gradient Method to Electromagnetics and Signal Analysis, T.K. Sarkar, Ed., PIER 5, Elsevier, Amsterdam, pp. 103-129. 1991.
- [17] M.B. Woodworth and A.D. Yaghjian, Multiwavelength three-dimensional scattering with dual-surface integral equations, J. Opt. Soc. Am. A, 11, pp. 1399-1413, 1994.
- [18] G.W. Oseen, Über die Wechselwirkung zwischen zwei elektrischen Dipolen und über die Drehung der Polarisationsebene in Kristallen und Flüssigkeiten, Annalen der Physik, 48, pp. 1-56, 1915.
- [19] H.A. Schenck, Improved integral formulation for acoustic radiation problems, J. Acoust. Soc. Am., 44, pp. 41-58, 1967.
- [20] R. Mittra and C.A. Klein, Stability and convergence of moment method solutions, in *Numerical and Asymptotic Techniques in Electromagnetics*, R. Mittra, Ed., Springer-Verlag, New York, pp. 129-163, 1975.

BIBLIOGRAPHY 109

[21] P.C. Waterman, Numerical solution of electromagnetic scattering problems, in *Computer Techniques for Electromagnetics*, R. Mittra, Ed., pp. 97-157, 1973.

- [22] P.M. van den Berg, Iterative computational techniques in sacttering based upon the integrated square error criterion, *IEEE Trans. Antennas Propagat.*, AP-32, pp. 1063-1071, 1984.
- [23] P.W. Barber and S.C. Hill, Light Scattering by Particles: Computational methods, World Scientific, Singapore, 1990.
- [24] P.M. van den Berg, Iterative schemes based on minimization of a uniform error criterion, in *Application of Conjugate Gradient Method to Electromagnetics and Signal Analysis*, T.K. Sarkar, Ed., PIER 5, Elsevier, Amsterdam, pp. 27-65. 1991.
- [25] G.L. Naber, Topological methods in Euclidean spaces, Cambridge University Press, Cambridge, 1980.
- [26] A.P.M. Zwamborn and P.M. van den Berg, A Weak Form of the Conjugate Gradient FFT Method for Plate Problems, *IEEE Trans. Antennas Propagat.*, **39**, pp. 224-228, 1991.
- [27] R.F. Bloemenkamp, A. Abubakar and P.M. van den Berg, Inversion of experimental multi-frequency data using the contrast source inversion method, *Inverse Problems*, 17, pp. 1611-1622, 2001.
- [28] P.M. van den Berg and R.E. Kleinman, Iterative schemes based on minimization of a uniform error criterion, in Application of Conjugate Gradient Method to Electromagnetics and Signal Analysis, T.K. Sarkar, Ed., PIER 5, Elsevier, Amsterdam, pp. 67-102. 1991.
- [29] R.E. Kleinman and P.M. van den Berg, Iterative methods for radiowave problems, in *Review of Radio Science 1990-1992*, W.R. Stone, Ed., Oxford University Press, 1993.
- [30] A.G. Tijhuis, M.C. van Beurden and A.P.M. Zwamborn, Using Extrapolation in the Iterative Solution of Scattering Problems with a Varying Parameter, *Proc. Int. Conf. on Electromagnetics in Advanced Applications*, 10-14 September 2001, Politecnico di Torino, Torino, Italy, pp. 845-848, 2001

110 BIBLIOGRAPHY

[31] Rhinoceros, NURBS modeling for Windows, Version 1.0, User's Guide, Robert McNeel & Associates, U.S.A., 1993.

[32] A. Abubakar, Three-Dimensional Nonlinear Inversion of Electrical Conductivity, Ph.D. Thesis, Delft, 2000.

Samenvatting

Modellering van elektromagnetische wisselwerking van nabijheidsbuizen voor naderende doelen

door Erdal Korkmaz

Kennis over de verstrooiingseigenschappen van een voorwerp is waardevol bij het modelleren van nabijheidsbuizen. Deze buizen worden gebruikt voor de verdediging tegen luchtaanvallen van een vijandelijke vliegtuig of raket. De nabijheidsbuizen worden naar het doel geleid en op het juiste moment worden explosieven gebruikt om het doel uit te schakelen. Meer kennis over de verstrooiing van een elektromagnetische golf door een voorwerp kan gebruikt worden voor het beter onderkennen van de geometrie van het doel en het punt van interceptie. Dit kan leiden tot een verdere optimalisatie van het tijdstip van explosie, en dientengevolge tot een hogere effectiviteit van de verdediging.

In dit proefschrift wordt een efficiënte methode ontwikkeld om elektromagnetische verstrooiing aan perfect-geleidende voorwerpen numeriek te berekenen. In het bijzonder worden integraalrepresentaties voor de verstrooide elektromagnetische veldgrootheden afgeleid. In deze representaties is de tangentiële component van de magnetische veldvector op de rand van

112 SAMENVATTING

het voorwerp de enige onbekende grootheid. Voor deze onbekende veldgrootheid worden twee soorten integraalvergelijkingen over de rand van het voorwerp afgeleid, één van het elektrische type en één van het magnetische type. Voor bepaalde frequenties van het invallend veld leveren deze integraalvergelijkingen geen eenduidige oplossing. Wij eisen daarom ook de consistentie van de integraalrepresentaties in het binnengebied van het verstrooiende voorwerp. Om de rekenkundige complexiteit zo veel mogelijk te beperken, zijn, voor het oplossen van de onbekende veldgrootheid op de rand van het voorwerp, de integraalvergelijkingen van het magnetische type gekozen. De in dit proefschrift ontwikkelde numerieke rekenmethoden zijn ook met metingen geverifiëerd.

Voor het oplossen van de integraalvergelijkingen over de rand van het voorwerp is de geconjugeerde gradiëntenmethode als een iteratieve oplosser gebruikt. Voor bepaalde frequenties hebben wij inderdaad waargenomen dat de oplossing van onze integraalvergelijking niet eenduidig is. Dit heeft te maken met mathematisch gecreëerde interne resonanties. Om de nieteenduidigheid te herstellen, hebben wij de integraalrepresentaties over een gesloten oppervlak in het binnengebied van het voorwerp als een noodzakelijke eis opgelegd. Dat wil zeggen, het probleem wordt gesteld als een optimalisatie-probleem, waarbij een foutennorm van twee termen wordt geformuleeerd. De eerste term is de genormaliseerde foutennorm ten aanzien van de integraalvergelijking over de rand van het voorwerp, terwijl de tweede term de genormaliseerde foutennorm is ten aanzien van de integraalrepresentatie over een gesloten oppervlak in het inwendige van het voorwerp. De totale foutennorm wordt met de geconjugeerde gradiëntenmethode geminimaliseerd. Om de extra rekentijd te beperken, is het interne oppervlak zo klein mogelijk gekozen, maar dusdanig dat veldvariaties over het interne oppervlak rekenkundige betekenis blijven houden. Derhalve kiezen wij een zodanig oppervlak, dat het omsloten wordt door een bol met een diameter van tenminste een halve golflengte. Voor realistische voorwerpen is de extra rekentijd te verwaarlozen. Numerieke experimenten hebben aangetoond dat de voorgestelde rekenmethode betrouwbare resultaten geeft en het probleem van de interne resonanties vermijdt. Verder hebben wij ook geconstateerd dat de positie van het interne oppervlak niet belangrijk is, zo lang dit interne oppervlak niet te dicht bij de rand van het voorwerp wordt gekozen. Dicht bij de rand voor het voorwerp ontstaan numerieke problemen door aanwezigheid van het singuliere punt van de Greense functie. Van groter belang is de constatering dat de nieuwe geconjugeerde gradiëntenmethode

SAMENVATTING 113

convergeert naar een minimum, dat representatief is voor de fout, gemaakt in de discretizatie van de integraalvergelijking over de rand van het voorwerp. Een verbetering in de discretisatie levert een lager minimum van de foutennorm. Dit betekent dat wij een kwantitatief foutencriterium hebben voor de gemaakte discretisatie-fouten.

Om de numeriek berekende resultaten met gemeten resultaten te kunnen vergelijken hebben wij een calibratie-schema ontwikkeld. Omdat wij veronderstellen dat de antenne gemodeleerd kan worden door een elektrische dipool, moet de effectieve plaats en het effectieve moment van de dipool bepaald worden. Daartoe wordt als verstrooiiend voorwerp een zeer grote plaat genomen, zodat het gereflecteerde veld eenvoudig bepaald kan worden, namelijk met het spiegelingsprincipe. Eerst wordt het effectieve moment van de dipool bepaald door middel van het berekenen van de globale factor tussen de gemeten velden en de berekende velden, waarna de berekende velden met deze factor gecalibreerd worden. Vervolgens wordt de effectieve plaats van de dipool bepaald door binnen een interval van een golflengte, de faseverschillen tussen de gemeten en gecalibreerde computer-resultaten te minimalizeren.

Na een verdere vergelijking van de gemeten resultaten met de gecalibreerde computer-resultaten voor een bepaald type voorwerp, hebben wij weer faseverschillen geconstateerd tussen de twee resultaten. Dit is te wijten aan onzekerheden tijdens het handmatig positioneren van het verstrooiende object. Om die reden wordt de tweede calibratie-procedure herhaald om de oorspronkelijke effectieve locatie van de dipool ten opzichte van het verstrooiende object te berekenen.

Vervolgens hebben wij metingen verricht door het laten naderen van de dipool-antenne naar verschillende goed-geleidende voorwerpen. Omdat de snelheid van de beweging veel kleiner is dan de lichtsnelheid, hebben wij het als monostatische verstrooiing beschouwd. Dat wil zeggen, voor elke locatie van de dipool-antenne, wordt het verstrooiingsprobleem als een stationair probleem beschouwd. In de simulaties worden de verstrooide velden op bepaalde discrete punten berekend langs de meettraject. In het eerste punt wordt de velden berekend met een nauwkeurigheid, die bepaald wordt door een van te voren gestelde fouttolerantie. Daarna hebben wij een constante bepaald, die ongeveer evenredig is met de veldveranderingen langs het meettraject. Deze constante wordt gebruikt om de beginschatting van het onbekende veld in de geconjugeerde gradiëntenmethode te verbeteren, zodra

114 SAMENVATTING

de antennepositie veranderd is. Dat heeft de computertijd fors verlaagd. De experimenten laten zien dat de ontwikkelde rekenmethode succesvol is. Wij hebben ook de resultaten, verkregen met de zogenaamde fysisch-optische benadering, vergeleken met metingen. Hieruit kan geconcludeerd worden dat de fysisch-optische benadering geen betrouwbare resultaten geeft voor gecompliceerde (geen vlakke) voorwerpen.

Tenslotte wordt opgemerkt, dat de ontwikkelde rekenmethode in dit proefschrift beperkt is tot de oplossing van integraalvergelijking van het magnetische type. Alleen die voorwerpen kunnen worden gebruikt, waarvan de rand een gesloten oppervlak vormt en een inwendige gebied omsluit met een volume ongelijk aan nul. Voor open oppervlakken, zoals oneindig dunne platen, dient de integraalvergelijking van het elektrische type gebruikt te worden.

About the author

Erdal Korkmaz was born in Göle, Turkey, on February 10, 1973. From 1984 to 1990 he studied at the Public High School in Göle, Turkey. In December 1990 he moved to The Netherlands. From 1991 to 1992 he started his university study with an admittance course at the Delft University of Technology. From 1992 to 1997 he studied at the Faculty of Electrical Engineering of the Delft University of Technology. His masters thesis was about Low-Stress PECVD a-SiC Thin Films for IC-Compatible Microstructures and carried out at the Laboratory of Electronic Components, Technology and Materials. His masters thesis was published as an international paper and presented at an international conference. In March 1998 he started with his Ph.D. thesis at the Laboratory of Electromagnetic Research, Delft, under supervision of Prof.dr.ir. P.M. van den Berg. He developed during a period of four year an efficient computational method to calculate the electromagnetic scattering for perfectly conducting objects. The thesis project was financed by TNO Physics and Electronics Laboratory in The Hague, The Netherlands. His research resulted in an international paper and a presentation at an international conference.

Currently, he works as a postdoctoral researcher at the Laboratory of Telecommunication Technology and Electromagnetics of the Eindhoven University of Technology. The research is about the modeling of electromagnetic waves in periodic structures financed by ESTEC, Noordwijk, The Netherlands.

